23-3-71

AN OPTICAL STUDY
OF
ATMOSPHERIC AEROSOLS

by

D. J. Gambling, M.Sc.

A Thesis
presented for the degree of
DOCTOR OF PHILOSOPHY
at the
UNIVERSITY OF ADELAIDE
(Physics Department)

August 1970

FRONTISPIECE. The author (right) and colleague, K. Bartusek, with the mobile instrumentation van housing the laser radar.

CONTENTS

SUMMARY

In recent years aerosols have become of increasing importance in several fields of meteorology. However, our knowledge of the properties and distribution of aerosols above the first few kilometres of the atmosphere has been limited by difficulties experienced using present techniques.

This thesis describes an investigation of aerosols in the atmosphere, by means of their light scattering properties, using a ruby laser radar. Since its advent in 1960, the laser beam has proved to be the most satisfactory of existing remote optical probes. The laser radar described here is capable of measuring atmospheric scattering from nearly ground level to altitudes of 60 km.

Interpretation of existing laser radar measurements using a single wavelength and scattering angle does, however, depend on a priori knowledge of certain aerosol properties. This shortcoming of the present laser radar technique, and other theoretical aspects of light scattering by aerosols, are discussed in some detail. Recent measurements of stratospheric aerosol number densities using balloon-borne optical counters indicate that the stratospheric aerosol is predominantly volatile and hence remains undetected by collection experiments. As little is known of the size distribution of volatile stratospheric aerosols, a theoretical investigation is made of their optical scattering characteristics. Aided by the results of the theoretical analysis, present optical measurements are examined in order to deduce aerosol size distributions compatible with the observations.

Results of laser radar measurements of stratospheric aerosols conducted in South Australia are presented. The vertical profiles are broadly in agreement with observations reported by other workers in the northern hemisphere. An annual variation apparent in the laser radar observations is remarkably similar to that of ozone in the stratosphere, and the importance of large scale transport mechanisms in the stratosphere is discussed.

Results of tropospheric aerosol measurements are presented, showing vertical profiles typical of the coastal regions. The relation between temperature inversions, humidity and aerosol layers observed in the troposphere is investigated.

The reliability of the twilight scattering experiment used by several workers to study stratospheric aerosols is discussed, and a comparison is made of the results of twilight and laser radar experiments conducted at the same time and locality. A theoretical model of the twilight phenomenon based on primary scattering is developed, and calculations are performed to deduce the relative effects of the various aerosol layers in the troposphere and stratosphere on the twilight profile.

PREFACE

To the best of the author's knowledge, this thesis contains no material previously published or written by another person, except where due reference is made in the text. It contains no material which has been submitted or accepted for the award of any other degree or diploma in any University.

(D. J. Gambling)

University of Adelaide
14/8/70

ACKNOWLEDGEMENTS

The work described in this thesis was undertaken in the Physics Department of the University of Adelaide under the supervision of Dr. W. G. Elford. The author is grateful to Dr. Elford for his advice and guidance during the course of the work.

The author is indebted to his colleague, Mr. K. Bartusek, who was responsible for the initial design and construction of the laser radar, and who assisted with the final installation and operation of the equipment. Thanks are also due to Mr. L. Thomas, who constructed much of the electronic and ancillary equipment, and who assisted in the operation of the laser radar. Mr. M. Manuel was responsible for most of the mechanical construction.

Acknowledgement is due to the Director of the Mawson Institute for Antarctic Research, Dr. Jacka, who made available the Mt. Torrens field station during the early stages of the observations. The author is grateful to the Weapons Research Establishment for the loan of the instrumentation van, and in particular, to Mr. B. Rofe, who made the arrangements.

The author is indebted to the Director of the Commonwealth Bureau of Meteorology for providing the meteorological data used in the analysis. The author is particularly grateful for the assistance of Mr. V. Deering of the Meteorological Office at Adelaide Airport, and to Mr. L. Mitchell of the Regional Office.

Thanks are due to Dr. B. Pittock and Dr. B. Hicks of the Division of Meteorological Physics, C.S.I.R.O., and to Dr. E. K. Bigg of the Division of Radiophysics, C.S.I.R.O., who made their records available.

Finance for the laser project was provided by the Commonwealth Department of Supply, and the University of Adelaide. The author was a holder of a Post-Graduate Studentship from the Department of Supply.

CHAPTER ONE

A SURVEY OF CURRENT KNOWLEDGE OF AEROSOLS

Aerosols in the troposphere and stratosphere are of importance to various branches of meteorology. The largest particles are responsible for the formation of clouds and fogs, and smaller ones give rise to haze which can, under certain conditions, seriously affect the visibility of distant objects. In recent years volcanic dust has been used as a tracer of transport mechanisms in the lower stratosphere (Dyer and Hicks, 1968) in analogy with the well known tracer studies using ozone. In the last decade man has created a serious problem in the form of air pollution in the large cities and industrial centres, and in some regions, aerosol concentrations have reached alarming proportions. In addition to the obvious health hazards, it is conceivable that abnormal concentrations of aerosols could significantly affect the large scale weather pattern by means of a change in transfer processes of radiation in the atmosphere. Aerosols in the stratosphere and mesosphere are also believed to play a very important part in the heat budget (Kellog, 1968).

Under conditions of cloudless skies, the effects of aerosols in the troposphere are commonly manifested in the whiteness of the horizon sky, particularly in the direction of the sun, and in the solar aureole, a diffuse circle of white light surrounding the sun. Layers of aerosols are frequently observed from aircraft, particularly when the sun is low in the sky. Many splendid optical phenomena in the atmosphere can be observed as a result of abnormal aerosol characteristics. Under exceptional circumstances such as the periods following the famous eruption of Krakatoa in 1883, and the extensive forest fires in the Canadian province of Alberta in 1950, the sun appeared blue or green (Minnaert, 1959, 1968). In both cases large amounts of aerosols were injected into the atmosphere.

Evidence indicates the existence of aerosols at altitudes above the troposphere. Observations of the "purple light" at twilight led Gruner (1942) to postulate a layer of aerosols near 20 km. This has been substantiated in recent years by measurements of twilight effects (Bigg, 1956; Volz and Goody, 1962; Rozenberg, 1966), particle counting experiments (Junge et al, 1961; Mossop, 1965; Friend, 1966; Rosen, 1964, 1968, 1969(a)), searchlight probing (Elterman, 1966; Rozenberg, 1960; Elterman et al, 1969) and lidar measurements (Fiocco and Grams, 1964; Clemesha et al, 1966; Grams and Fiocco, 1967). The existence of a worldwide aerosol layer in the stratosphere is now well established. Noctilucent clouds provide evidence for the presence of aerosols near 85 km, but are rare and only visible at high latitudes in the summer (Fogle, 1966).

The above considerations indicate the existence of significant concentrations of aerosols in the atmosphere between ground level and the mesosphere. However, our present knowledge of the nature of aerosols, their origin and size distribution is far from complete, and only in recent years have rapid advances been made due to improved experimental techniques.

Measurements of aerosol properties in the lower stratosphere, for example, have yielded conflicting results, and the origin of the stratospheric aerosol layer still remains controversial.

In the following sections, current knowledge of the properties of aerosols and their distribution in the atmosphere will be reviewed. Particular emphasis is made of the characteristics affecting optical scattering by aerosols, and in the final section of this chapter, a brief review is made of methods used to optically probe the upper atmosphere.

1.1 The Size of Aerosols

The size of particles in the atmosphere normally ranges from clusters of molecules to particles of about 20 μ radius. Particles less than 0.1 μ have very short lifetimes because they become attached to the larger aerosols, and only exist in significant concentrations near the source. They include the products of gas reactions, and small ions which are produced in air by ionizing radiation. As these particles are optically insignificant, they will not be considered in the present work. The upper limit of aerosol sizes is determined by sedimentation, and particles larger than about 20 μ radius remain airborne for only a limited time. These particles are also limited to the vicinity of their source, and in a similar manner to the small ions, exist in low concentrations.

Thus the sizes of atmospheric aerosols cover over four orders of magnitude, and as a result of the various techniques that have been evolved to detect them, the size range is normally divided into three principal groups.

(a) Aitken particles have radii less than 0.1 μ, and have been studied extensively since the beginning of the century using Aitken's nuclei counter, which operates on the principle of the Wilson cloud chamber.

(b) Aerosols having radii between 0.1 and 1.0 μ are termed large particles and are responsible for some optical effects such as haze because their sizes are of the order of visible wavelengths.

(c) Giant particles are classed as having radii greater than 1 μ and are of importance in the formation of cloud and rain. Their concentrations relative to the other particles are extremely low.

The large and giant particles can be collected by impactor techniques, and those larger than about 0.5 μ can be investigated with the light microscope. Aerosols having radii between 0.1 and 0.5 μ are difficult to study because they are out of range of the two most efficient methods used to date. Although the resolution of the electron microscope is suitable for the size range .1 - .5 μ, the particles studied by means of this technique tend to be modified by the heating action of the electron beam. In recent years, photometric particle counters have been developed (Zinky, 1962).

1.2 Size Distribution and Concentration

Several methods are needed to investigate the total aerosol size range, and very few measurements of the complete size distribution have been made. As a result of the separate methods of investigation, it was thought until recently that the aerosols existed in discrete groups. It is now known that natural aerosols have an essentially coherent size distribution, which is of importance to the understanding of many properties of atmospheric aerosols (Junge, 1963).

If $N(r)$ is the total number of particles (cm^{-3}) of radius less than r, then the logarithmic incremental size distribution function $n(r)$ is defined as follows:

$$n(r) = dN(r)/d(\log r) \quad cm^{-3} \tag{1.1}$$

The number of particles $\Delta N(r)$ between radii r_1 and r_2 is then

$$\Delta N(r) = n(r) \log (r_2/r_1) \ . \tag{1.2}$$

The discussion of size distributions and concentrations is divided into three categories. As there is a significant difference in the properties of aerosols over land and sea, these types are considered separately. Stratospheric aerosols form the third group as a consequence of their entirely different origin.

1.2.1 Continental Aerosols

Figure 1.1(a) shows complete size distribution curves for continental areas determined by Junge (1963). The size distribution for radii greater than 0.1 μ appears to fit a power law of the form

$$dN(r)/d\,(\log r) = cr^{-\nu} \tag{1.3}$$

where c is a constant and the exponent ν is approximately 3 in the lower continental troposphere. The lower limit of particle

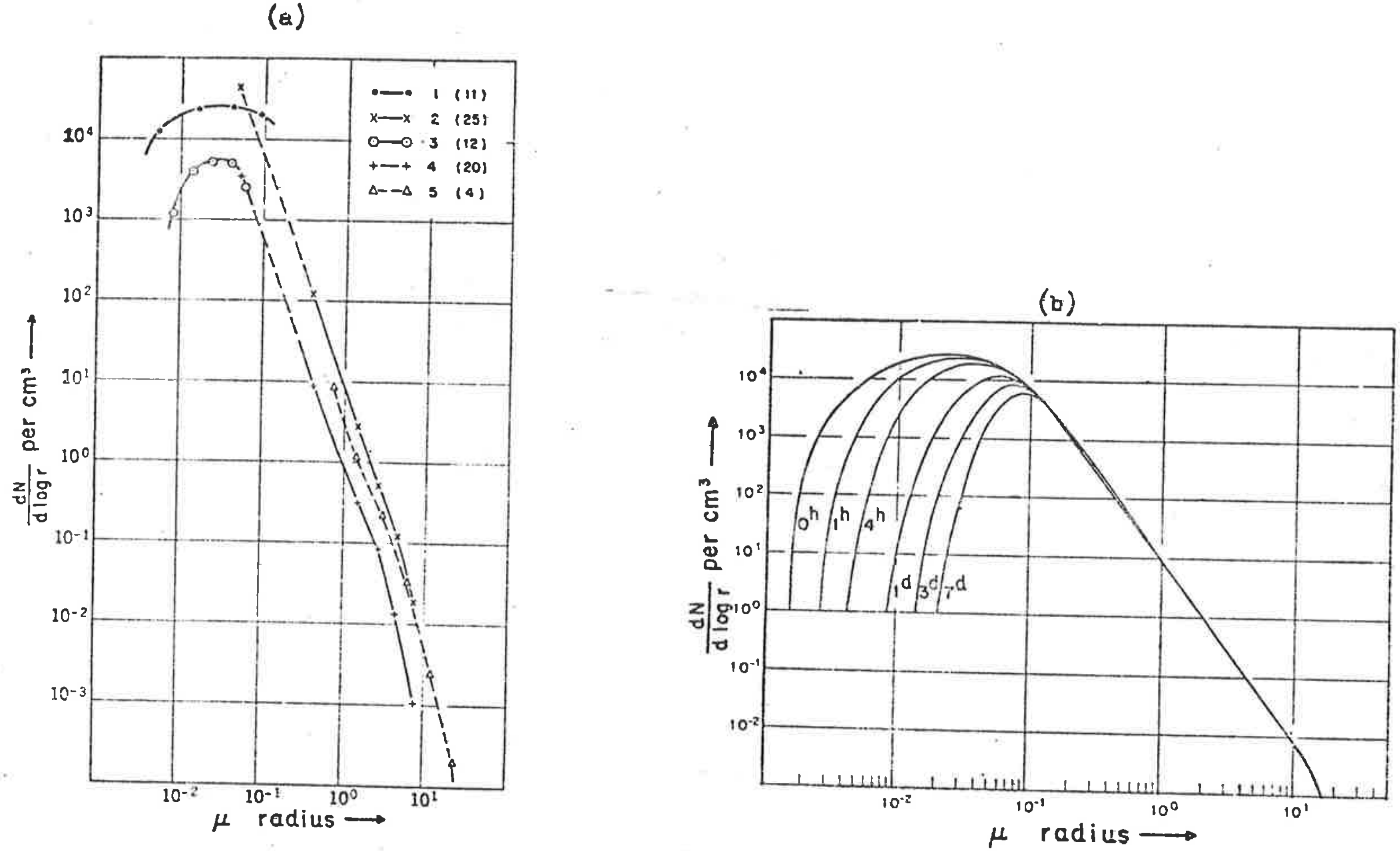

FIGURE 1.1 Size distributions of tropospheric aerosols (after Junge,1963). (a) experimental profiles. (b) calculated changes due to coagulation.

sizes is variable, and the maximum of the distribution lies between 0.01 and 0.1 μ, and is usually about 0.03 μ (Junge, 1963).

Junge (1963) reports that a smooth size distribution curve shown in Figure 1.1(a) represents the end-state of coagulation and sedimentation processes after one or a few days. During this time interval, any discrete spectra in the size distribution curve due to temporary local sources of aerosols would have been smoothed out. Figure 1.1(b) shows how a given size distribution changes with time due to coagulation resulting from Brownian motion (Junge, 1963). The decrease of the Aitken nuclei is rapid compared to the rate of meteorological processes, and results in a displacement of the size distribution maximum towards larger radii. The change in size and concentration of the large particles is negligible because of the small size of the Aitken nuclei.

Junge (1969) has suggested a statistical explanation of the form of the size distribution, based on the fact that the log volume distribution, dV/d(log r), is approximately constant over the large size range. It is possible that equal portions of mass are formed by various sources of aerosols in the different size ranges. The statistical approach is consistent with the concept that the form of a measured size distribution depends on the proximity of the observer to the different sources of aerosols. The presence of a significant source of aerosols in a particular size region would give rise to a peak in the distribution curve. The fine structure in the size distributions observed by Fenn (1964) in the radius region 0.1 - 1.0 μ might be caused by several discrete sources. The measurements of Friedlander and Paceri (1965), Clark and Whitby (1967) and Blifford and Ringer (1969) show significant variability in the shape of the size distribution curve. Independent optical scattering measurements also indicate changes in ν. The experimental evidence suggests that the value of ν for the continental troposphere varies between 2 and 4.

Table 1.1 contains data on Aitken particle concentrations compiled by Landsberg (1938), and shows a wide variation in aerosol concentration over various continental regions. A marked degree of variability in the concentrations observed over a particular area is also evident.

TABLE 1.1

Concentration of Aitken Particles per cm^3 in Different Localities[a]

Locality	Number of:		Average	Average	
	Places	Observat.		Max	Min
City	28	2500	147,000	379,000	49,100
Town	15	4700	34,300	114,000	5900
Country (inland)	25	3500	9500	66,500	1050
Country (sea shore)	21	7700	9500	33,400	1560
Mountain					
500-1000 meters	13	870	6000	36,000	1390
1000-2000 meters	16	1000	2130	9830	450
> 2000 meters	25	190	950	5300	160
Islands	7	480	9200	43,600	460
Ocean	21	600	940	4680	840

a Landsberg (1938)

Rozenberg (1967) has reported that concentrations measured by the impactor technique (e.g. Junge, 1963) do not include the effects of moisture, and are only applicable to the dry base of mineral condensation nuclei. However, tropospheric measurements by Rosen (1964, 1969(b)) and Clark and Whitby (1967) using optical particle counters essentially arrive at the same concentrations and size distribution, indicating a large proportion of solid aerosols in the troposphere. Nevertheless, in the case of large relative humidities, the role of water condensation must significantly alter the form of the size distribution.

A large number of measurements have been made of the variation of aerosol concentration with height in the troposphere. Average profiles of both Aitken and large particles show a rapid and almost exponential decrease in concentration with increasing altitude up to about 5 km, above which the concentration slowly decreases up to the tropopause. There appears to be no difference in the relative tropospheric profiles for Aitken and large particles, indicating that sedimentation is unimportant compared with other effects, which are independent of particle size (Junge, 1963).

Large particle concentrations measured by Rosen (1969(b)) using a balloon-borne photoelectric particle counter indicate a decrease from ground level to the tropopause by nearly 3 orders of magnitude (Figure 1.2). The results show a great deal of fine structure which is well correlated with the relative humidity. Mean

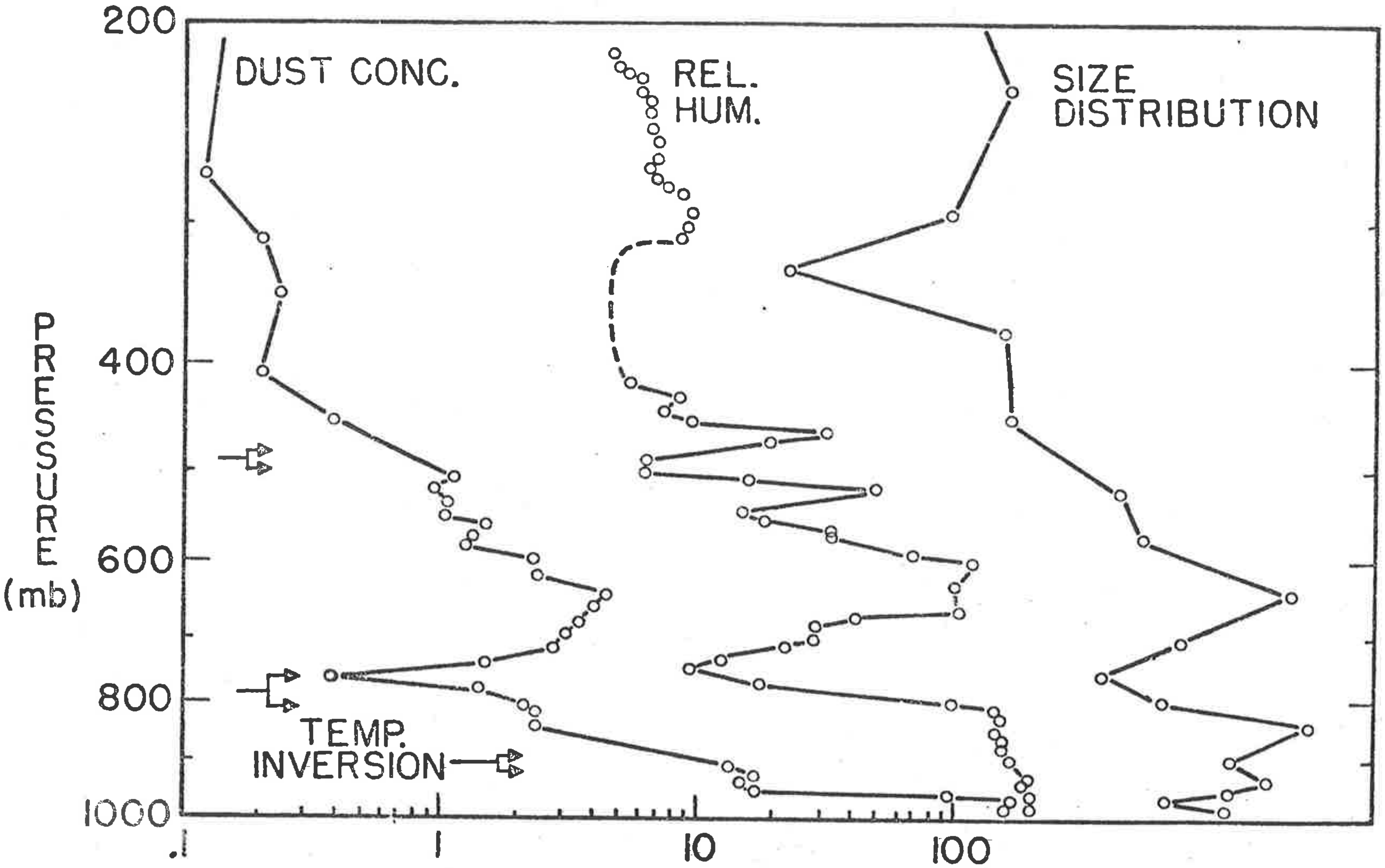

FIGURE 1.2 Vertical profile of large particle concentrations compared with relative humidity and size distribution profiles (after Rosen,1969(b)).

quarterly profiles of large particle concentrations in the troposphere obtained by Blifford and Ringer (1969) using impactors mounted on aircraft are presented in Figure 1.3. It is apparent that the large particle concentration is strongly dependent on the season, with highest concentrations in the summer periods in the layer near the ground. Above 6 km, there is an increase in large particle concentration during winter. The average results of Blifford and Ringer show no general correlation of particle concentration with either temperature or relative humidity curves. The low altitude summer increase in concentration does, however, indicate the importance of convection and vertical mixing processes, which have also been observed by Elterman et al (1969) using optical scattering techniques.

The vertical profile of Aitken nuclei after Junge (1961) is shown in Figure 1.4. The Aitken particle measurements indicate a world-wide background aerosol concentration in the upper troposphere of about 200 - 300 cm^{-3}. The vertical profile suggests that the origin of the Aitken particles is in the first 5 km over the continents.

Few measurements have been made of the variation of size distribution with height. Newkirk and Eddy (1964) measured scattering from the solar aureole by means of a balloon-borne coronograph up to a maximum altitude of 25 km, and deduced the variation of the exponent ν of the Junge power law with height. In the height region 3 - 9 km, the value of ν increased from 2.0 to 2.2 with a tendency to increase still further with altitude. Similar measurements of the solar aureole

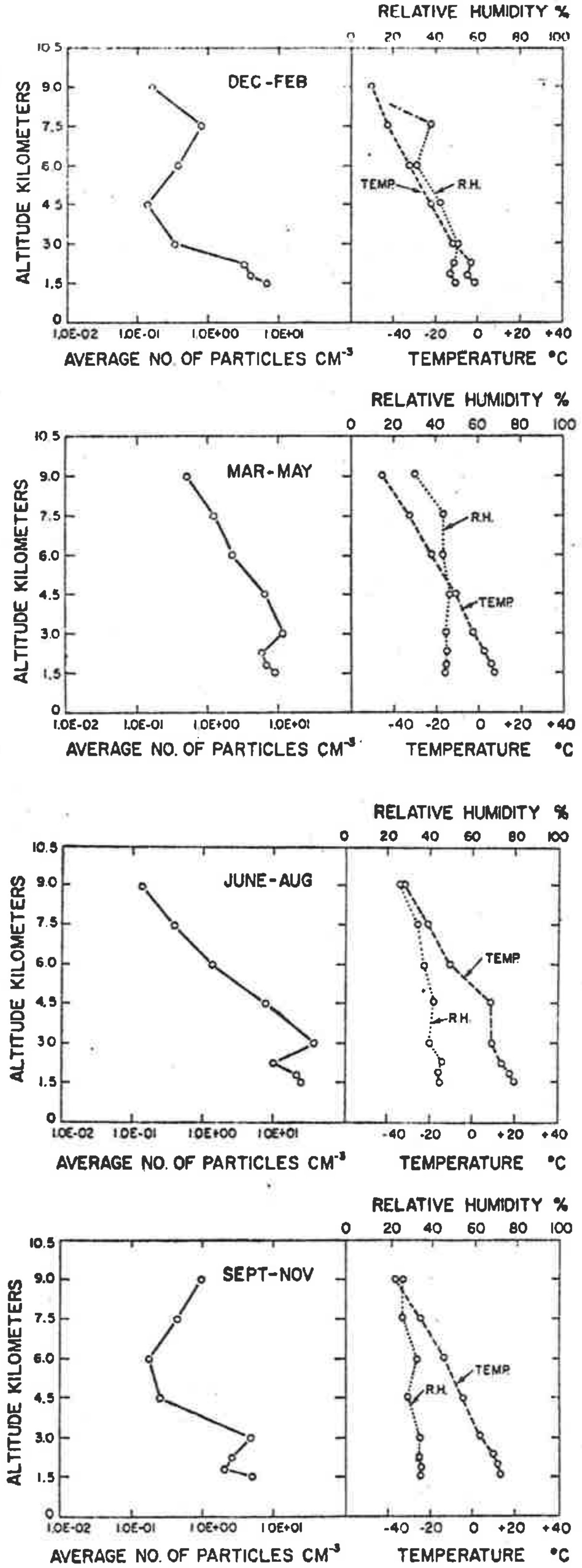

FIGURE 1.3 Average profiles of large particles in the troposphere (after Blifford and Ringer, 1969).

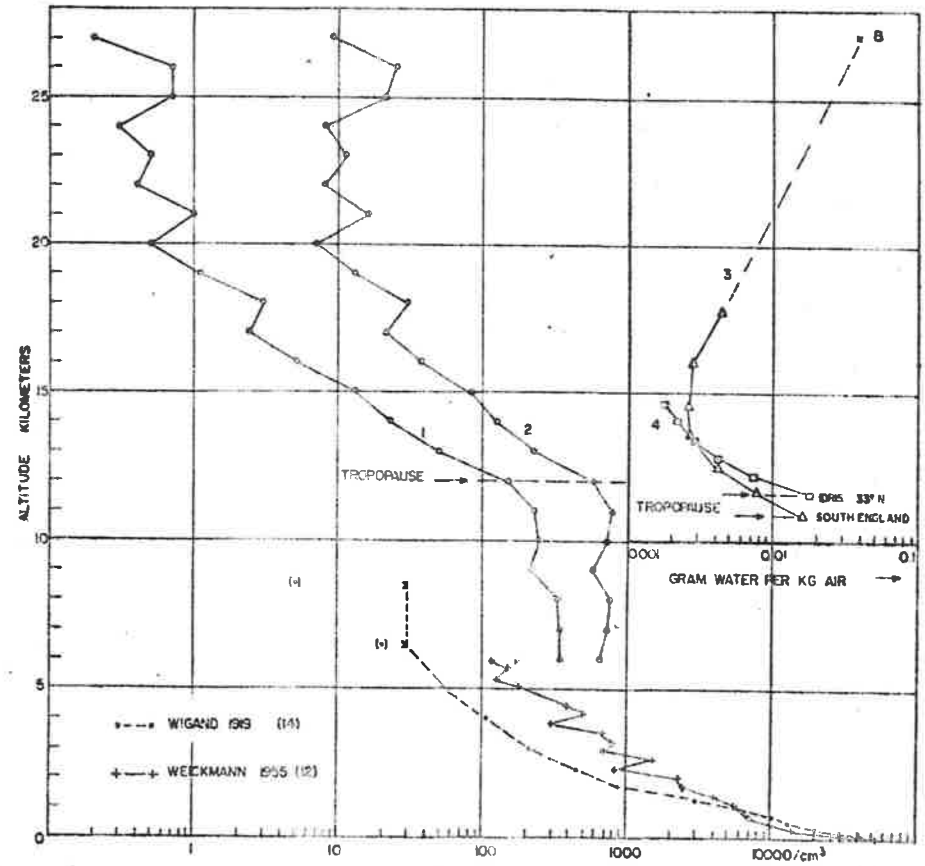

FIGURE 1.4 Vertical profiles of Aitken particles. Curve 1; average of seven flights. Curve 2; Curve 1 at STP (after Junge,1961).

by Eiden (1968) from ground-based sites yielded values of the Junge exponent ν which were larger than values found by direct measurement. As the size distributions calculated from the ground based solar aureole measurements represent average values of the entire atmosphere, Eiden concluded that the value of ν increases with height.

The size distribution results of Blifford and Ringer (1969) using an airborne impactor are shown in Figure 1.5. The slope ν for the giant particles (radii > 1 μ)increases systematically from 2 at the lower levels to approximately 3 at 9 km, and there is a pronounced flattening of the curve in the large particle range (radii between 0.2 and 1.0 μ). In general, the distributions become compressed as the altitude is increased due to the reduction of both the largest and smallest sizes. This is most likely the result of an aging process, as the aerosols are predominantly of terrestrial origin. The smallest aerosols would coagulate, and the largest ones would be reduced in number by sedimentation and capture by rain.

The only in-situ measurements of large particle size distributions in the troposphere using an optical particle counter appear to be those of Rosen (1968, 1969(b)). In contrast to all other measurements, Rosen's results indicate a rapid decrease in exponent ν with height, from 2.5 at ground level to about 1 in the upper levels of the troposphere. However, as the sizes were only divided into two ranges, the determination of a power law exponent could lead to serious errors.

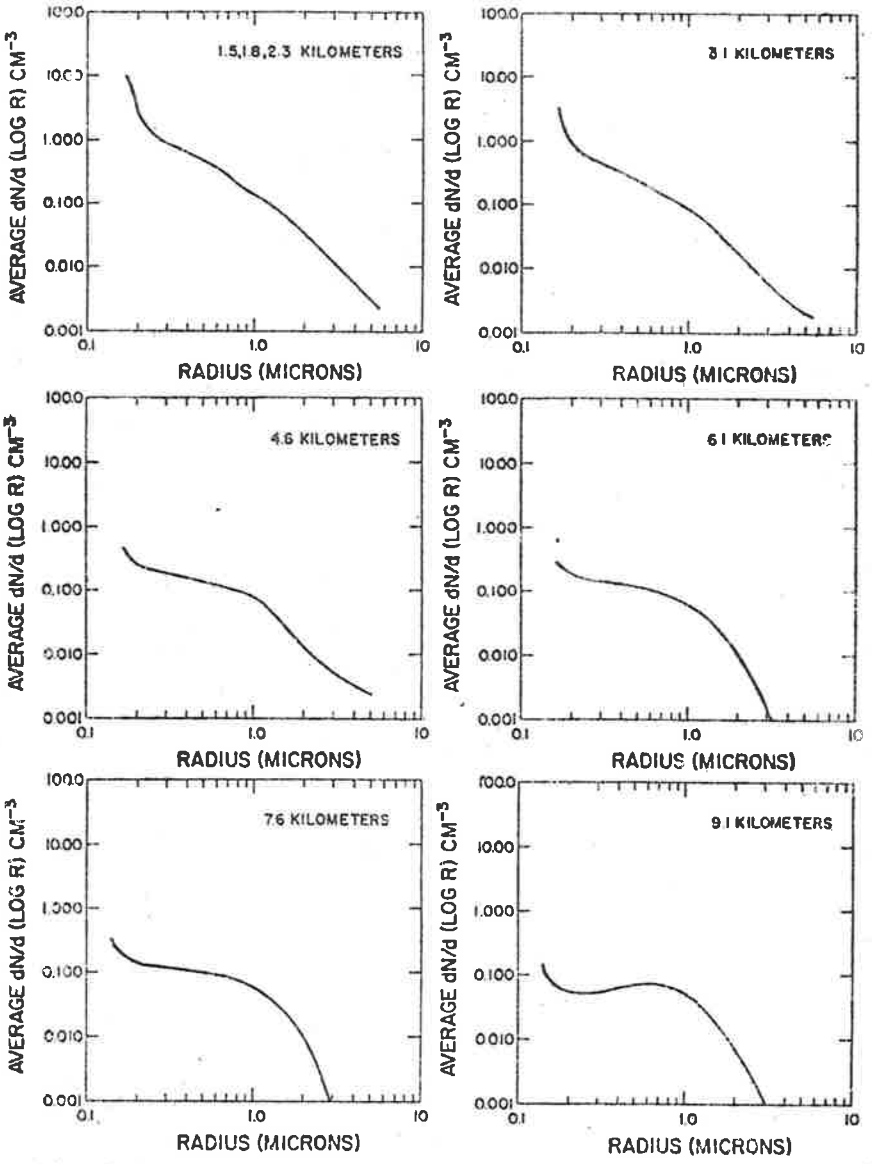

FIGURE 1.5 Average size distributions at various altitudes (after Blifford and Ringer,1969).

In summary, the results of optical and impactor counting experiments are in agreement at ground level, indicating a significant proportion of solid aerosol. Impactor measurements in the troposphere suggest an increase in ν with altitude, consistent with sedimentation effects. Particle number densities in the troposphere measured by optical counters and impactors are in agreement, but the lack of reliable measurements of the size distribution using optical counters gives rise to an uncertainty in the tropospheric size distributions.

1.2.2 Maritime Aerosols

Woodcock (1953) made a detailed study of maritime aerosols in the giant size range, and found that they consist mainly of sea-spray particles. An increase in strength of the wind increases the total concentration of the sea salt, and shifts the upper limit of the distribution to larger particle sizes. Woodcock's results imply that the large sea spray particles are less numerous than the continental aerosols by one or two orders of magnitude. The data in Table 1.1 indicate that Aitken particles show a similar variation between land and sea. For average wind speeds, a Junge power law with $\nu = 3$ can be fitted to the data of Woodcock (1953) for radii between 2 and 10 μ (Junge, 1963). On the basis of a chemical analysis of chloride in maritime aerosols over Hawaii, Junge extrapolated Woodcock's average size distribution curve to less than 0.1 μ, and revealed a peak in the function at about 0.3 μ radius at 80% relative humidity.

Recently Junge et al (1969) measured the size distributions of maritime air masses on the coast of Oregon, U.S.A., using Aitken and optical particle counters. Data were taken at Cape Blanco about 65 metres above the sea on steep cliffs, and in Crater Lake National Park, at an altitude of 2200 metres and about 160 km inland. The area between the two sites is forested, and hence air originating from the north Pacific can be considered uncontaminated. The normal Crater Lake distribution is closest to a power law relation with $\nu = 3.2$, and represents the low - to mid-tropospheric maritime aerosol. The results from Cape Blanco representing the surface maritime aerosol cannot be accurately described by a power law, but $\nu \simeq 2$ is an approximate estimate. By directly comparing the Cape Blanco and Crater Lake distributions, Junge et al were able to separate the pure sea spray component at Cape Blanco, revealing a peak in the distribution at 0.4 μ. Evidently, the sea-spray component becomes insignificant by about 2 km altitude.

The size distribution measured at Crater Lake when subsidence of the air mass occurred is representative of aerosols in the high troposphere, and can be described by a power law with an exponent of approximately 2. The subsidence results are substantially in agreement with size distributions measured at Haleakala, Hawaii (Bullrich et al, 1966) above the trade wind inversion at an elevation of 3050 metres above sea level. The agreement in the results indicates the presence of a rather uniform and widespread upper tropospheric background aerosol. Junge et al (1969) suggest that this aerosol may represent aged continental particles, and that they form the background on which the low level continental and maritime aerosols are superimposed.

It is to be expected that large scale horizontal mixing could give rise to a variety of transitions between the continental and maritime size distributions discussed above, particularly in the coastal areas. In some instances, Twomey (1955) found sea-salt particles as far as 1000 miles inland. On the other hand, residues of continental aerosols are found to be present far out in the open sea, as for instance by Moore and Mason (1954) over the East Atlantic.

1.2.3 Aerosols in the Lower Stratosphere

The average vertical profile of Aitken nuclei measured by Junge (1961) has already been presented in Figure 1.4. The results show a steady decrease in concentration with an increase in altitude above the tropopause, implying that the majority of stratospheric Aitken particles are of tropospheric origin, and enter the stratosphere by mixing. The concentration ranges from 10 cm^{-3} at 15 km to about 1 cm^{-3} at 20 km, where it remains approximately constant with a further increase in altitude. On the basis that Aitken nuclei originate from the troposphere by a turbulent diffusion process, Junge et al (1961) estimated their mean radius to be approximately 0.03 μ.

Measurements of large particle number densities in the stratosphere using the impactor technique (Junge, Chagnon and Manson, 1961; Junge and Manson, 1961) indicate the presence of a broad aerosol layer with a maximum concentration of 0.1 cm^{-3} at an altitude of 20 km. Extensive measurements at latitudes from 60°S to 70°N (Junge and Manson, 1961) suggested a stable stratospheric aerosol layer, constant in time and space. A Junge power law with $\nu = 2$ fits the experimental size distribution results in the size range 0.1 - 1.0 μ, and for radii greater than 1 μ, $\nu \simeq 4$. On the basis of these results, the power law size distribution has been employed in several optical studies of the stratospheric aerosol (e.g. Newkirk and Eddy, 1964; De Bary and Rössler, 1966) in order to deduce the particle concentration and size distribution exponent ν. Concentrations of stratospheric aerosols measured by Mossop (1965) and Friend (1966) using the impactor technique are in agreement with those of Junge, Chagnon and Manson (1961). However, the size distribution obtained by Mossop and Friend peak at 0.3 to 0.4 μ, and can be approximated by the following lognormal function.

$$dN(r)/d(\log r) = C \exp \left[- (\log r - \log r_o)^2/2s^2\right] \qquad (1.4)$$

where C is a constant, r_o the mean radius and s the standard deviation. Dave and Mateer (1968) averaged the results of Mossop and Friend, and deduced that $r_o = 0.35$ μ and $s = 0.30$ (using natural logarithms).

The vertical profiles of large particle concentrations measured by Rosen (1969(a)) using a balloon-borne photoelectric particle counter are shown in Figure 1.6. It has already been noted that Rosen's lower tropospheric concentrations (Rosen, 1969(b)) are in agreement with results of impactor experiments such as those of Blifford and Ringer (1969). However, the stratospheric concentrations measured by Rosen (1969(a)) are more than an order of magnitude greater than the counts deduced by collection experiments, indicating the existence of a considerable proportion of volatile aerosols in the stratosphere. Rosen has reported further evidence of the volatile nature of stratospheric aerosols. When the temperature of the air intake of the optical particle counter was increased above 70°C, the apparent dust concentration abruptly decreased by a factor of 10. The recent measurements reported by Rosen indicate a significant decrease in stratospheric aerosol concentration over the years following the volcanic eruption in Bali in 1963 (Figure 1.7). The rate of decrease is consistent with the removal rate of radioactive debris, but shows large seasonal variations from the average.

The size distribution of stratospheric aerosols measured by Rosen using the optical particle counter is of particular interest. The results indicate an exponential function of the form,

$$dN/d(\log r) = Cr \exp(-4r) \qquad (1.5)$$

where C is a constant. The size distribution peaks at about 0.3 μ radius, and is similar in many respects to the lognormal function discussed earlier.

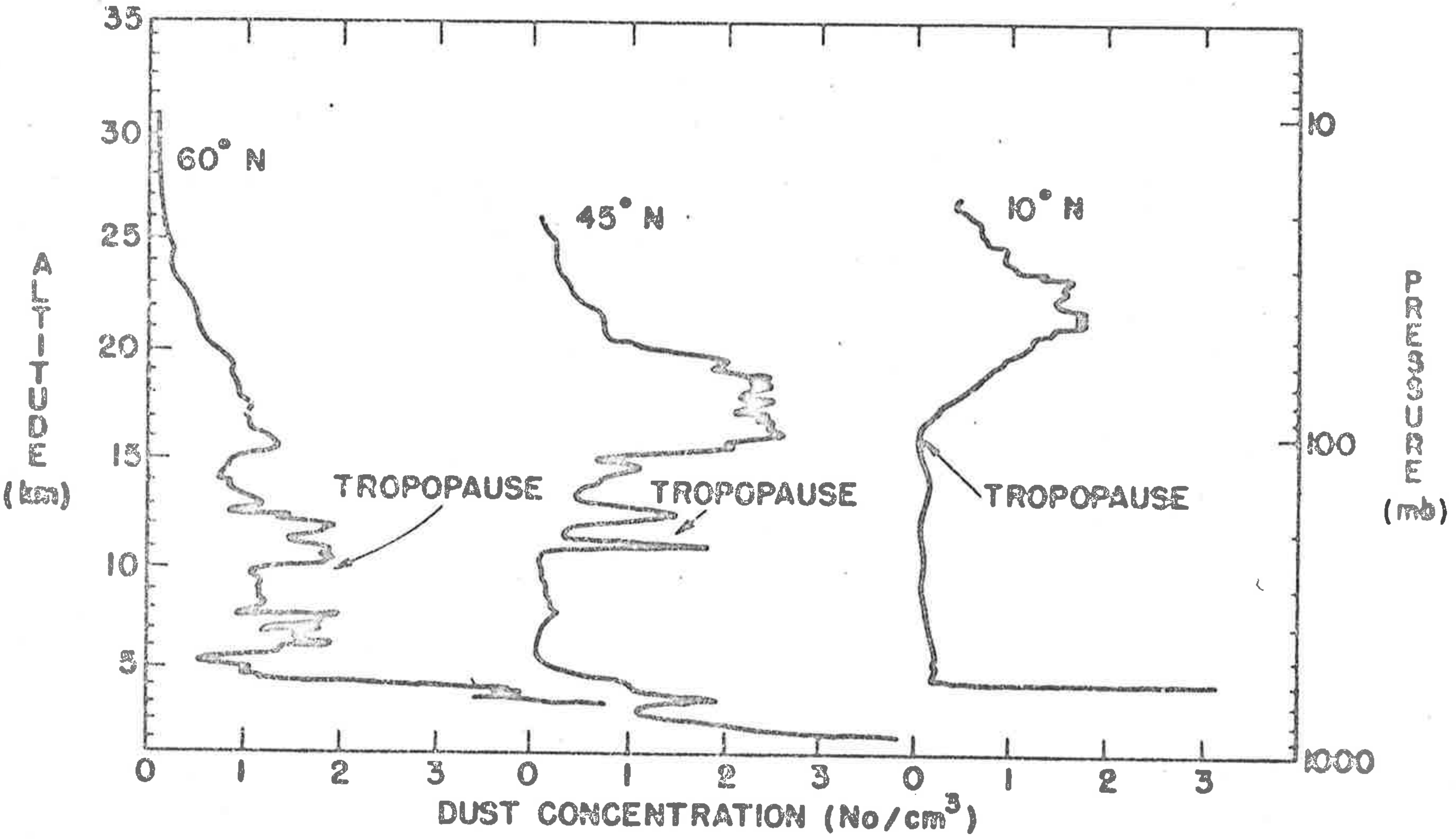

FIGURE 1.6 Vertical profiles of large particle concentration (after Rosen,1969(a)).

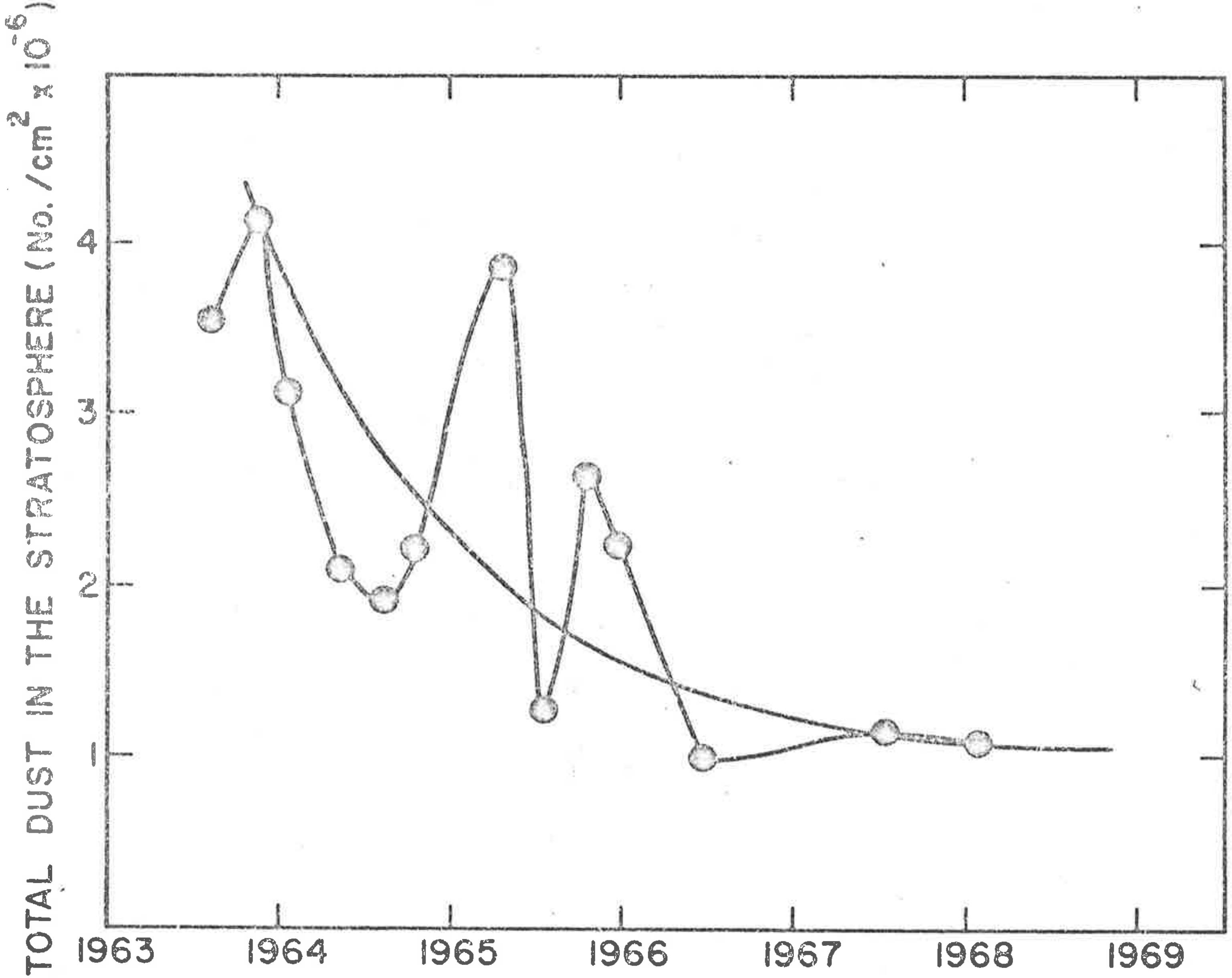

FIGURE 1.7 Reduction in stratospheric aerosol concentration since the Bali eruption in 1963 (after Rosen, 1969(a)).

Thus to date only one satisfactory measurement of the size distribution of the volatile aerosols in the stratosphere has been reported. The consistency of this function with other optical measurements in the stratosphere will be discussed in a later chapter.

Some observations of the stratospheric aerosol indicate extensive horizontal layering which is not detected in many of the sampling experiments, principally because the layers are very thin. Ross (1958) and Simons (1958) photographed the layers from balloons. Newkirk and Eddy (1964) and Newkirk and Kroening (1965) report stratospheric aerosol layers approximately 30 to 100 metres thick from observations of the sunlit sky using a balloon-borne coronograph. The measurements indicate layers with concentrations of aerosols up to twenty times that of the local smoothed concentration. Bigg (1969) has photographed the layers from aircraft and using balloon-borne cameras up to altitudes of 26 km. The observations show the same layers to exist over some 2000 km in latitude, although changes in height and thickness are common. Recent studies by Bigg (1970) indicate that different layers contain completely different types of particles, with varying size distributions.

At high latitudes the region between the dust maximum (15 km) and the tropopause (10 km) is characterised by layers rich in both dust and ozone (Rosen, 1968). The similarity of the dust and ozone profiles in this region indicates that both of these quantities are transported from the same source (Rosen, 1969(c)). As much of the ozone is produced above 15 km, it follows that the dust associated with it must have also come from above 15 km. However, Rosen (1969(c)) reports that the lack of correlation of dust and ozone above 15 km indicates that aerosols are not being mixed downward from above 25 km as is the ozone, which suggests that the source of aerosols at high latitudes is apparently between 15 and 25 km.

1.3 Chemical Composition

The composition of natural aerosols is of importance to the formation of clouds and in determining their origin. It is of particular importance to the optical properties of aerosols in the atmosphere, and a brief review follows.

1.3.1 Tropospheric Aerosols

Dust particles in the troposphere are usually irregular in shape with an admixture of small soot particles and an occasional salt crystal. Studies of growth rate curves of natural aerosols as the humidity is varied indicate that 70 - 80% of the material is insoluble. At high relative humidities, continental aerosols are more characteristic of droplets of a salt solution due to the soluble portion.

Using microanalytical techniques, Junge (1953, 1954, 1956) showed that the soluble fraction of the large particles was essentially composed of NH_4^+ and SO_4^{--} ions, the concentration ratio of which suggests $(NH_4)_2 SO_4$. On the other hand the giant particles showed only small amounts of NH_4^+, and Junge assumed that a considerable fraction of the $SO_4^=$ was bound by other cations. Chloride was found to be present in both size ranges, and the results indicate that chloride particles smaller than 0.8 μ are formed over land. In summarizing the composition of tropospheric aerosols, Junge (1963) concludes that most of the water-insoluble materials in polluted areas are organic substances and ashes. In unpolluted continental atmospheres, the ashes are replaced by mineral dust, such as SiO_2.

Bullrich (1964) has collated the optical refractive indices of materials commonly found for the natural aerosol. In the dry state the average refractive index is about 1.54, but as the relative humidity is increased above 70% the refractive indices of the soluble materials tend towards that of water (1.33).

Sea-salt particles in pure maritime air contain practically no insoluble components, and the sharp phase transition in the growth curve at 73% relative humidity can be used to identify them (Twomey, 1954). However, with decreasing humidity, dissolved salts do not recrystallize until much lower relative humidities are reached, and the solution is considerably supersaturated. NaCl, for example, does not recrystallize until the relative humidity is about 40%. In the Aitken size range, the normal phase transition of crystals occurs at lower humidities due to the curvature of the droplets.

As the relative humidity approaches 70%, the size distribution of continental and maritime aerosols is modified, and the lower size limit tends to increase. Taking into account the corresponding change in refractive index, humidity effects are of considerable importance to the optical properties of the atmosphere, as indicated by the many references to this effect in the literature (e.g. Rozenberg, 1967; Garland, 1969).

1.3.2 Aerosols in the Lower Stratosphere

All of the collection measurements of stratospheric aerosols indicate that sulphur is the most prominent element present. Because of the hygroscopic nature of the particles, Junge, Chagnon and Manson (1961) assumed the sulphur is most likely present as sulphate, and on the basis that the vertical profile of large particles peaks in the stratosphere, they concluded that the particles are formed in situ. They proposed a mechanism whereby H_2S and SO_2 are introduced by diffusion through the tropopause, and subsequent photochemical oxidation forms the sulphate. This mechanism is also consistent with the small variations observed in time and space of the aerosol layer (Junge and Manson, 1961). Friend and Sherwood (1961) identified ammonium sulphate and ammonium persulphate by electron diffraction analysis of stratospheric aerosols collected under similar conditions. Mossop (1965) found that within each sulphate particle there exists at least one smaller insoluble particle that presumably acts as a nucleus upon which the ammonium sulphate is deposited in the stratosphere.

The collection measurements to date suggest that the refractive index of ammonium sulphate (1.52) is applicable to stratospheric aerosols. However, the measurements of Rosen (1964, 1968, 1969(a)) discussed in Section 1.2.3 suggest a significant volatile component in the stratosphere. The chemical composition of the volatile component is likely to be sulphuric acid or water vapour, the refractive index of which approaches 1.33.

1.4 Aerosols above 30 km

Observations of noctilucent clouds (Fogle, 1966) at high latitudes indicate the presence of aerosols at heights close to the mesopause. Polarization and spectral measurements (Deirmendjian and Vestine, 1959; Witt, 1960) have shown that the majority of the particles have sizes less than the wavelengths of light, and that if the particles follow a Junge size distribution law, the exponent ν must be greater than 2.

Results of rocket-borne experiments by Hemenway, Soberman and Witt (1964) and Soberman and Hemenway (1965) showed that the particle concentration in a vertical column through the noctilucent cloud display was at least 1000 times greater than in the case when no clouds were observed. Table 1.2 shows the particle characteristics observed.

TABLE 1.2

	Cut-off Radius (microns)	Average Number Density (m^{-3})	Size Distribution Exponent ν
NLC Display	.02	4×10^6	3 - 4
No Display	.02	4×10^3	2

In both cases the smallest radius was 0.02 μ whereas the exponent of the power law describing the size distribution changed from 2, when no display was observed, to 3 - 4 during a noctilucent cloud display. The largest size observed was about 0.5 μ radius.

The noctilucent cloud particles are mainly of iron, nickel and silicon, and some show evidence of having been ice coated.

In the region 30 - 70 km, there is little evidence in support of the existence of aerosols. Twilight sky brightness measurements of Volz and Goody (1962) are interpreted as indicating a constant background turbidity of 0.2 for red light in this region. Dunkleman, Dave, Mateer and Evans (1968) postulate a narrow aerosol layer at about 40 km altitude in order to explain the colours of the twilight sky seen by astronauts. However, lidar observations (e.g. Kent, Clemesha, and Wright, 1967) have not detected any significant aerosol layers in this altitude region.

1.5 Remote Optical Probing of the Upper Atmosphere

Many of the properties of aerosols in the upper atmosphere discussed in the previous sections have been determined using vehicle borne equipment, whereby the particles are either collected for subsequent analysis in the laboratory, or measured in situ by optical counters. The inability of the collector experiment to detect the volatile component limits its use somewhat for stratospheric measurements, and highlights the importance of optical methods. It is likely that the vehicle borne optical counter of the type used by Rosen (1964, 1968, 1969(a)), but perhaps modified to enable more accurate measurements of the size distribution, will make significant contributions to atmospheric studies in the future.

The vehicle borne experiment, however, is both costly and complicated by experimental difficulties, and progress has been relatively slow. On the other hand, frequent measurements of atmospheric properties have been made using ground based optical techniques, of which twilight and searchlight experiments, and more recently laser radar measurements are most common. Remote optical measurements, however, require clear weather and are more difficult to interpret. Nevertheless, the disadvantages are far outweighed by the advantages. In what follows, some of the more important ground based optical experiments will be described.

1.5.1 Twilight Experiments

As the sun sets below the horizon, the earth's shadow gradually rises upward, and the lower atmospheric layers, submerged in shadow, no longer contribute to the sky brightness. The scattered light comes progressively from the higher layers which are still illuminated by direct sunlight, and consequently the brightness of the sky rapidly decreases due to the reduction in air density with height (Figure 1.8(a)).

The twilight phenomenon has been used by scientists as far back as the 11th century to deduce properties of the upper atmosphere. It was not until 1923, however, that the purely empirical observational approach was replaced by a theoretical approach (Fesenkov, 1923). Since then, many contributions to the development of twilight research have been made (Rozenberg, 1966). Essentially, the sun acts as the source of light, and height resolution is achieved by means of the earth's shadow, which progressively sweeps through higher layers of

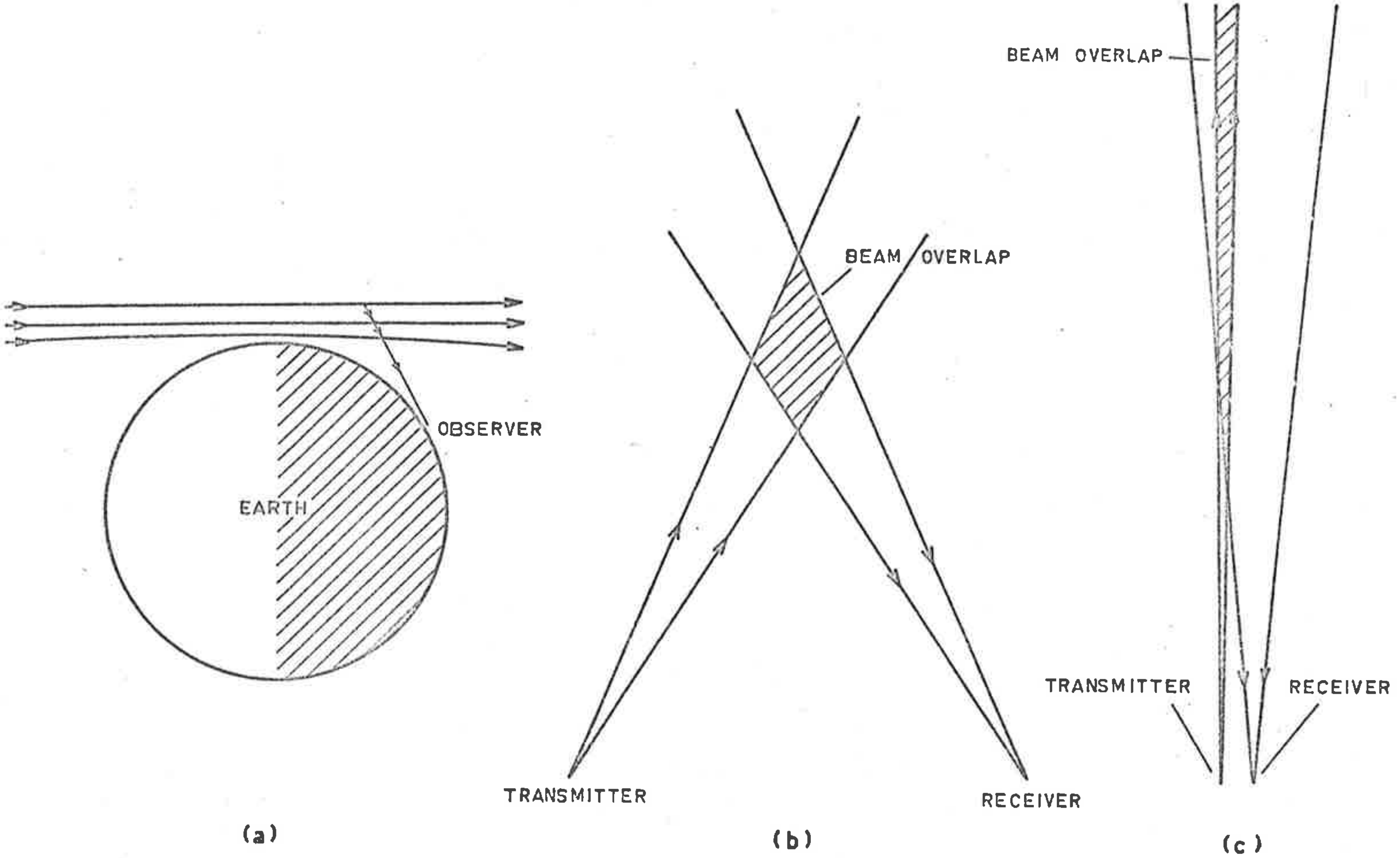

FIGURE 1.8 Geometry of remote optical probing systems. (a) twilight experiment; (b) bistatic system; (c) monostatic system.

the earth's atmosphere. Many workers (e.g. Gruner, 1942; Dave and Mateer, 1968) have ascribed the phenomenon of "purple light" to the stratospheric aerosol layer, and Volz and Goody (1962) have deduced scattering coefficients of the aerosols. Rozenberg (1966) has reported that the twilight method is ideal for the sounding of the molecular component of the atmosphere above 30 km.

The studies of Rozenberg (1966) show, however, that deduction of atmospheric quantities from twilight measurements is exceedingly complicated. He concludes that the results below about 30 km are difficult to analyse because of the interrelation between the transmission and scattering characteristics of the atmosphere in this region. In addition, the twilight experiment requires cloudless skies up to hundreds of kilometers from the observation site, thus reducing the number of possible measurements. Thus alternative optical probing methods have been investigated, and these are described in subsequent sections.

1.5.2 Searchlight Experiments

The geometry of the searchlight experiment is shown diagramatically in Figure 1.8(b). The searchlight beam is directed upwards, and either a photographic or photoelectric detector, situated some distance from the searchlight, scans the beam and records the intensity as a function of height. Most of the systems are of the bistatic type as shown in Figure 1.8(b). Using a photographic recorder, Hulburt (1937) obtained density measurements to altitudes of 28 km. Later, Johnson et al (1939) improved the sensitivity of the experiment by modulating the intensity of the beam, and a photoelectric receiver was used. Rayleigh scattering was measured up to heights of 34 km. This experiment was repeated by Elterman (1954, 1966) and Elterman et al (1969), and results up to altitudes greater than 60 km have been obtained, showing the existence and variation of the stratospheric aerosol layer.

The bistatic configuration of the searchlight experiments described above complicates the experimental work, as difficulties occur in aligning the receiving and transmitting beams, and it is difficult to know the exact extent of the overlap. Long times are also needed to obtain complete profiles. Friedland et al (1956) attempted to overcome these difficulties by using a pulsed searchlight system, in which transmitter and receiver are located in proximity, forming a "mono static" system (Figure 1.8(c)). The altitude limit of the equipment, however, was approximately 40 km.

1.5.3 The Laser Radar

The laser was developed a few years after the monostatic experiments of Friedland et al (1956), and apart from the work of Elterman, has almost replaced the searchlight beam as an optical probe. The advantage of the laser are its monochromicity and much narrower angular divergence, which has enabled the background noise received to be reduced by many orders of magnitude. Due to the short duration of the laser pulse, the monostatic system is normally used.

Since the early work of Fiocco and Smullin in 1963, several laser radar systems have been developed. Recently Wright et al (1969) have reported laser radar measurements to heights approaching 100 km. To date the laser radar offers the most suitable and reliable method of optically probing the upper atmosphere.

CHAPTER TWO

THE LASER RADAR

Figure 2.1 shows the laser radar equipment installed inside the mobile instrumentation van. The principle of the laser radar technique is similar to that of ordinary radar in that a pulse of energy is emitted and the back-scattered signal is detected and its intensity measured as a function of range. The laser radar constructed at Adelaide, South Australia, is directed vertically, and the scattered energy is measured as a function of height. A brief review of the equipment is given in this chapter.

It is convenient to discuss the laser radar in terms of the transmitter and receiver separately. The transmitter consists of a laser and collimator, and the receiver is comprised of a telescope and photoelectric detector system.

2.1 Transmitter

A simplified diagram of the transmitting system is shown in Figure 2.2(a), and a block diagram of the electronics is given in Figure 2.3.

2.1.1 Laser Generator

The main parameters of the laser generator are listed in Table 2.1. The laser element is a ruby rod (15 cm long by 8 mm diameter) having a Brewster face at one end and a total internally reflecting end at the other. The interferometer or optical cavity is formed between the

FIGURE 2.1 The laser radar equipment installed inside the mobile instrumentation van.

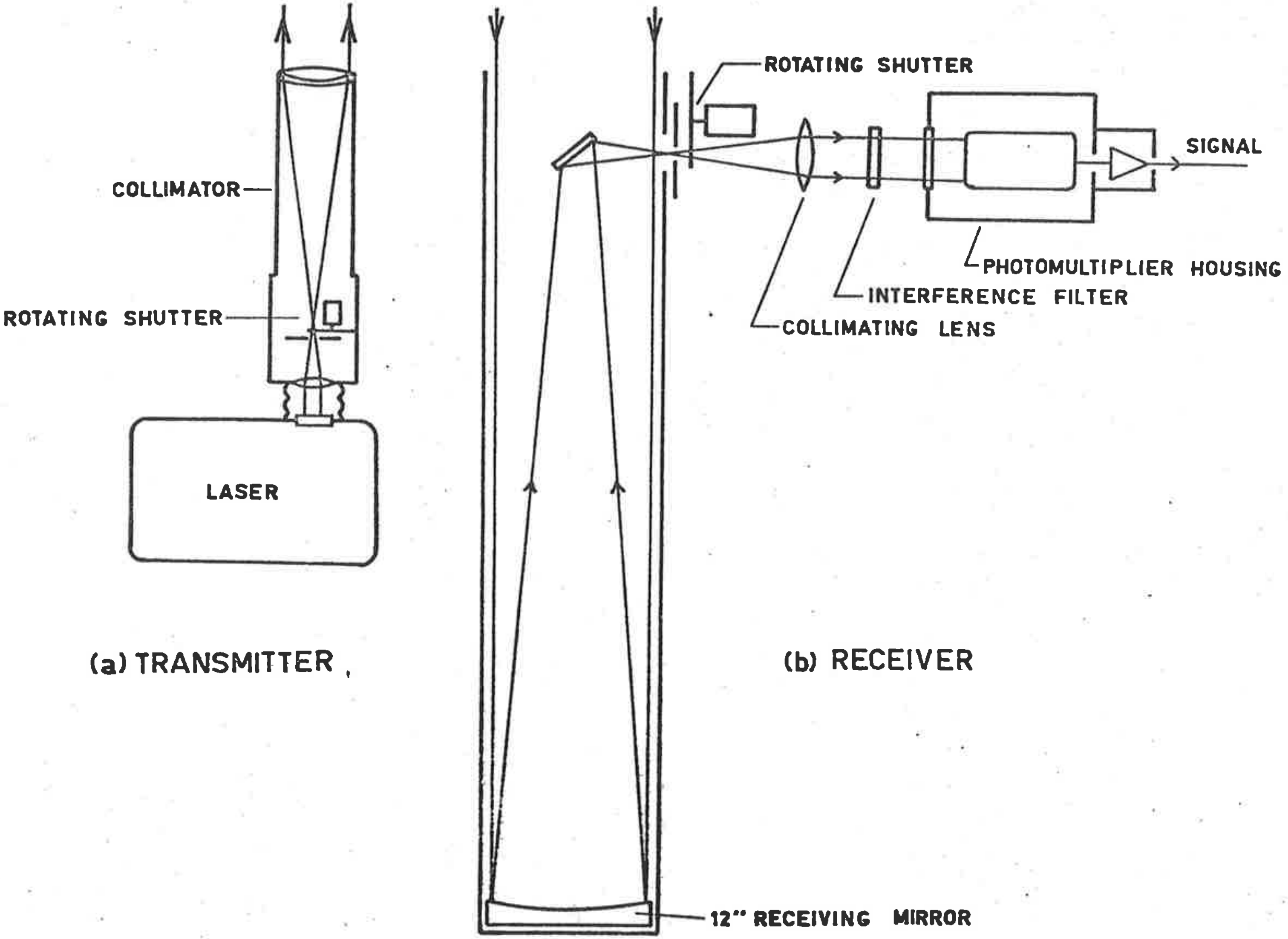

(a) TRANSMITTER

(b) RECEIVER

FIGURE 2.2 Essential components of the laser radar.

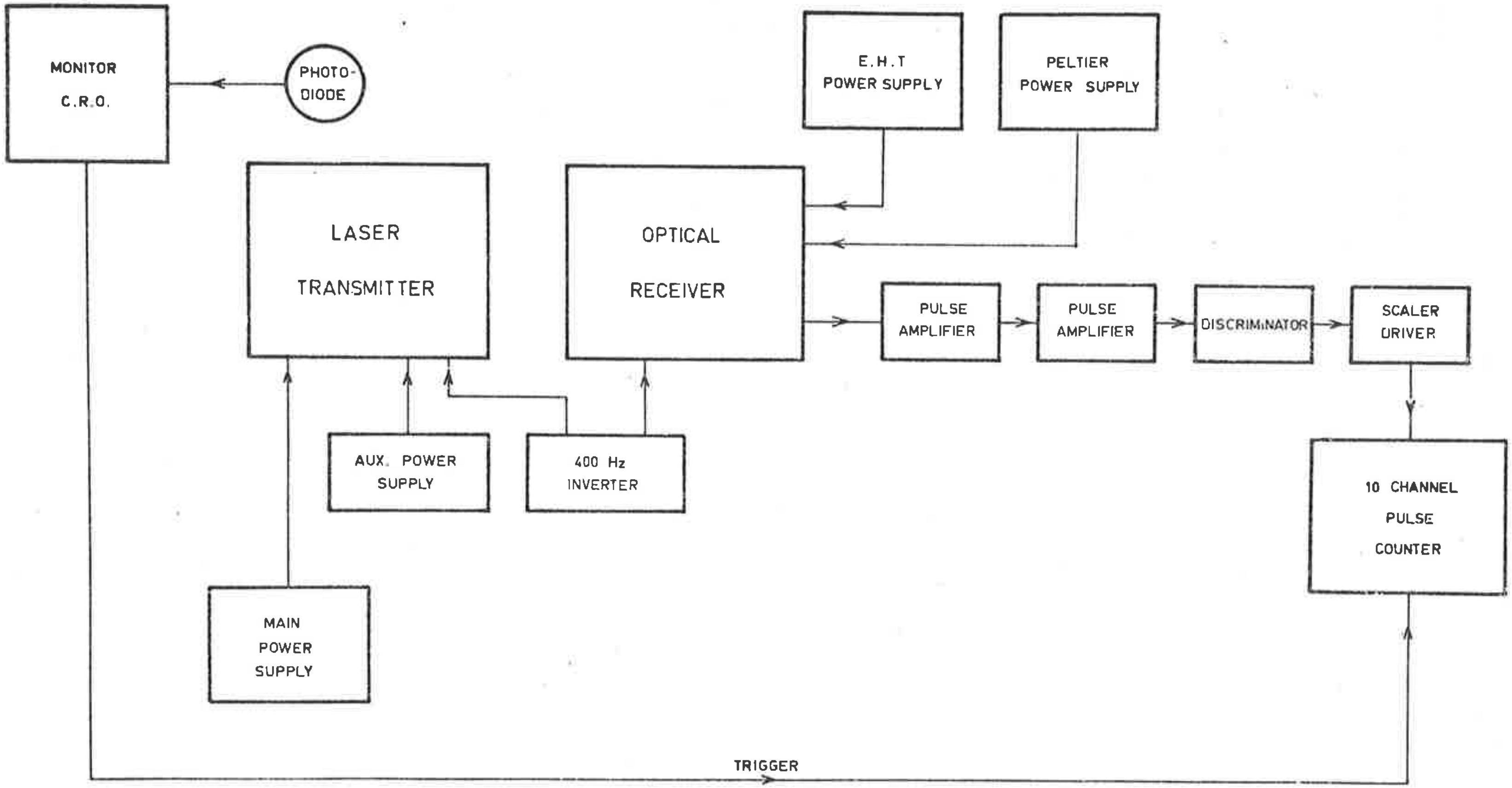

FIGURE 2.3 Block diagram of laser radar electronics.

total internally reflecting end of the ruby, and an optical flat made of sapphire having 16% reflectivity. "Q" switching is achieved by rotating a prism at 12000 rpm within the interferometer. The prism also rotates the beam through 90 degrees (see Figure 2.4). The Q-switch is driven by a small synchronous hysteresis motor which is in turn supplied by a 400 Hz inverter. A magnetic pick-up monitors the rotation of the Q-switch and provides synchronisation between triggering of the flash tube and prism rotation.

TABLE 2.1

Parameter	Numerical Value
Wavelength	0.6943 Å
Energy per pulse	0.2 J
Pulse length	0.5 μs
Beamwidth (after collimation)	1 mrad
Pulse repitition rate	24 min^{-1}

The ruby rod is at one focus of an elliptical cavity, and is optically pumped by a FX55 Xenon flash tube at the other focus of the cavity. Both the ruby rod and flash tube are cooled by passing water through glass envelopes, and the complete laser is enclosed in a gas-tight cover, and operates in an atmosphere of dry nitrogen. The nitrogen is necessary to prevent oxidation of the aluminised surface of the elliptical cavity, and to prevent condensation of moisture on the cooling jackets. The nitrogen is supplied

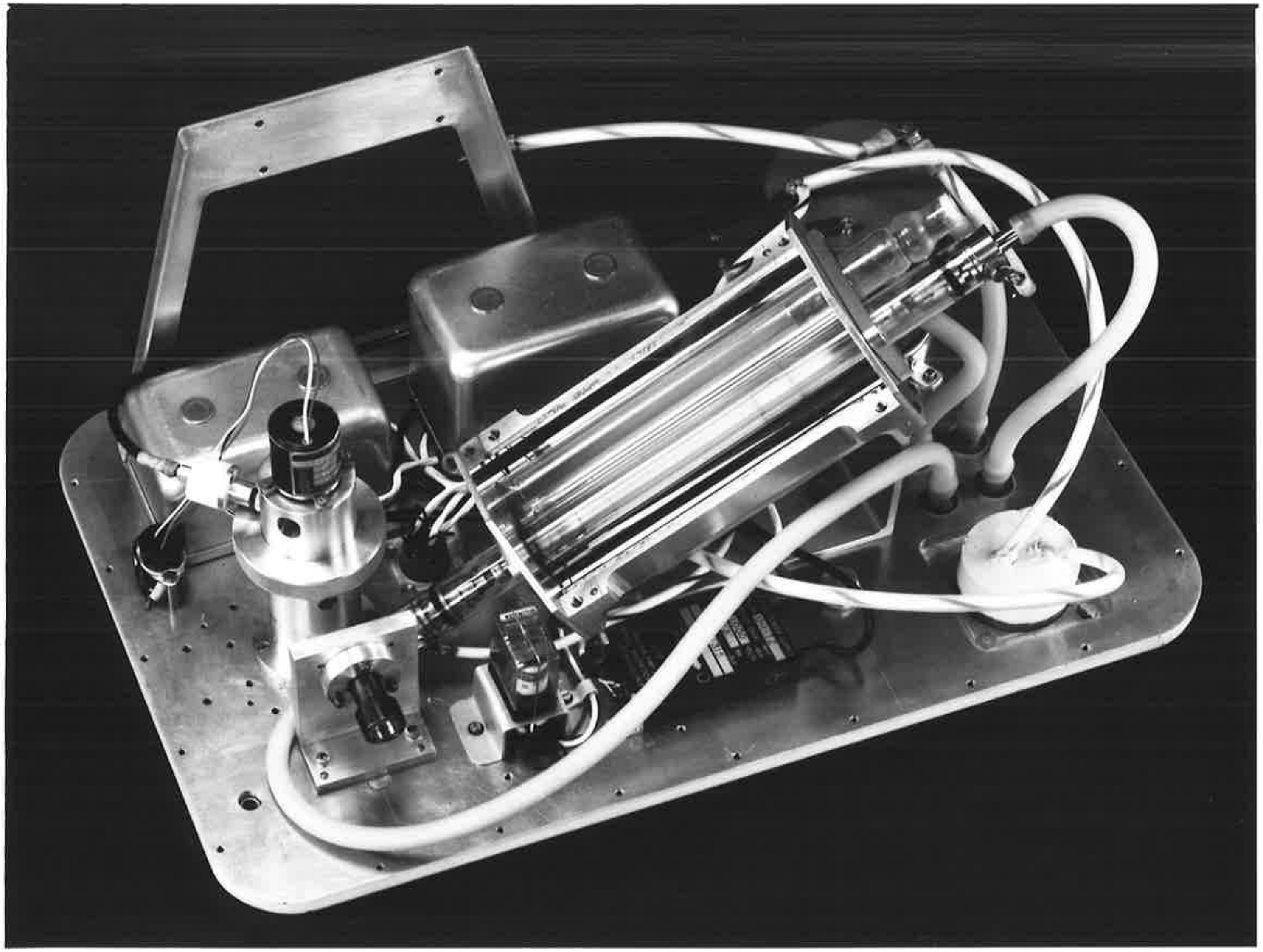

FIGURE 2.4 The laser, with cover removed.

from a standard 220 c. ft. cylinder of industrial dry nitrogen and the small flow rate is controlled by a medical oxygen regulator. A flow gauge and pressure safety valve are also included.

2.1.2 Laser Power Supply

A power supply delivers approximately 650 joules of electrical energy at 2.3 KV in a rectangular pulse about 0.3 milliseconds in duration to the flash tube. Delay and triggering circuits are incorporated into the supply to enable the flash tube to be triggered at the appropriate point in the Q-switch cycle.

The electrical energy is initially stored in capacitors of a pulse frequency network. The charging of the capacitors is monitored and interrupted by a Schmitt trigger circuit when the preset energy has been reached. In order to fire the laser, the delay and triggering circuits are activated by a manual push-button control, or by means of an automatic mode of operation which immediately begins the charging process after the previous laser firing. The highest repitition rate at present is 24 cycles per minute, and is limited by current capabilities of the power supply.

2.1.3 Cooling System

Cooled water is supplied to the ruby and flash tube by two separate pumping systems. Standard plastic containers and tubing are avoided because of the risk of contaminating the water supplies with plasticisers which dissolve more readily in high purity water. Hence water in both systems is delivered through a combination of nylon and natural rubber tubing. Initial tests with "mono" pumps indicated that small particles of neoprene were being worn from the stator and carried into the water jackets. The high intensity radiation from the flash tube caused the neoprene to decompose and form a brown deposit on the walls of the jackets, thus decreasing the amount of excitation energy reaching the ruby. Centrifugal pumps constructed of nylon-impregnated bakelite are now used in which contact between rotor and stator is minimised. The water cooling unit has since proved satisfactory and no deposits have formed in the glass jackets over an operational period of 18 months.

The water used to cool the flash tube is at ambient temperature and is de-ionized, since it flows over the high-voltage terminals of the tube. The storage tank is constructed of stainless steel in order to minimise ionic contamination. The ruby is cooled to a temperature of 4°C by a separate supply and controlled by two thermostats to an accuracy of $\pm 1^{\circ}$C. The water in both systems is pumped at a rate of about 1 litre per minute, and experiments have shown that excess heat energy from the flash tube is adequately dissipated.

2.1.4 Characteristics of the Laser Output

The laser output normally consists of three closely-spaced narrow pulses of light. The total duration of the pulse train is 0.5 μs and the overall energy is 0.2 joules. The angular divergence of the beam is 10 mrad.

As the input energy to the flash-tube is decreased and approaches the threshold value for laser action, the number of pulses reduces to one and the angular divergence decreases due to the suppression of off-axis modes. Some of the off-axis modes are due to the rotation of the Q-switch prism, and the angular divergence can be reduced slightly by tilting the sapphire flat, which acts as one end of the laser interferometer, about an axis parallel to that of prism rotation. This causes a majority of the energy to be released in an off-axis mode earlier than the axial mode. The late off-axis modes are therefore suppressed due to insufficient population of the excited state.

The laser generator was originally designed to produce pulses of 1 joule total energy. This specification is unfortunately unattainable. At output energies near 1 joule the Q-switch prism has a very limited life, suffering severe pitting on the total internally reflecting face after 50 - 60 shots. It appears that the prism is unable to withstand the high energy density of the laser beam at these energies. It is of interest to note that most laser generators of comparative outputs have ruby rods of considerably larger cross-sections, thus decreasing the peak energy densities. The output capability of the laser has therefore been derated to 0.2 joules, and a prism life in excess of 30,000 shots has been obtained.

The output energy of the laser can be measured by inserting a right angled prism in the path of the beam, which directs the beam to a ballistic thermopile. At the present time there is no facility to measure the output energy each time the laser is fired during the course of sounding the atmosphere. It will be seen in the following chapter, however, that the particular method of data analysis used in the present work does not require absolute measurement.

The wavelength of the radiation generally lies between 6942 and 6943 Å, the exact value depending on the temperature of the ruby. Up to the present time the ruby temperature has been maintained at 4°C, giving rise to a wavelength of 6942 Å. According to the results of Long (1966), this wavelength is adjacent to an absorption line due to water vapour in the atmosphere (Figure 2.5). It was initially feared that a temperature rise in the ruby during irradiation by the flash tube might cause the emitted wavelength to coincide with the absorption line. However, no significant reduction in signal has been noticed during experimental observations. Moreover, theoretical calculations of the expected signal are within 60% of the observed values.

2.1.5 The Collimator

As noted earlier, the collimator reduces the laser output beam divergence. The advantage of a small angular divergence lies in the fact that the receiver field of view can be minimised, thus reducing the noise contribution from the sky background radiation.

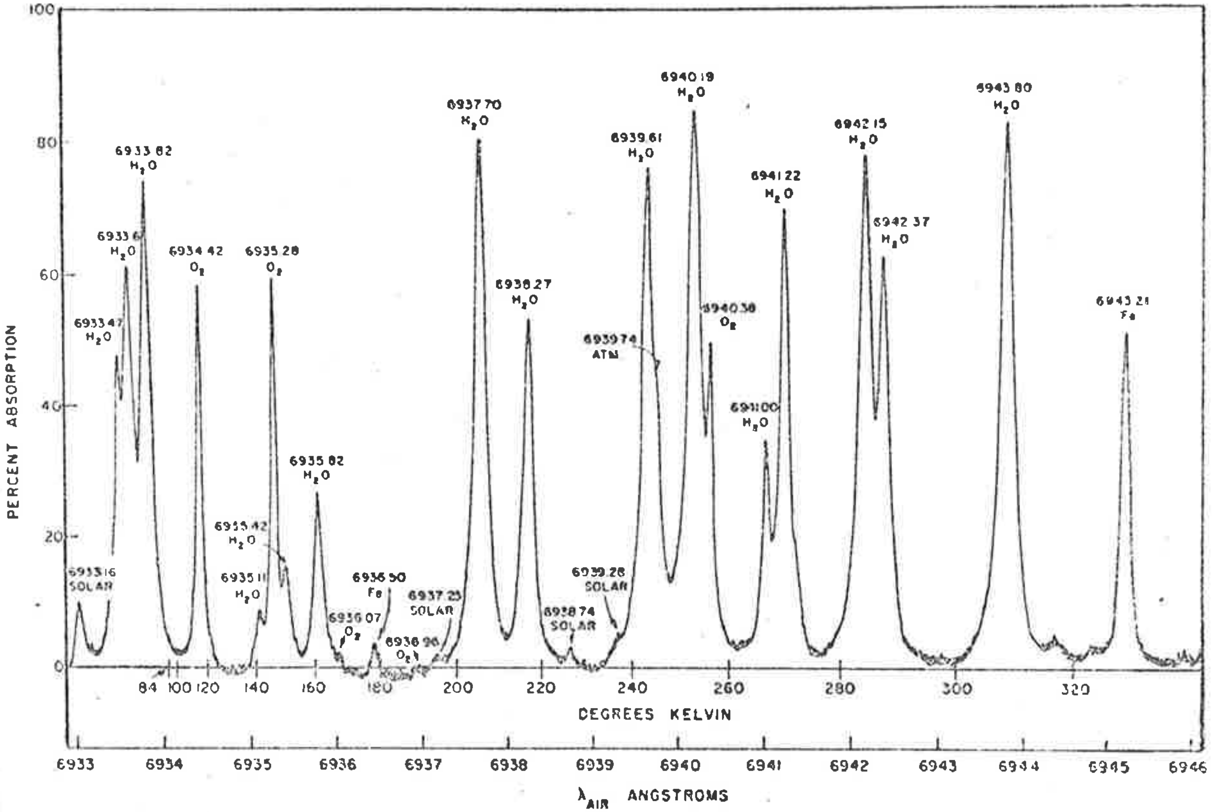

FIGURE 2.5 Atmospheric absorption spectrum between 6934 and 6945 Å using the sun as a source (after Long , 1966).

A rotating shutter positioned at the focus of the entrance lens of the collimator is used to cut off the long duration fluorescent emission from the ruby following the main laser pulse. This, when scattered from the lower regions of the atmosphere, gives rise to a signal intensity of the same order of magnitude as the main pulse when scattered from the upper atmosphere. The rotating shutter is a disc of diameter approximately 6 cms, and having four 5 mm slots equally spaced around the circumference. This is rotated at 12,000 rpm by a synchronous hysteresis motor which is in turn driven by the same inverter that supplies the Q-switch motor.

The phase of the shutter is monitored by a small optical pickup, and adjusted relative to the phase of the Q-switch prism so that the shutter is completely closed soon after emission of the main laser pulse. The relative phase of the shutter rotation with respect to rotation of the Q-switch is monitored by displaying the waveform of the magnetic pickup in the Q-switch and the output of the optical pickup on a dual-beam oscilloscope. The shutter phase is adjusted mechanically by bodily rotating the motor about the shutter rotation axis. This method has proved simpler and just as reliable as altering the phase of the driving waveform.

The closing time of the transmitter shutter is 20 μs, and the jitter in phase in relation to the Q-switch has a maximum value of 20 μs. Thus the maximum time difference between emission of the laser pulse and complete closing of the transmitter shutter is 40 μs. Results of an experiment to measure the contribution from the fluorescent tail showed that the intensity of the fluorescence is less than 10^{-6} of that of the main laser pulse. Calculations using a model aerosol atmosphere show that scattering from such a fluorescent tail will be less than 5% of the main signal from the height being studied provided its length is less than 50 μs.

In order to reduce the closing time of the transmitter shutter, a positive entrance lens was used in the collimator and the shutter was placed at its focus. A negative entrance lens would have resulted in a prohibitively large laser beam cross-section. Tests have shown no significant loss of energy which could be attributed to dielectric breakdown of the air at the focus of the positive lens. The primary lens of the collimator is a simple plano-convex lens, as it was feared that a cemented compound lens would deteriorate under the high density irradiation of the laser beam. Chromatic aberration is absent because the laser beam is monochromatic, and the shape of the lens minimises spherical aberration.

A thin wire stretched across the exit aperture of the collimator scatters a small fraction of the beam to a high speed photodiode. The photodiode output waveform is displayed on an oscilloscope, allowing a constant visual check to be kept on the laser pulse shape during operation. The leading edge of the oscilloscope's time-base gating voltage is used to trigger the recording system.

2.2 The Receiver System

2.2.1 The Optical Receiver

The parameters of the optical receiver are listed in Table 2.2, and a simplified diagram is shown in Figure 2.2(b).

TABLE 2.2

Parameter	Numerical Value
Area of receiving mirror	0.073 m^2
Field of view	2 - 5.4 mrad
Quantum efficiency of photomultiplier	0.03
Filter bandwidth	8.5 Å
Minimum noise level from photomultiplier	120 pulses sec^{-1}

The scattered light is gathered by a 30 cm diameter, 1.8 m focal length parabolic mirror, and directed by a diagonal flat to an aperture which defines the field of view of the receiver. The size of the aperture is adjustable, and for high altitude work is set to 3.5 mm, which corresponds to a field of view of 2 mrad. The largest diaphragm size is 9.7 mm, giving a field of view of 5.4 mrad. The position of the aperture can be accurately adjusted by means of micrometer screws to align the receiver's field of view with the transmitted beam.

Immediately behind the aperture is a rotating shutter, whose function is to block the receiver for a short period following each laser firing. If this were not done, the intense scattering from the first few kilometres of the atmosphere would lead to overloading of the photomultiplier, and a consequent increase in the noise count. This shutter is also synchronised with the laser Q-switch, and phased so that the receiver aperture is completely uncovered by the time the scattered light has returned from the lowest level of the height range being studied. The receiver shutter is powered by the same inverter that supplies the Q-switch and transmitter shutter motors, and is phased by a method similar to the phasing of the transmitter shutter described earlier. The shutter rotates at 24,000 rpm, resulting in an opening time of 30 μs. Due to jitter in rotation of the Q-switch, the effective opening time of the receiver shutter is increased to 50 μs, which corresponds to a sounding height of 7.5 km. Thus when the shutters are in operation, the receiver cannot be used for atmospheric soundings less than about 8 km. However it is possible to study the lower layers without the receiver shutter (see Section 2.2.2.2).

The light passing through the aperture is collimated by a lens of 12.7 cm focal length and then passed through an interference filter to the detector. The interference filter has a bandwidth of 8.5 Å and a peak transmission of 45%. The filter is tuned to the laser wavelength by tilting it with respect to the beam axis by means of a cam and rotating shaft. The method adopted to tune the filter is as follows. After cooling the ruby to the normal operating temperature, the laser is fired, and a small fraction of the collimated beam is scattered into a fibre optics bundle, or light pipe, by the thin wire stretched across the exit aperture of the collimator. The other end of the light pipe is placed near the diaphragm of the telescope and directed towards the interference filter and photomultiplier. It is necessary to attenuate the light by a factor of 100 to prevent overloading of the photomultiplier. The relative intensity of the laser light reaching the photomultiplier after passing through the interference filter is monitored on a storage oscilloscope. The laser is fired repetitively, and the filter is tuned by optimising the output from the photomultiplier.

The detector is an E.M.I. type 9558B photomultiplier having a photocathode of the S-20 class. In the wavelength region of 0.7 μ this photocathode appears to have the highest quantum efficiency of those currently available, a value of 0.03 being typical. The photomultiplier is cooled by a Peltier battery in order to reduce the dark count rate. The hot side of the Peltier battery is cooled by water at 4°C from the laser cooling system, and the battery is then capable of lowering the temperature of the photomultiplier to -15°C. The dark count at this temperature is 120 pulses/sec, compared to 1900 pulses/sec at 20°C. The photomultiplier and Peltier battery are contained in a thermally insulated housing, the front window of which is an evacuated cylindrical glass cell. The front glass surface of the cell remains at ambient temperature and is free of condensation. The photomultiplier is surrounded by "conetic" material to provide magnetic shielding. The tube is operated at a gain of 2000 amps/lumen, the maximum recommended by the manufacturer.

After being individually aligned optically in the laboratory by standard collimation techniques, the transmitter and receiver are rigidly mounted on a heavy metal framework. The final alignment of transmitter and receiver beams is carried out after installation of the equipment. A subsidiary optical system consisting of a 9 cm diameter and 64 cm focal length lens, and aluminium foil mounted at its focal plane, is capable of sliding on accurately machined guide rails placed above the transmitter and receiver (Fig. 2.6). To carry out the alignment, the sliding lens is placed over the transmitter and the laser fired, producing a small hole in the aluminium foil. The lens assembly is then moved over the receiver aperture, making sure that the angular orientation with respect to the optical axis of the transmitter is not altered. The orientation is monitored by means of two accurate spirit levels, and adjusted by three screw motions at the base of the lens platform. The small hole in the aluminium foil is illuminated from above, and the field of view of the receiver is adjusted so that the image of the hole, viewed with a low power microscope, is central in the receiver aperture. Coarse adjustments are made by tilting the main mirror of the receiver, and fine adjustments are made using the micrometer screws which move the receiver diaphragm.

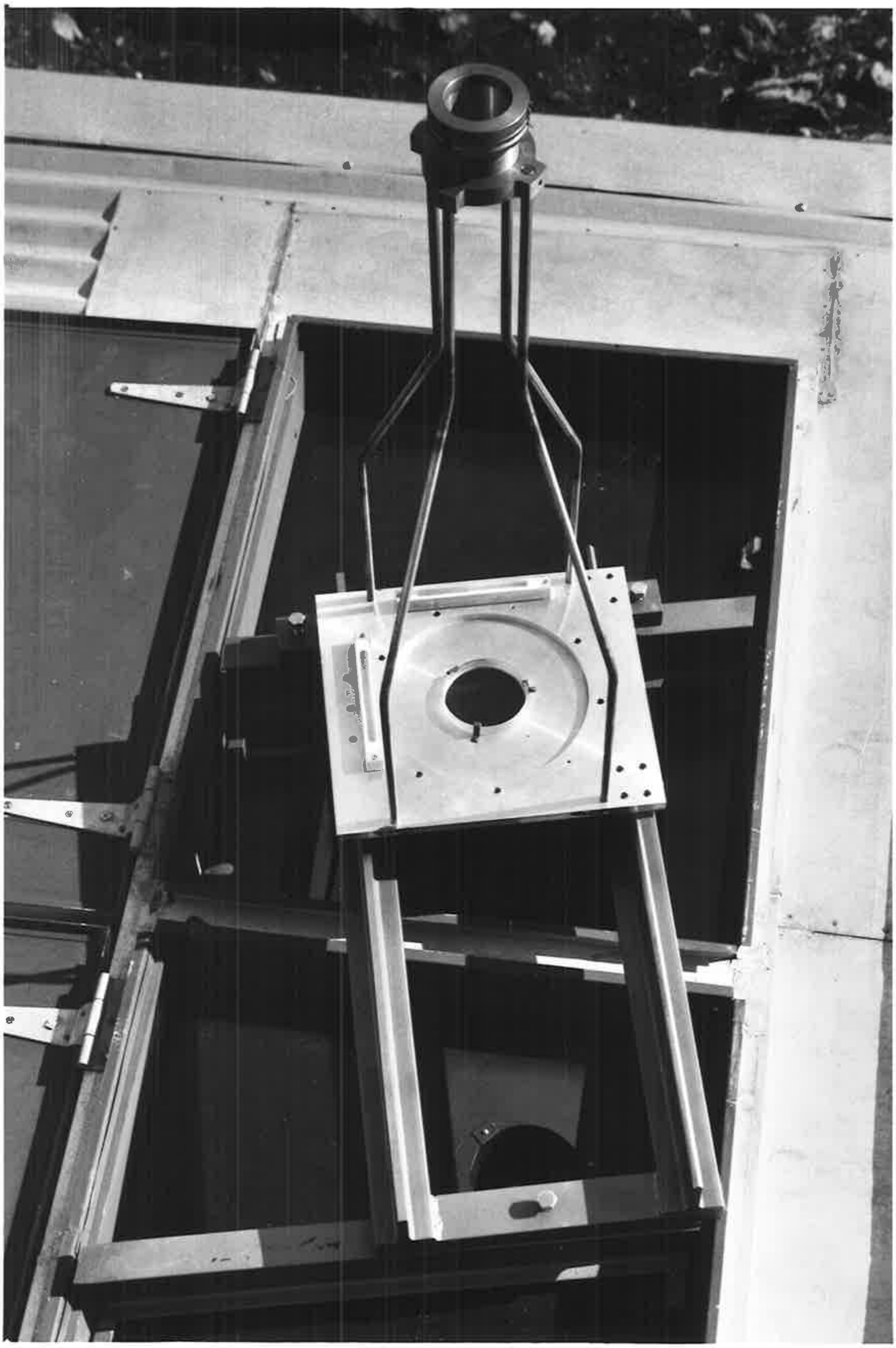

FIGURE 2.6 Receiver and transmitter collimation procedure.

2.2.2 Electronic Recording System

Depending on the height range to be studied, one of two signal recording techniques is used. The signal from altitudes below 10 km is of sufficient magnitude to enable an analogue recording technique to be used. For altitudes above about 10 km, however, the signal is so weak that individual current pulses are resolved, corresponding to the arrival of discrete photons. In this case a digital recording technique is employed.

2.2.2.1 Digital Recording System

A block diagram of the recording systems is shown in Figure 2.3. Single photon pulses from the photomultiplier are amplified by a factor of 10 by a preamplifier mounted on the photomultiplier housing, and passed through 50 Ω cable to the electronics rack. The pulses are further amplified by a factor of 10, and then pass to a high speed discriminator whose threshold is adjusted to eliminate noise pulses due to the main power supply and triggering circuits.

The standardised output pulses from the discriminator are amplified and further shaped by the scaler driver, and passed to a 10-channel counter which has been specifically developed for the laser radar. With the exception of the power supplies, the circuitry is based almost entirely on integrated circuits. The counter channels form

10 successive range recording intervals, and may be set at 1,2,4 or 8 km width. The delay between the arrival of a trigger pulse and the opening of the first channel is adjustable, and at present may be set at 8, 12, 20 or 40 km. The dead time between channels is less than 1% of the width of the smallest channel. With such a combination of delays and widths, it is possible to investigate the 8 to 120 km height range. The maximum counting rate varies from one channel to another, being dependent on the speed of the individual components of each channel. The maximum counting rate of each channel for regularly spaced pulses, however, is not less than 20 MHz, and it is the speed of the discriminator, set at 20 MHz, that determines the counting rate of the total system.

The pulse counting system was found to be linear up to average random count rates of 0.2 - 0.3 MHz. At greater count rates the effect of more than one pulse arriving during the resolving time of the counter becomes significant, and the observed count rate n is less than the true count rate N. If t is the resolving time of the counter, then nt is the total "dead time" of the counter per second, and the ratio of true counts to observed counts is given by the equation

$$\frac{N}{n} = \frac{1}{1 - nt} \qquad (2.1)$$

Figure 2.7 shows a graph of the departure from linearity of the counting system as a function of count rate. The circles are the results of an experimental determination, and the solid curves are derived using equation (2.1) with t = 50 and 55 nsec respectively. It is thus possible, within limits, to count pulses at rates greater than 0.2 MHz and apply corrections according to equation (2.1). This will be discussed in further detail in a later chapter.

The counter is arranged to accumulate the counts recorded in consecutive firings of the laser for the appropriate height range. The counts in each channel are stored until erased by an external control, or they can be read out in turn by a manual operation. The number of laser firings is also recorded.

The scattered light from altitudes below about 20 km is attenuated to reduce the maximum count rate to a level acceptable to the counting system. Thus low level observations are limited by the performance of the counter system, whereas above 20 km, the limitation lies in the weak signal strength.

2.2.2.2 Analogue Recording System

The advantage of the analogue recording system is that a complete profile from nearly ground level to about 10 km can be obtained with approximately 5 laser firings. The

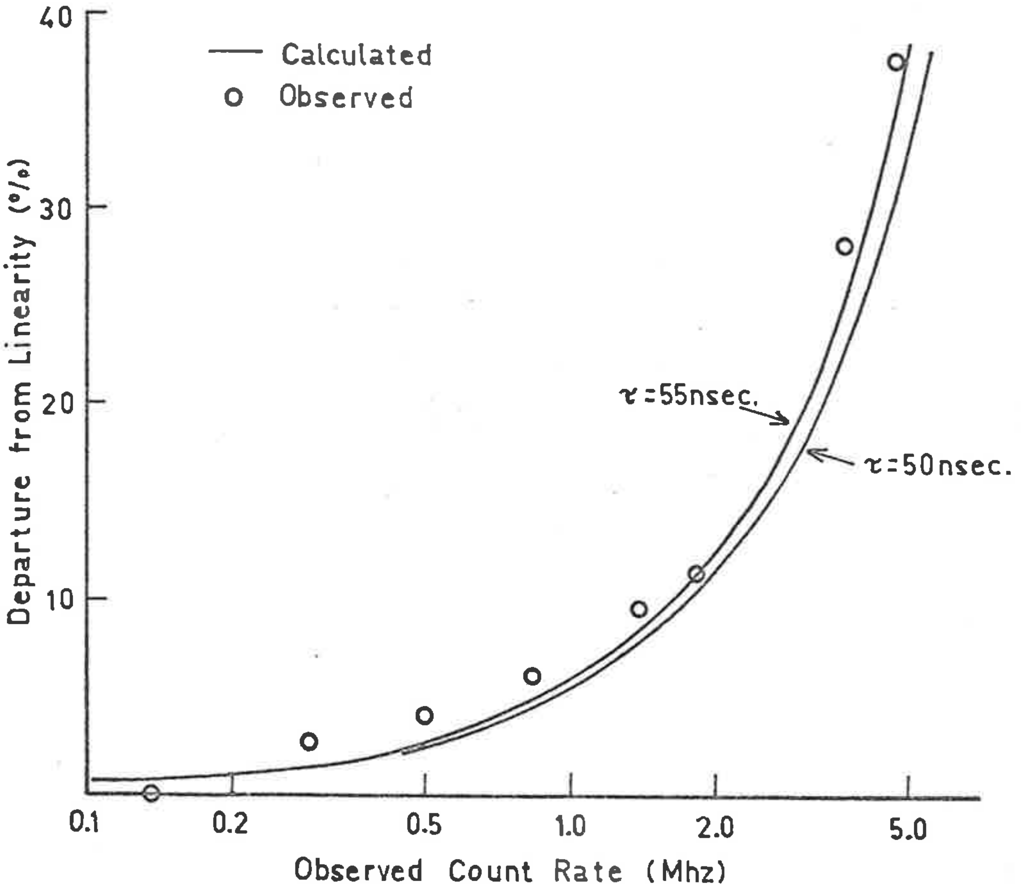

FIGURE 2.7 Departure from linearity of the counting system.

current waveform from the photomultiplier is displayed directly on the screen of a Tektronix 564 storage oscilloscope in the conventional A-scan mode. It is thus possible, particularly in low altitude regions where turbid layers exist, to observe transient atmospheric phenomena in real time.

As the signal between 0.4 and 10 km varies by more than 3 orders of magnitude, a logarithmic amplifier would be desirable. However, such an amplifier having a sufficiently fast speed of response was not available commercially, and attempts to develop one were unsuccessful. The signal recording is at present carried out by overlapping the results of several soundings at progressively higher sensitivity settings of the oscilloscope vertical amplifier. The oscilloscope display of each laser firing is photographed and the profile is digitised for data processing.

Due to jitter in rotation of the Q-switch and the finite opening time of the receiver shutter, discussed previously in Section 2.2.1, it is not possible to use the rotating shutter in the receiver to cut off the high intensity light scattered from the lowest regions of the atmosphere. Thus, as the gain of the oscilloscope is increased, the amplifier becomes severely overloaded. However, experiments show that the amplifier recovers sufficiently rapidly to allow this technique to be used.

A neutral filter is placed in the received cone of light to ensure that the maximum light intensity incident on the photomultiplier does not overload the photocathode.

2.2.3 Electrical Noise Problems

Initial experiments using the pulse counting technique revealed the presence of considerable noise interference. The majority of the noise appeared to come from the relays in the main power supply, and was picked up by the circuits associated with the photomultiplier.

The photomultiplier and pre-amplifier were subsequently shielded magnetically, and leads to and from the main power supply were electrostatically shielded. The pre-amplifier and Peltier battery power supplies were separately decoupled. Earth loops were minimised by the judicial positioning of earth points. A large proportion of the noise interference has subsequently been eliminated, and the discriminator is capable of reducing the remaining interference to negligible proportions.

CHAPTER THREE

THEORETICAL SCATTERING CONSIDERATIONS

Theoretical aspects of importance to laser radar studies of the atmosphere are discussed in this chapter. The solution of the basic lidar equation is not straightforward, as the interpretation of the results using a single wavelength and scattering angle is subject to considerable uncertainty. However, making certain reasonable assumptions concerning the nature of the scatterers in the atmosphere, it is possible to deduce quantitative information such as scattering coefficients, turbidities and number densities.

3.1 The Lidar Equation

The photon count C(h) received from a small height interval Δh at height h is a function of the Rayleigh backscattering coefficient $B_R(\pi,h)$ (metre^{-1} sterad^{-1}) for the molecular component, and the backscattering coefficient $B_A(\pi,h)$ for the aerosol component. For the case of vertical lidar soundings, it can be shown that

$$C(h) = k\{T(0 - h)\}^2 \frac{B_R(\pi,h) + B_A(\pi,h)}{h^2} \qquad (3.1)$$

where T(0 - h) is the transmission through the atmosphere between ground level and the height h. The value of the constant k depends on equipment parameters such as laser output energy, transmission of all optical surfaces, and efficiency of the photomultiplier photocathode.

The transmission term in equation 3.1 is related to the volume attenuation coefficient, a(h) (metre^{-1}), by the following expression:

$$T(0 - h) = \exp \left\{- \int_0^h a(h')dh'\right\} \qquad (3.2)$$

Both the total backscattering coefficient, given by

$$B(\pi,h) = B_R(\pi,h) + B_A(\pi,h) \qquad (3.3)$$

and the attenuation coefficient are functions of the type, number concentration and size distribution of atmospheric particles. However, a(h) appears in equation 3.1 as an integral expression, and hence fluctuations in the received signal C(h) may be attributed primarily to changes in $B(\pi,h)$. The lidar signal scattered from an atmosphere of low turbidity is thus capable of directly revealing layers and inhomogeneities. The signal scattered from a turbid atmosphere is more difficult to interpret because of the interrelation between backscattering and attenuation.

In the visible region of the spectrum, the attenuation coefficient appearing in equation 3.2 is mainly dependent on the molecular and aerosol scattering coefficients, $\beta_R(h)$ and $\beta_A(h)$ respectively, and on the ozone absorption coefficient $\beta_o(h)$. Absorption of ruby laser radiation by water vapour, aerosols and the molecular atmosphere is considered negligible. The attenuation coefficient is thus approximated by the following expression:

$$a(h) = \beta_R(h) + \beta_A(h) + \beta_o(h) \ . \qquad (3.4)$$

3.2 Solution of the Lidar Equation

As several of the quantities appearing in the equipment parameter k in equation 3.1 are difficult to measure, and may change with time, a relative method of solution is employed in the present work. The method is similar to that of Elterman (1966), who used an iterative-convergent technique to solve the equation describing scattering from a searchlight beam. A brief description follows.

In order to solve equation 3.1, it is assumed that at some calibration height, hcal, the scattering is predominantly molecular, so that the aerosol backscattering coefficient $B_A(\pi,\mathrm{hcal})$ can be ignored. The product $k\{T(0 - h)\}^2$ in equation 3.1 can then be calculated.

It is convenient to rewrite $T(0 - h)$ in terms of the transmission between ground level and the calibration height, $T(0 - \mathrm{hcal})$, and the transmission $T(\mathrm{hcal} - h)$ between the calibration height and height h. Equation 3.1 becomes

$$C(h) = k\{T(0 - \mathrm{hcal})\}^2\{T(\mathrm{hcal} - h)\}^2 \frac{B_R(\pi,h) + B_A(\pi,h)}{h^2} \qquad (3.5)$$

if $h > \mathrm{hcal}$ (if $h < \mathrm{hcal}$, the term $\{T(\mathrm{hcal} - h)\}^2$ in the above equation appears in the denominator).

The transmission term $T(0 - \mathrm{hcal})$ is assumed constant for a given experiment. Equation 3.5 is solved by rewriting $T(\mathrm{hcal} - h)$ in terms of the attenuation coefficient as in equation 3.2, and expressing the backscattering coefficients $B_A(\pi,h)$ and $B_R(\pi,h)$ in terms of the volume scattering coefficients by means of the following equation:

$$B_A(\pi,h) + B_R(\pi,h) = (P_A(\pi)\beta_A(h) + P_R(\pi)\beta_R(h))/4\pi \qquad (3.6)$$

$P_A(\pi)$ and $P_R(\pi)$ are, respectively, the normalised backscattering phase functions for aerosols and the molecular atmosphere. Representing all the constant terms by k´, equation 3.5 is then given by

$$C(h) = k' \exp\left\{-2\int_{hcal}^{h} (\beta_R(h') + \beta_A(h') + \beta_o(h'))dh'\right\} \frac{(P_R(\pi)\beta_R(h) + P_A(\pi)\beta_A(h))}{h^2} \qquad (3.7)$$

which can be solved for $\beta_A(h)$ by an iterative technique (Elterman, 1966).

However, the laser radar equation can be solved with a high degree of accuracy without the necessity for an iterative method, as the following considerations illustrate. If the numerical integration in equation 3.7 is computed using sufficiently small height intervals, then $\beta_A(h)$ appearing in the transmission correction term

$$\exp\left\{-2\int_{hcal}^{h} (\beta_R(h') + \beta_A(h') + \beta_o(h'))dh'\right\}$$

can be ignored without introducing serious errors, Substitution of the transmission correction term in equation 3.5 enables $B_A(\pi,h)$ to be calculated.

Results can now be expressed in terms of the scattering index I(h), defined by the equation

$$I(h) = C(h)h^2/\{T(hcal - h)\}^2 \;. \qquad (3.8)$$

The scattering index is thus directly proportional to the total backscattering coefficient $B(\pi,h)$. The experimental values of scattering index are normalised to theoretical values for a molecular atmosphere at height hcal, and departures of the experimental from the theoretical curve are interpreted as indicating the presence of aerosols.

3.3 Quantities Derived from the Lidar Data

The ratio $R(h)$ of experimental values of scattering index to molecular values is given by the identity

$$R(h) = 1 + B_A(\pi,h)/B_R(\pi,h) \quad . \qquad (3.9)$$

The aerosol backscattering coefficient $B_A(\pi,h)$ can be deduced by inserting in this equation a value of the molecular backscattering coefficient $B_R(\pi,h)$. The latter is calculated using the following relation:

$$B_R(\pi,h) = (3/8\pi)\beta_R(h) \qquad (3.10)$$

where the volume scattering coefficient $\beta_R(h)$ is given by the formula

$$\beta_R(h) = \sigma_R(\lambda)N_R(h) \qquad (3.11)$$

$\sigma_R(\lambda)$ is the Rayleigh scattering cross-section for radiation of wavelength λ, and at the ruby laser wavelength of 6943 Å, $\sigma_R(\lambda) = 1.760 \times 10^{-27}$ cm^2. $N_R(h)$ is the molecular number density.

Combining equations 3.6 and 3.9, the following relation is obtained:

$$\frac{\beta_A(h)}{\beta_R(h)} = \frac{P_R(\pi)}{P_A(\pi)}\{R(h) - 1\} \quad . \qquad (3.12)$$

The quantity on the left hand side of the above equation is known as the turbidity, $\tau(h)$, and substituting the value of $\beta_R(h)$ by means of equation 3.11 enables $\beta_A(h)$ to be calculated. The molecular phase function $P_R(\pi) = 1.5$, and the value of $P_A(\pi)$ is obtained from independent experimental observations and theory.

The aerosol number density $N_A(h)$ is related to the backscattering coefficient $B_A(\pi,h)$ by the following expression:

$$B_A(\pi,h) = N_A(h)\ \overline{\Sigma_A(\pi)} \tag{3.13}$$

where $\overline{\Sigma_A(\pi)}$ is the backscattering function for aerosols averaged with respect to the size distribution.

The magnitudes of the aerosol phase function for backscatter, $P_A(\pi)$, and the backscattering function, $\overline{\Sigma_A(\pi)}$, are subject to considerable uncertainty. For example, $P_A(\pi)$ in Figure 3.1 is shown as a highly variable function of the particle size parameter x, the circumference to wavelength ratio. $P_A(\pi)$ was derived theoretically for single spherical particles of refractive index 1.33. It can be seen that $P_A(\pi)$ shows no simple dependence on particle size or wavelength. Natural aerosols in the atmosphere, however, have a range of sizes, and fluctuations in the phase function tend to average out. Thus, a given value of $P_A(\pi)$ implies a given type of aerosol and constant size distribution. Deirmendjian (1965) has noted that on the basis of lidar observations alone, several equally plausible interpretations of the observed value of $B_A(\pi,h)$ are possible. A change in aerosol number

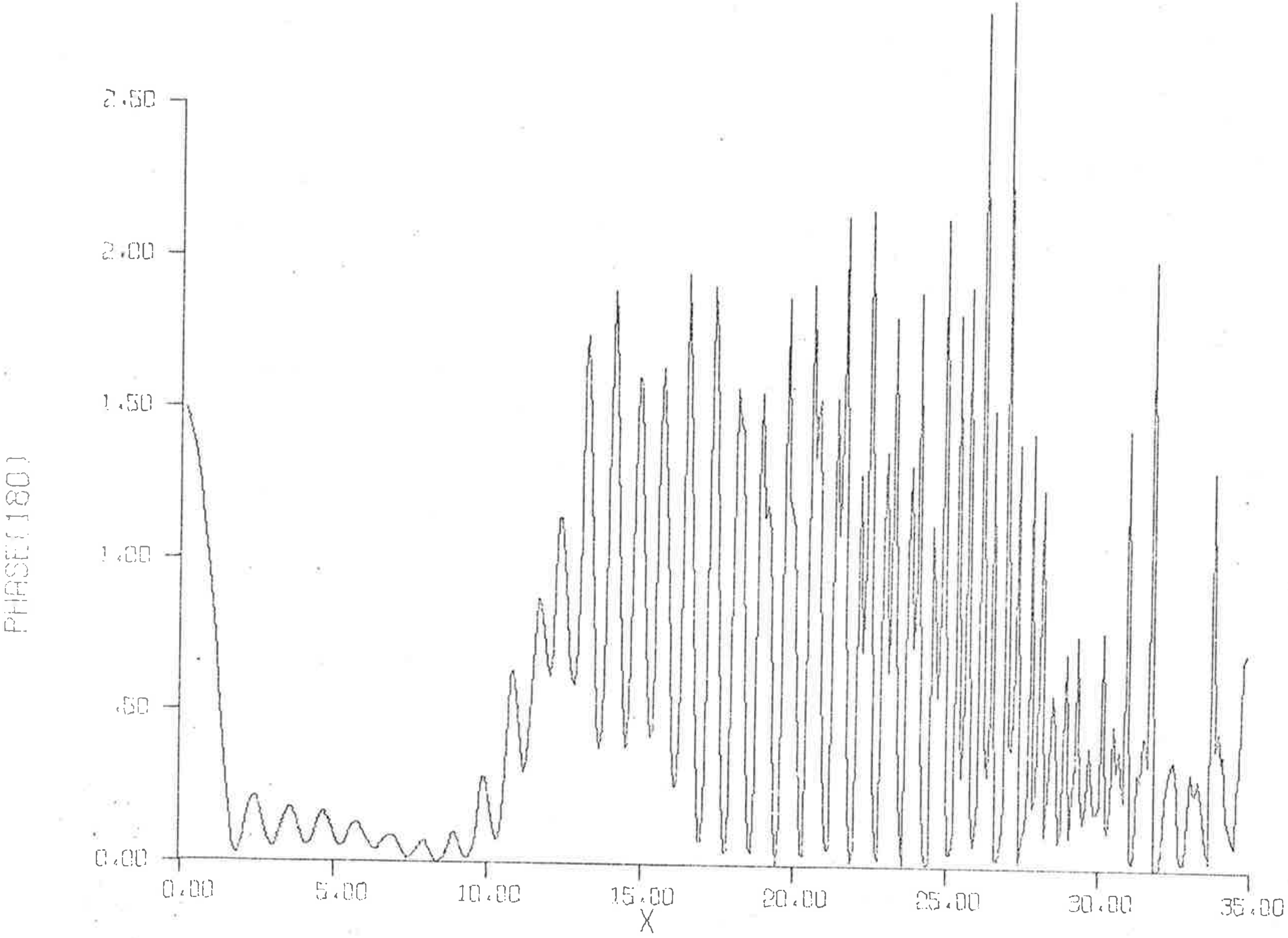

FIGURE 3.1 Phase function for backscatter as a function of particle size parameter x. Refractive index 1.33 .

density would alter $B_A(\pi,h)$, other parameters being constant. Alternatively the total aerosol number density could remain constant, but the aerosol refractive index might change due to some chemical reaction. Coagulation and sedimentation could alter the size distribution of a given ensemble of particles, which would be reflected in a change in $B_A(\pi,h)$ and also $P_A(\pi)$.

The above discussion clearly demonstrates the limitations of the present technique in interpreting the measured value of $B_A(\pi,h)$. However, as little is known of aerosol concentrations, results of these calculations are therefore of great interest.

In the following sections, aspects in the derivation of $P_A(\pi)$ and $\overline{\Sigma_A(\pi)}$ will be discussed.

3.4 Mie Scattering Theory

In 1908 Mie formulated a complete solution to Maxwell's equations describing the scattering of radiation by a single homogeneous sphere. Although natural aerosols can hardly be described as homogeneous spheres, many useful theoretical studies of optical scattering properties of atmospheric aerosols have been carried out in recent years.

For radiation of wavelength λ, the cross-section for scattering, σ_A(metre^2), by a single sphere of radius r is given by the formula (Van de Hulst, 1957):

$$\sigma_A(r) = (\lambda^2/2\pi)\sum_{n=1}^{\infty}(2n+1)\{|a_n|^2 + |b_n|^2\} \qquad (3.14)$$

where the Mie coefficients a_n and b_n are written in terms of Ricatti-Bessel functions:

$$a_n = (\psi_n'(y)\psi_n(x) - m\psi_n(y)\psi_n'(x))/(\psi_n'(y)\zeta_n(x) - m\psi_n(y)\zeta_n'(x)) \quad (3.15)$$

$$b_n = (m\psi_n'(y)\psi_n(x) - \psi_n(y)\psi_n'(x))/(m\psi_n'(y)\zeta_n(x) - \psi_n(y)\zeta_n'(x)) \quad (3.16)$$

The arguments are $x = 2\pi r/\lambda$ and $y = mx$, where r is the radius of the sphere and m the complex refractive index, compared with that of the surrounding medium. The Ricatti-Bessel functions $\psi_n(z)$ and $\zeta_n(z)$ are defined in terms of the spherical Bessel functions $j_n(z)$ and $h_n^{(2)}(z)$.

$$\psi_n(z) = zj_n(z) \quad (3.17)$$

$$\zeta_n(z) = zh_n^{(2)}(z) \quad (3.18)$$

The primes in equations 3.15 and 3.16 denote the derivatives of the functions.

The backscattering function $\Sigma_A(\pi)$ is written in terms of Mie's amplitude function $S_1(\pi)$:

$$\Sigma_A(\pi,r) = \lambda^2|S_1(\pi)|^2/4\pi^2 \quad (3.19)$$

where

$$S_1(\pi) = -\sum_{n=1}^{\infty}(n + \tfrac{1}{2})(-1)^n(a_n - b_n) \quad (3.20)$$

The normalised phase function for backscattering, $P_A(\pi,r)$, is then given by the relation

$$P_A(\pi,r) = 4\pi\,\Sigma_A(\pi)/\sigma_A(r) \quad (3.21)$$

Calculations of the Mie coefficients a_n and b_n are simplified using recurrence relations described by Aden (1952), whereby the expressions in equations 3.15 and 3.16 are rewritten in terms of the logarithmic derivative functions;

$$D_n(y) = [\ln \psi_n(y)]' \qquad (3.22)$$

$$G_n(x) = [\ln \zeta_n(x)]' \qquad (3.23)$$

Then equations for the Mie coefficients may be expressed after some manipulation in the following form:

$$a_n = j_n(x)\ [D_n(y) - mD_n(x)]/h_n^{(2)}(x)\ [D_n(y) - mG_n(x)] \qquad (3.24)$$

$$b_n = j_n(x)\ [mD_n(y) - D_n(x)]/h_n^{(2)}(x)\ [mD_n(y) - G_n(x)] \qquad (3.25)$$

The logarithmic derivative D_n satisfies the recurrence relation

$$D_{n-1}(z) = \frac{n}{z} - \left[D_n(z) + \frac{n}{z}\right]^{-1} \qquad (3.26)$$

and an identical relation holds for G_n.

Most workers have used the above relationship to calculate D_n by an upward recurrence relation (e.g. Aden, 1952). However, Kattawar and Plass (1967) have reported that the upward recurrence relation becomes numerically unstable when $n > |z|$, a region of particular importance for large values of x. They have shown that the downward recurrence formula for D_n is always numerically stable. Nevertheless, the author has found that calculations relevant to the work described here can be accurately performed on a CDC 6400 computer (60 bits per word) using the upward recursion method. Results up to x = 40 are in agreement with values tabulated by Deirmendjian (1963).

Using the Mie theory described above, $P_A(\pi,r)$ was calculated for a single sphere of refractive index 1.33, and for a range of values of the size parameter x varying from 0.1 to 35 in steps of 0.1. Figure 3.1 shows the highly oscillatory nature of the curve. For small values of x, $P_A(\pi,r)$ approaches 1.5, the molecular phase function for backscatter.

Mie's theory describing scattering from a single sphere has since been extended to cover the case of a sphere surrounded by a concentric spherical shell of different refractive index (Aden & Kerker, 1951). It is well established that the scattering properties of atmospheric aerosols are dependent on the relative humidity, and the above theory has obvious applications. Witt (1968) has used scattering theory for a concentric spherical shell to describe optical properties of noctilucent clouds, under the assumption that the particles consist of nuclei surrounded by a shell of ice.

3.5 Some Computational Results Using Mie's Theory

Several aspects of the nature of aerosols in the atmosphere have been discussed in Chapter 1. The wide variety of aerosol types and shapes in the atmosphere limits the usefulness of Mie scattering theory. Nevertheless, these calculations can be invaluable to an understanding of many optical properties of natural aerosols.

Attempts have been made to investigate the validity of the use of Mie's theory to predict the scattering from randomly aligned, irregularly shaped, polydisperse particles as existing in the atmosphere. One approach (e.g., Greenberg et al, 1961; Napper and Ottewill, 1963) is to measure scattering from single, non-spherical particles of known size and shape, and compare the results with calculations for spheres. The size of the non-spherical particle is usually based on some combination of geometrical parameters such as volume and largest dimension. The results of these comparisons show that it is impossible to predict the scattering characteristics of non-spheres on the basis of a linear relationship between their corresponding geometrical properties.

The method adopted by Powell et al (1967) was to measure the scattering from ensembles containing randomly oriented, polydisperse particles. The results were compared with Mie calculations for spheres on the basis that irregularities in the scattering properties for the ensemble of polydisperse, irregularly shaped particles would tend to average out, and that a certain ensemble of spheres with a given size distribution would exhibit the same characteristics. The equivalent size distribution of the irregularly shaped particles is deduced by taking the largest projected dimension as being characteristic of the particle. Powell et al (1967) measured the intensity and polarisation of light scattered by ensembles of magnesium oxide cubes and zinc oxide "fourlings", and found that polydisperse cubes scatter exactly like spheres. On the other hand, they found it difficult to predict consistently the scattering characteristics of ensembles containing particles with small volume-to-longest dimension ratios such as the fourlings.

Many of the stratospheric particles collected by Junge and Manson (1961) and Mossop (1965), and a large proportion of the tropospheric aerosols (Heard and Wiffen, 1969) appear to be moist spheroids. Many others would at least fall into the cube category discussed above. The volatile stratospheric aerosols detected by Rosen (1969(a)) would very likely be spherical in shape. It is therefore reasonable to expect that the Mie theory is capable of predicting optical scattering properties of the natural aerosol.

The averaged aerosol backscattering function $\overline{\Sigma_A(\pi)}$ is found by integration of $\Sigma_A(\pi,r)$ over the range of particle sizes. If $dN(r)$ is the number of particles having radii between r and $r + dr$, then

$$\overline{\Sigma_A(\pi)} = \int_{r_1}^{r_2} \Sigma_A(\pi,r)dN(r) / \int_{r_1}^{r_2} dN(r) \qquad (3.27)$$

where r_1 and r_2 are the limits of particle sizes. A similar expression holds for the averaged total scattering cross-section $\bar{\sigma}_A$. $\overline{P_A(\pi)}$, the normalised phase function averaged with respect to the size distribution, is then calculated using an expression similar to equation 3.21 thus;

$$\overline{P_A(\pi)} = 4\pi\overline{\Sigma_A(\pi)}/\overline{\sigma_A(r)} \qquad (3.28)$$

Table 3.1 lists results of calculations of $\overline{\Sigma_A(\pi)}$ and $\overline{P_A(\pi)}$ for several size distributions and refractive indices approximating, as nearly as possible, measured aerosol characteristics. The wavelength of the incident radiation is 0.6943 microns. The refractive index value of 1.33 corresponds to that of pure water droplets, and 1.50 approximates the refractive index of ammonium sulphate and sodium chloride aerosols. As the hygroscopic particles take up water with increasing relative humidity, the observed refractive index will vary between the two limits. The value of the exponent ν of the Junge distribution varies from 2 to 4. The lognormal size distribution is described by equation 1.4 with a standard deviation of 0.3 (using natural logarithms) and a mean radius of 0.35 μ (Dave and Mateer, 1968). Rosen's exponential size distribution is defined in equation 1.5. The upper limit of particle radii has been arbitrarily set at 3.0 microns. Although aerosols having radii greater than 3.0 microns are known to exist, their effect on the averaged backscattering cross-section and averaged phase function are very small for the size distributions assumed here. Increasing the upper radius limit of the Junge distribution to 10 microns, for example, increases the backscattering cross-section by 1% to 10%, depending on the value of ν. The backscattering cross-section for an ensemble of spheres having the lognormal or exponential size distribution is hardly affected if either the upper or the lower radius limits are extended. For example, an extension of the integration range of the lognormal distribution to limits of 0.01 and 8.0 microns only increases $\overline{\Sigma_A(\pi)}$ by approximately 0.03%.

TABLE 3.1

Refractive Index	Size Distribution	Radius Limits (Microns)	$\bar{\sigma}_A$ (m^2)	$\overline{\Sigma_A(\pi)}$ (m^2 sterad^{-1})	$\overline{P_A(\pi)}$ normalised
1.33	Junge $\nu = 2$	.04 - 3.0	6.74×10^{-14}	1.82×10^{-15}	0.339
	$\nu = 3$		6.56×10^{-15}	1.22×10^{-16}	0.234
	$\nu = 4$		9.73×10^{-16}	2.47×10^{-17}	0.319
	lognormal		1.17×10^{-12}	1.02×10^{-14}	0.110
1.40	Junge $\nu = 2$	.04 - 3.0	7.22×10^{-14}	2.36×10^{-15}	0.410
	$\nu = 3$		7.87×10^{-15}	1.82×10^{-16}	0.290
	$\nu = 4$		1.30×10^{-15}	3.69×10^{-17}	0.356
	lognormal		1.43×10^{-12}	1.81×10^{-14}	0.159
	Junge $\nu = 2$	.08 - 3.0	2.88×10^{-13}	9.38×10^{-15}	0.409
	$\nu = 3$		6.22×10^{-14}	1.38×10^{-15}	0.278
	$\nu = 4$		1.96×10^{-14}	4.60×10^{-16}	0.295
	$\nu = 3$	.01 - 3.0	1.23×10^{-16}	2.86×10^{-18}	0.291
	Rosen's exponential	"	1.12×10^{-12}	2.61×10^{-14}	0.294
1.50	Junge $\nu = 2$	.04 - 3.0	7.79×10^{-14}	4.40×10^{-15}	0.709
	$\nu = 3$		9.64×10^{-15}	3.68×10^{-16}	0.478
	$\nu = 4$		1.81×10^{-15}	6.31×10^{-17}	0.440
	lognormal		1.63×10^{-12}	4.21×10^{-14}	0.324
	Junge $\nu = 4$	.30 - 3.0	1.92×10^{-12}	6.35×10^{-14}	0.415

On the other hand, an extension of the lower radius limit of the Junge distribution can have a significant effect on the backscattering cross-section. The effect of altering the lower cut-off limit from 0.04 to 0.01 microns is shown in the 1.40 refractive index group of Table 3.1. The averaged backscattering cross-section is decreased by more than an order of magnitude. The importance of this result may be judged by the fact that up to the present time, little is known of the characteristics of the size distribution in this particular size region. This is because the size region is at the limits of sensitivity of the two types of instrument used to detect aerosols; the cloud chamber and the impactor. The reason for the importance of the very small particles in Junge type distributions is clearly demonstrated in Figure 3.2, which shows the backscattering cross-section of a spherical particle of refractive index 1.33 as a function of its radius, computed on the basis of Mie's theory described in the previous section. Relative values of a Junge type size distribution with exponent $\nu=3$, which approximates the size distribution of tropospheric aerosols, are also included. It can be seen that although a given particle becomes "optically inefficient" as its size parameter x is made smaller than about 3, tropospheric aerosols of small size are significant because of their overwhelming numbers. On the other hand, later considerations show that the concentration of Aitken nuclei relative to the large particles is very much less in the stratosphere than in the troposphere. Consequently, the optical effects of stratospheric Aitken nuclei may be neglected.

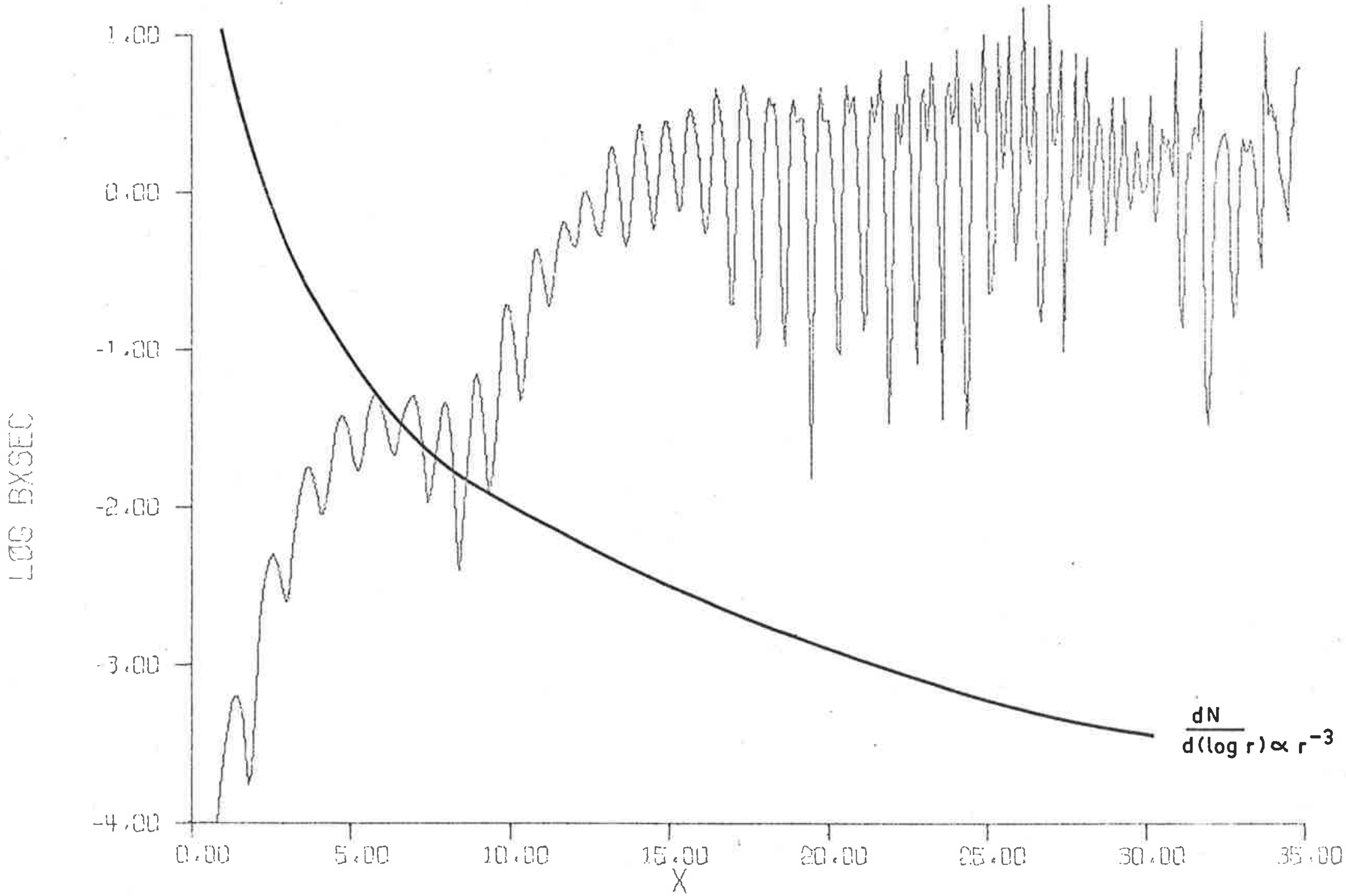

FIGURE 3.2 Backscattering coefficient and Junge size distribution as functions of particle size parameter, x.

The effect of coagulation of the smaller aerosols has already been discussed in Chapter 1. It has been shown that the lower cut-off radius could vary from less than 0.01 micron to about 0.08 microns, depending on how far removed the region considered is from the source of Aitken nuclei. It is apparent that significant fluctuations could be observed in the backscattering cross-section due to effects of the lower cut-off radius.

The phase function for backscatter appears to be more stable to changes in the upper and lower radius limits of the size distribution. In the instance of changing the lower limit from .04 to .01 microns discussed above, the backscattering phase function changes by less than 1%.

Other interesting features of the phase function for backscatter are demonstrated in Figure 3.3, which shows the variation of $\overline{P_A(\pi)}$ with the exponent ν of the Junge distribution and for three different values of refractive index. For comparison, the result of a calculation by Deirmendjian (1965), and measurements of phase functions by Reeger and Siedentopf (1946), and Barteneva (1960), are included. The latter values were originally in the form of the phase function for the actual atmosphere consisting of aerosols and the molecular component. The aerosol component of the phase function $P_A(\pi)$ was separated from the overall phase function $P(\pi)$ by using the following relation (Deirmendjian, 1965).

$$P(\pi) = \frac{\beta_R P_R(\pi) + \beta_M P_M(\pi)}{\beta_R + \beta_M} \quad . \qquad (3.29)$$

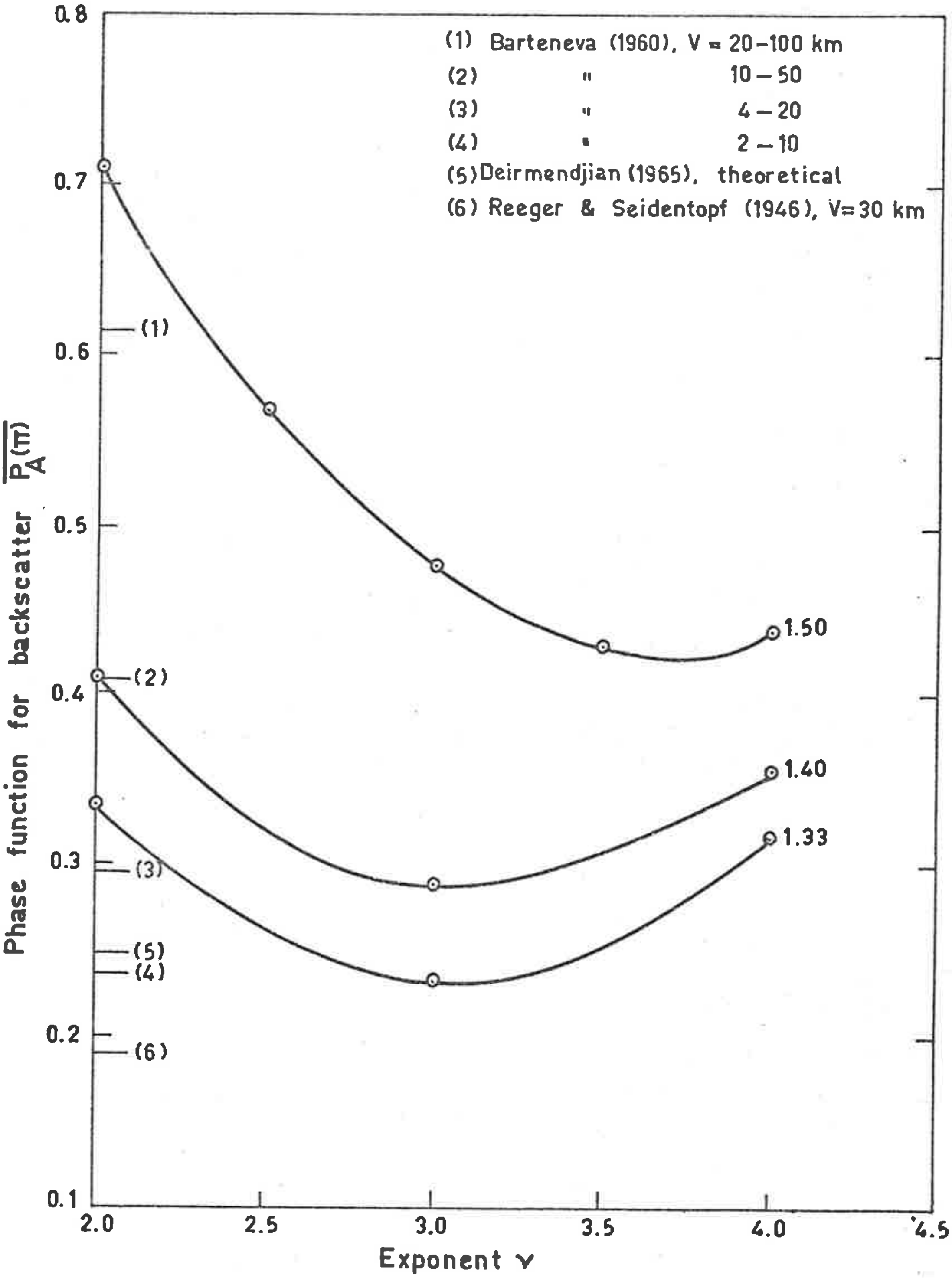

FIGURE 3.3 Variation of the phase function for backscatter averaged over a Junge size distribution with exponent ν and cut-off radii of .04 and 3μ. Refractive indices as marked.

The value for β_R at ground level was taken from Elterman's (1968) tables, for a wavelength of 0.55 microns.

It is apparent from Figure 3.3 that water plays a significant role in affecting the optical characteristics of atmospheric aerosols, at least in the lower atmosphere where measurements have been taken. More than half the experimental values of $\overline{P_A(\pi)}$ are less than 0.3, and centred about the values for pure water. There appears to be a definite relationship between Barteneva's phase functions for backscatter and the meteorological visual range V (km), defined as the limiting horizontal distance for which the contrast of a black object becomes equal to 0.02. It can be shown (Middleton, 1958) that provided the atmosphere is horizontally homogeneous,

$$V = 3.912/\beta \tag{3.30}$$

implying that the phase functions for backscatter measured by Barteneva (1960) are dependent on the value of the total scattering coefficient β.

It is also obvious from a comparison of Barteneva's (1960) experimental results and the theoretical values of $\overline{P_A(\pi)}$ presented in Figure 3.3 that as the visibility V decreases, the value of the backscattering phase function decreases towards the value for pure water. Barteneva (1960) found that the form of the scattering function depends, to a certain extent, on the relative humidity. Junge (1963) has shown theoretically how hygroscopic particles grow with increasing relative humidity. Garland (1969) has computed a theoretical relationship between β and relative humidity, and Horvath and Noll (1969) have detected such an effect in experimental observations. The results in Figure 3.3 also indicate that exceptionally high visibilities ($\sim$ 100 km) are attained only when the atmosphere is relatively dry.

In Figure 3.4, the tabulated values of $\overline{\Sigma_A(\pi)}$ for the Junge size distribution are shown as functions of the refractive index and exponent ν. In general, a decrease in refractive index leads to a decrease in $\overline{\Sigma_A(\pi)}$. A reduction in the value of refractive index from that of a solid to that of pure water decreases the averaged backscattering cross-section by a factor of about 2. A decrease in the exponent by a numerical value of one leads to about an order of magnitude increase in the averaged backscattering cross-section. This result has obvious implications. Near the coast as at Adelaide, South Australia, a change in the direction of the wind can lead to a change in the source of aerosols, from continental ($\nu \simeq 3$) on the one hand to maritime ($\nu \simeq 2$) on the other.

In order to gain a further insight into the nature of the aerosol size distribution in the stratosphere, calculations were made of the scattering coefficient, based on Mie cross-sections $\bar{\sigma}_A$ and measured number densities. As moisture appears to be a major component of the stratospheric aerosol, $\bar{\sigma}_A$ values calculated on the basis of a refractive index of 1.40 are used. The theoretical values of the aerosol scattering coefficient β_A were calculated according to the relation

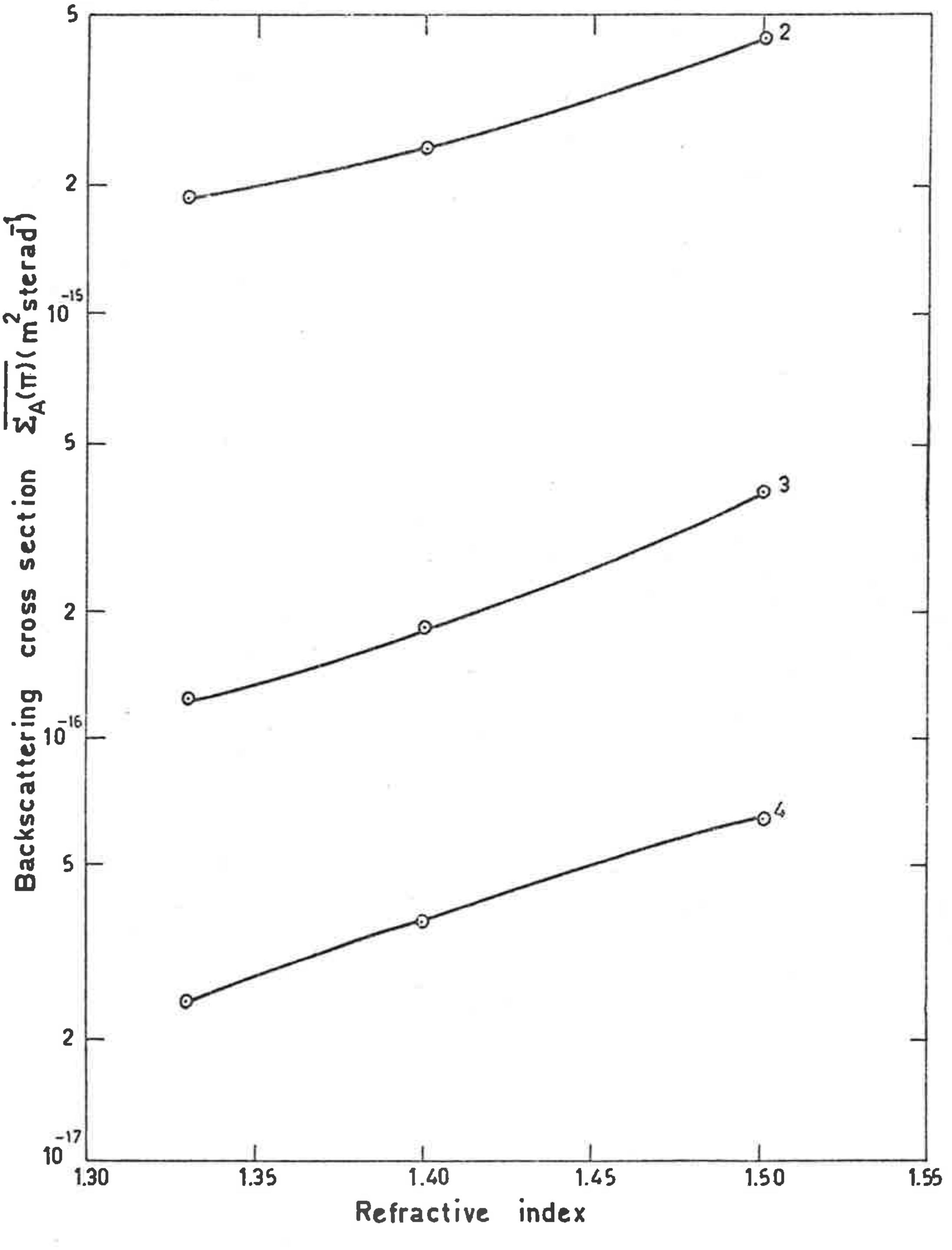

FIGURE 3.4 Averaged backscattering cross-section as a function of refractive index for various exponents of the Junge size distribution. The cut-off radii are .04 and 3μ.

$$\beta_A = N\bar{\sigma}_A . \qquad (3.31)$$

The results of the calculations are shown in Figure 3.5. Each curve corresponds to a given size distribution model assumed in the calculations, and can be identified in Table 3.2.

TABLE 3.2

Curve	Size Distribution Model
1	Junge power law, $\nu = 4$, $r_1 = .04\ \mu$
2	" " " , $\nu = 3$, "
3	" " " , $\nu = 2$, " & " " " , $\nu = 3$, $r_1 = .08\ \mu$
4	" " " , $\nu = 2.5$, $r_1 = 0.1\ \mu$
5	" " " , $\nu = 2$, $r_1 = .08\ \mu$
6	Exponential (Rosen, 1969(a)) & lognormal (Dave & Mateer, 1968)
7	Junge power law, $\nu = 0.5$, $r_1 = 0.1\ \mu$

On the vertical axis of Figure 3.5 are the results of several optical measurements of the peak aerosol scattering coefficient in the stratosphere, and on the horizontal axis, peak aerosol number densities in the stratosphere measured by various workers are included. In the following discussion, a particular size distribution is chosen so that the scattering coefficient and number density measurements are compatible with the theoretical relationship in equation 3.31.

In earlier sections it has been noted that in the case of Junge distributions which extend significantly into the Aitken size range, the Aitken nuclei determine the optical scattering properties

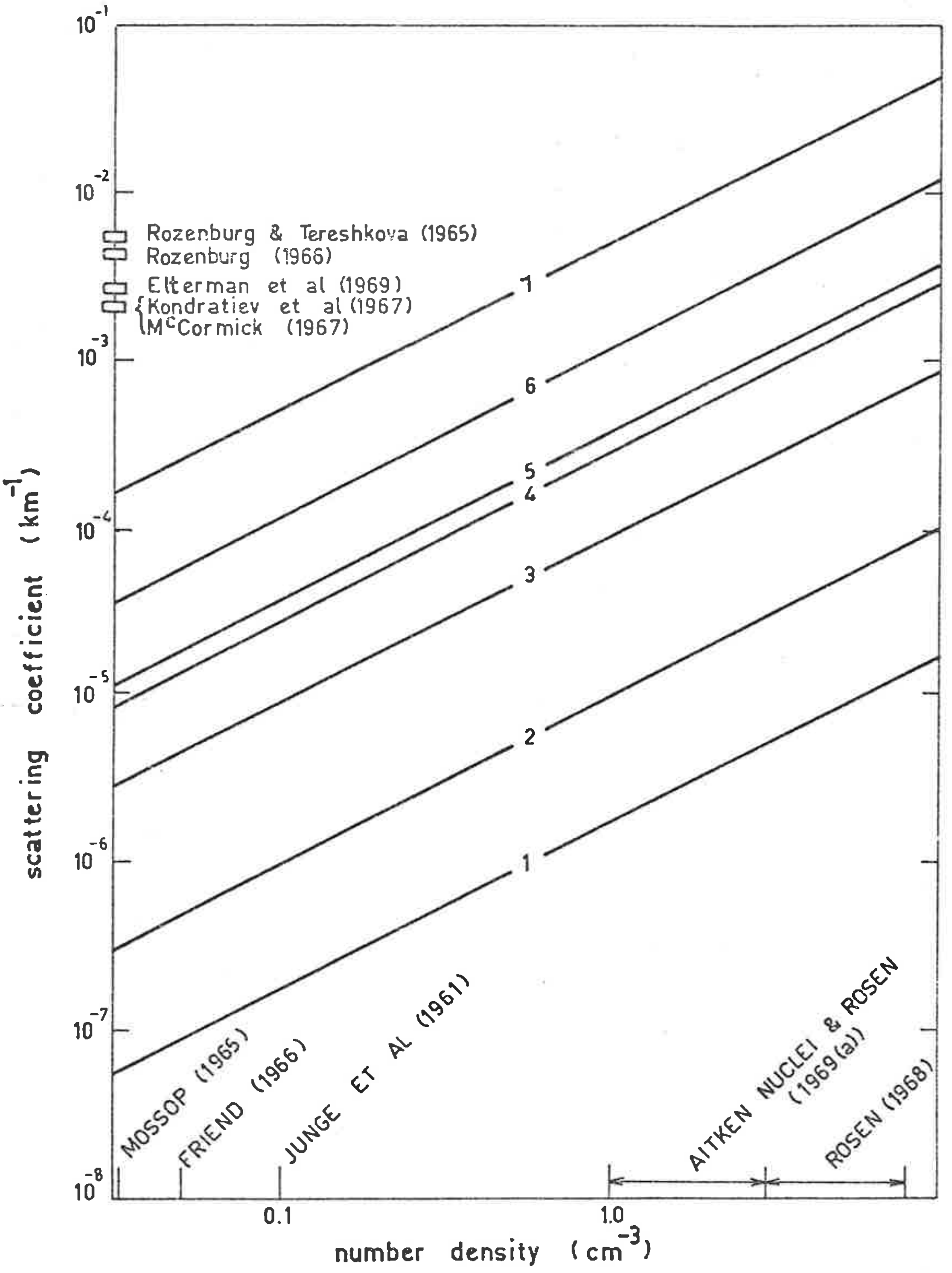

FIGURE 3.5 Variation of aerosol scattering coefficient ($\lambda = .55\mu$) with number density for different size distribution models. Refractive index of 1.4 assumed.

of the aerosols due to their overwhelming numbers. The results of the present calculations for these distributions are shown as curves 1 to 3 in Figure 3.5, and it is evident that all are incompatible with the optical observations. This is not unexpected because stratospheric optical scattering measurements do not show the same rate of change with height as the Aitken nuclei variation. The variations with height of optical scattering observations in the stratosphere are more consistent with the distribution of large particles, which shows a broad maximum in the lower stratosphere.

Size distributions favouring the large particles are shown as curves 4 to 7 in Figure 3.5. It is clear that large particle number densities measured by the impactor technique (Junge et al, 1961; Mossop, 1965; Friend, 1966) are unable to account for the observed scattering coefficients, whereas the observations of Rosen (1964, 1968, 1969(a)) using an optical particle counter are consistent with the optical measurements. As explained in Chapter 1, the principal difference between the two types of measurement is that whereas the collector type of experiment will only measure the non-volatile component of the aerosols efficiently, the in situ optical method includes condensed vapour. Curves 4 and 5 are representative of Junge size distributions with lower cut-off radii near 0.1 μ and exponents ν of 2.5 and 2.0 respectively. The former size distribution was proposed by Newkirk and Eddy (1964) as a result of solar aureole measurements, and later supported by the laser radar measurements of Pilipowskyj et al (1968). The size distribution giving rise to curve 5 is consistent with the measurements of Chagnon and Junge (1961). Figure 3.5 shows, however, that curves 4 and 5 only result in agreement between extreme values of measured aerosol quantities, as the highest number densities measured at mid-latitudes by Rosen (1968) give rise to lowest values of observed aerosol scattering coefficients.

On the other hand, curve 7, which was deduced using Rosen's (1968) earlier size distribution functions, gives rise to scattering coefficients larger than the measured values. Figure 3.5 shows that the exponential size distribution function and the lognormal distribution (both corresponding to curve 6) are in good agreement with observed aerosol properties. These functions are shown in detail in Figure 3.6. Both have been normalised at their maximum values.

Of importance to optical measurements in the stratosphere is the wavelength dependence of the aerosol scattering coefficient. The total scattering cross-section, $\bar{\sigma}_A$, was accordingly calculated for a range of wavelengths, and for the lognormal and exponential size distributions. It was found that the cross-sections, and hence scattering coefficients, calculated using both size distributions are nearly independent of wavelength, at least in the visible region of the spectrum.

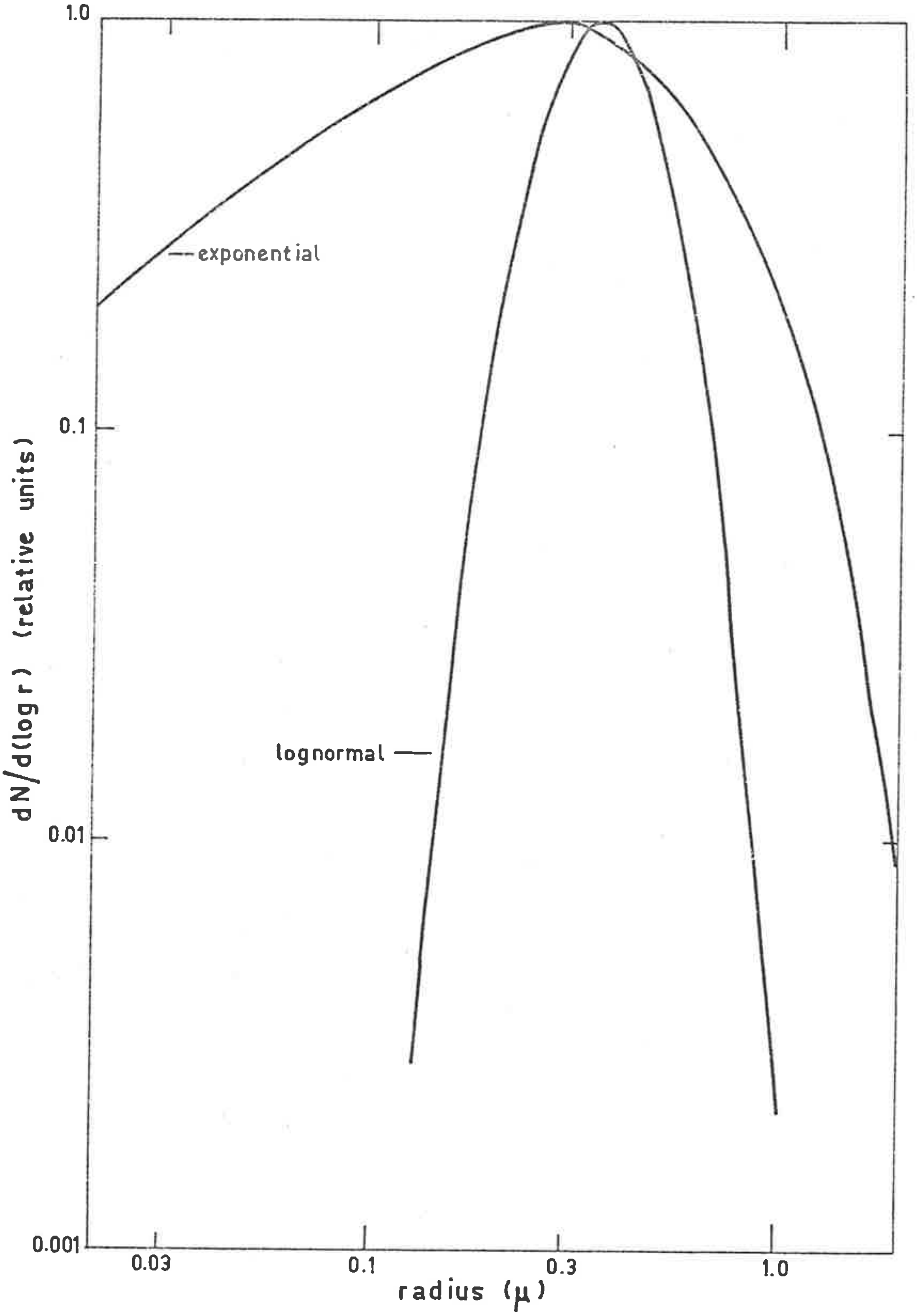

FIGURE 3.6 Most probable size distribution functions of the stratospheric aerosol .

CHAPTER FOUR

DATA REDUCTION

Scattering profiles up to 10 km can be readily obtained using the analogue recording method with as few as 4 or 5 laser firings. The backscattered signal from above approximately 10 km is so weak for the present lidar equipment that significant fluctuations in the mean photomultiplier anode current are observed. These fluctuations are caused by the arrival of discrete light photons, and under such conditions, it is necessary to revert to pulse counting techniques.

In the following sections, a description is given of the steps taken to correct and overlap the lidar data in order to produce a composite scattering index profile. An approximate method of separating the aerosol and molecular component of the backscattering coefficient will also be discussed.

4.1 Pulse Counting System

4.1.1 Resolving Time Corrections

In Chapter 2 the results of an experiment to determine the linearity of the 10-channel pulse counter were presented. It was shown that even at relatively low count rates the observed count became less than the true count due to the finite resolving time of each counter. The departure from linearity of the counting system is shown as a function of count rate in Figure 2.7, together with theoretical curves based on equation 2.1. The theoretical curve described by equation 2.1 with t =55 nsec is used to correct the count recorded in each channel.

For observations up to 20 km altitude, the scattered light is attenuated in order to reduce the maximum observed count rate to less than 3 MHz. The correction made to the observed count in any channel is then never greater than 20%. At this count rate, an error of 10% in the estimation of the resolving time of the counter system would give rise to an uncertainty of 3% in the correction applied.

Although the actual count rate varies during the time that a channel is open, it can be shown that the error introduced by correcting the average count rate is never greater than 1%.

4.1.2 Background Corrections

The background noise is composed principally of three components; "dark" counts from the photomultiplier, sky background radiation, and a contribution due to multiple scattering. Dark pulses emanate from the photomultiplier even in complete darkness due to thermal emission, and can be reduced by cooling the photomultiplier. In the equipment described here, a Peltier cell is used to lower the temperature of the photomultiplier to - 15°C, and the resulting "dark" count is 120 sec^{-1}.

Radiation from the night sky background in the absence of terrestrial sources is comprised of airglow components, and to a lesser extent, starlight and zodiacal light. The count rate due to the sky background radiation depends on the width of the interference filter used in the detector system. In the present apparatus, the width of the interference filter is 8 Å, and the sky background signal in the absence of moonlight and interference from city lights can be as low as 60 $\sec^{-1}$. At the Adelaide observing site in the centre of the city the sky background contribution has a minimum value of about 130 $\sec^{-1}$. In the presence of moonlight there is a rise in the background count, the magnitude of which is dependent on the haziness of the lower atmosphere.

The third factor of importance to the background noise count is the contribution due to multiple scattering of the main laser pulse into the field of view of the receiver. The effect of multiply scattered light was estimated by deliberately misaligning transmitter and receiver beams, and firing the laser. The multiple scattering contribution appeared to decrease with time at a similar rate to the primary scattered light. In Table 4.1 the multiple scattering contribution is compared with typical signal counts and photomultiplier plus sky background noise for various channel heights. The multiply scattered contribution has been extrapolated above 30 km.

TABLE 4.1

Height (km)	Units: Counts/km Channel Width/100 Shots		
	Multiply Scattered Light (Filtered)	Photomuliplier Plus Sky Noise (Filtered)	Normal Signal (Filtered)
10	2×10^{1}	1.7×10^{-1}	2.5×10^{3}
20	1.3×10^{1}		1.6×10^{3}
30	1.3×10^{0}		1.6×10^{2}
40	1.5×10^{-1}		1.8×10^{1}
50	2.7×10^{-2}		3.2×10^{0}
60	4.7×10^{-3}	1.7×10^{-1}	5.6×10^{-1}

It can be seen that multiply scattered light dominates the total background count for altitudes less than 30 km, but becomes insignificant compared with photomultiplier plus sky background noise for altitudes above 50 km. Nevertheless, the total noise count is much less than the signal count from altitudes less than 60 km, and the maximum height limit of the present equipment is determined by statistical errors due to insufficient signal counts in each channel.

4.1.3 Statistical Errors

Statistical errors in the recorded photon counts can be estimated using Poisson statistics for random events. It can be shown that the fractional error e corresponding to one standard deviation in counting N photons is given by the equation

$$e = \frac{N^{\frac{1}{2}}}{N - m} \qquad (4.1)$$

where m is the average number of noise counts expected. Inspection of Table 4.1 shows that below 50 km m is insignificant compared with N. Above 50 km, m is almost entirely due to photomultiplier dark counts and sky background noise, and hence can be accurately measured by averaging over a large time interval, usually about 10 sec.

4.1.4 Count Rate Corrections

The count recorded in a given channel is the integral of received photons over a particular height range. Data of this nature would normally be plotted as a histogram, but it was considered that a continuous curve would be more representative of the actual atmosphere.

In order to present the data in continuous form it is necessary to correct the count in each channel for the non-linear variation with time of the count rate during the time that the particular channel is open. Alternatively an equivalent height for each channel could be calculated, but this method leads to unwieldy height values for the counter channels. As the count rate can vary significantly from one sounding to another, it has been found necessary to calculate the count rate from the data to be corrected.

The method of correcting the data is as follows. It is assumed that the variations in the total counts in the successive channels give an approximate measure of the relative variation of count rate in each channel. In practice, the counts from the channel to be corrected and from the two nearest channels, together with the heights corresponding to the midpoints of the channels, are used to define a quadratic of the form

$$y_1 = ah^2 + bh + c_1 \qquad (4.2)$$

According to the assumption outlined above, the count rate in the channel to be corrected is of the form

$$y_2 = ah^2 + bh + c_2 \qquad (4.3)$$

The basic assumption, and hence equation (4.3) is valid provided the slope of the count rate changes monatonically over a single channel. The total count C in the channel is then given by

$$C = \int_{h_1}^{h_2} y_2 \, dh \qquad (4.4)$$

where h_1 and h_2 are, respectively, the lower and upper altitude limits of the channel. Thus the constant c_2 is uniquely defined, and equation (4.3.) can be used to calculate the actual count rate at the midpoint of the channel.

The above method is used to correct photon counts from heights less than 30 km, where the channel width is normally 1 km. At greater heights, statistical errors become increasingly significant, and give rise to erronious values of count rate. The data are therefore corrected on the basis of a theoretical molecular atmosphere. In this case, the count in a given channel is assumed to be proportional to $\{\exp(-h/H)\}/h^2$, where $H = H(h)$ is the density scale height of the molecular atmosphere at height h. For altitudes greater than 35 km, the density scale height H is derived from the U.S. Standard Atmosphere (1962), and values are reproduced in Table 4.2.

TABLE 4.2

Height (km)	Scale Height (km)	Source of Data
22.5	5.085 *	Calculated from data
26.5	5.666 *	
30.5	5.666 *	
34.5	6.204 *	Interpolated
38.5	6.741	U.S. Standard Atmosphere, 1962
42.5	7.052	
46.5	7.365	
50.5	8.049	
54.5	8.432	
58.5	8.191	

* Typical values

In the vicinity of 30 km an effective scattering scale height is calculated from the data, since the presence of aerosols can affect the count rate. In the region between 30 and 35 km, the effective scale height is interpolated.

4.1.5 Overlapping of the Data

In sounding of the atmosphere using the pulse counting technique a problem peculiar to the particular equipment has arisen. Using ten counter channels it is necessary to overlap several groups of soundings in order to cover a useful height range with a sufficiently small height resolution. Several combinations of counter delay and width settings have been tried, and the optimum configuration is listed in Table 4.3. The region from 8 to 30 km is covered in three groups of soundings, and the height range 20 - 60 km is covered in one sounding using a channel width of 4 km.

TABLE 4.3

Height Range (km) (Centre of Channel)	Delay (km)	Width (km)
9 - 14 *	8.5	1
13 - 22	12.5	1
21 - 30	20.5	1
22 - 58	20.5	4

* Terminated at 6th Channel

The number of laser firings is determined by the accuracy required, and in the present work, the accuracy corresponding to one standard deviation of the count in the last and least accurate channel is usually set at 5%. A total of at least 400 counts in the last channel is thus normally obtained. However, inspection of Table 4.1 shows that a prohibitively large number of laser firings would be necessary to achieve an accuracy of 5% at 58 km. In practice, the counts observed with a delay of 20.5 km and a 4 km channel width are normally integrated over 500 firings, for which the accuracy in the last channel is about 35%. These errors are considerably reduced when the results of soundings over several nights are added to give monthly mean profiles.

4.2 Analogue Recording System

A scattering profile up to about 10 km is obtained from 4 or 5 laser firings using the analogue recording apparatus. As remarked in Chapter 2, some characteristics of optically dense aerosol layers in the first 2 or 3 km of the atmosphere can be investigated in real time without any subsequent processing, as these layers are easily identified on the A-scan trace.

In addition to visual inspection, the data are processed so that backscattering coefficients can be derived. The traces recorded on Polaroid film are digitised, and the results from all the photographs, representing different height intervals, are overlapped.

The sky background contribution is automatically determined during the experiment by causing the oscilloscope to sweep without firing the laser. During the day, noise due to the sky background determines the upper altitude limit of observations. For small solar zenith angles of about 30°, observations are limited to heights below 4 to 5 km. As the sun approaches the horizon, the sky background contribution becomes insignificant, and observations are limited to 10 km by fluctuations in the signal due to individual photons.

4.3 Processing Common to Both Recording Systems

The total profile of relative signal derived from both analogue and digital systems is finally converted to values of scattering index, I(h) (see Chapter 3).

4.3.1 Normalising the Lidar Results

In Chapter 3 it was shown that it is necessary to compare lidar values of scattering index I(h) with theoretical values for a molecular atmosphere in order to deduce quantitative information about the scatterers. A departure of the experimental values from the theoretical is interpreted as indicating the presence of aerosols.

The theoretical curve for molecular scattering is fitted to the experimental curve at a height, hcal, where it is considered that the aerosol contribution is negligible. Examination of the literature to date on the variation of aerosol scattering with height reveals two contrasting groups of experimental results. On the one hand, analyses of horizon photographs taken by astronauts (Rozenberg, 1966a) and results of searchlight probing (Rozenberg, 1960; Elterman et al, 1969) indicate that scattering by aerosols is significant compared with molecular scattering up to heights of at least 35 km. In particular, the recently published results of Elterman et al (1969) show a minimum tropospheric turbidity of 0.5 at 5 km, and a similar turbidity at 35 km.

On the other hand lidar scattering index values of Kent et al (1967) decrease at the same rate as the pure molecular atmosphere over the height range from 30 to 70 km, suggesting that the atmosphere is essentially purely molecular over this height range.

However, the same rate of change of scattering index would result if the aerosol turbidity remained constant with height. Nevertheless the major proportion of the stratospheric aerosol would be expected to decrease with height above the 30 km region, as they appear to originate from the lower stratosphere (Rosen, 1969(c)). Thus the background turbidity contribution, indicative of a source above the lower stratosphere, is considered negligible, at least within the accuracy of present laser radar experiments.

In addition, airborne measurements of solar radiation (Kondratiev et al, 1967) showed a minimum in aerosol scattering at 12 km, where the turbidity was less than 0.1. A peak turbidity of 2 was observed at 17 km. It is of interest to note that the vertical profile of aerosol scattering deduced by the solar radiation measurements is in agreement with the number density profiles observed by Rosen (1964, 1968) using a balloon-borne photoelectric particle counter. The number density measured by Rosen increased by an order of magnitude between 10 and 20 km, and decreased by the same factor between 20 and 30 km. If the averaged scattering cross-section of the particles remains the same throughout the height interval 10 - 20 km, then according to the relation in equation 3.31 it follows that the aerosol scattering coefficient varies by an order of magnitude.

The minimum aerosol scattering coefficient in the vicinity of 10 to 12 km is not inconsistent with the concept that the majority of aerosols in the stratosphere and troposphere appear to originate from different sources. It is therefore not unreasonable to expect a significant difference in aerosol scattering between the upper troposphere and the lower stratosphere. Aircraft measurements (Cadle et al, 1969) support this view.

It appears from the above discussion that the first group of experimental results, which include those of Elterman et al (1969), do not represent the normal atmosphere. Two further points emerge from the considerations above. A minimum in aerosol scattering is to be expected in the region of 10 km, and above 30 km the atmosphere is predominantly molecular.

In normalising experimental scattering data, many workers have employed density values from standard atmospheres. However, data published in the U.S. Standard Atmosphere Supplements (1966) show significant latitudinal and seasonal departures of density values from the U.S. Standard Atmosphere (1962). In the height region of interest to the present work, and at 30° latitude, the maximum departure occurs at a height of 15 km, where the density departure varies from + 7% in winter to + 16% in summer.

In the present investigations, therefore, the results of daily radiosonde flights conducted by the Commonwealth Bureau of Meteorology at Adelaide are used to compute the molecular contribution to the scattering index. Unfortunately, the maximum height reached by most flights rarely exceeds about 32 km, and is often less. Hence a much lower height for normalisation of the lidar results was sought.

The existence of a minimum in aerosol scattering in the region of 10 km has already been discussed, and in the present work the 10 km level is chosen as the height of normalisation.

In addition to the theoretical scattering index curve based on radiosonde data, a second theoretical curve using density values from the U.S. Standard Atmosphere (1962) is calculated and fitted to the radiosonde values. On most occasions the two theoretical curves tend to overlap at approximately 30 km, although occasional differences of up to 5% have been observed.

It has been found necessary to use the data from the 2300 hrs G.M.T. local radiosonde flight in calculating the molecular values of scattering index. Whereas the 1100 hrs flight ascends to about 18 km, the flight at 2300 hrs normally reaches altitudes between 26 and 32 km. According to the U.S. Standard Atmosphere Supplements (1966), diurnal density variations between 3 and 30 km amount to less than 2%, so that the lidar and radiosonde observations can be made several hours apart without introducing serious errors.

4.3.2 Corrections for Transmission

In solving the lidar equation 3.5 , discussed more fully in Chapter 3, the transmission term is calculated from the lidar results as it is dependent on the measured values of $B_A(\pi,h)$.

Combining equations 3.5 and 3.6,

$$C(h) = \frac{k}{4\pi}\{T(0 - hcal)\}^2\{T(hcal - h)\}^2 \frac{P_A(\pi)\beta_A(h) + P_R(\pi)\beta_R(h)}{h^2} \tag{4.5}$$

An approximate determination of the transmission correction term $\{T(hcal - h)\}^2$ can be made by ignoring the transmission contribution from the height region h to h - Δh, where Δh corresponds to the step in height between data points. Starting at the calibration height hcal, where the scattering ratio R(h) as defined in Section 3.3 is unity, the height h is successively increased by one value of Δh. At each stage, the approximate value of T(hcal - h), which is merely the transmission $T(hcal - h_1)$ derived from the previous step (since $h_1 = h - \Delta h$), is inserted in equation 4.5. The calculated value of $\beta_A(h)$ is then used, together with appropriate values of $\beta_R(h)$ and $\beta_o(h)$, to compute the transmission $T(\Delta h)$ over Δh. Then

$$T(hcal - h) = T(hcal - h_1)T(\Delta h) \tag{4.6}$$

which is finally used in equation 3.8 to produce values of scattering index I(h).

Deirmendjian's (1965) value of 0.25 has been adopted for the value of $P_A(\pi)$ used in equation 4.5. The molecular scattering coefficient $\beta_R(h)$ is calculated according to equation 3.11, using radiosonde data to obtain the molecular number density $N_R(h)$. The aerosol and molecular scattering coefficients are averaged over the height interval Δh for simplicity. The absorption coefficient $\beta_o(h)$ due to ozone is averaged over Δh, and calculated on the basis of Elterman's (1968) method;

$$\beta_o(h) = A_v(\lambda) D_3(h) \tag{4.7}$$

where A_v is the Vigroux ozone absorption coefficient, and equals 2.48×10^{-2} cm^{-1} at the ruby laser wavelength. $D_3(h)$ is the ozone equivalent thickness (cm km^{-1}), values of which are tabulated (Elterman, 1968).

4.4 Computations

All stages of the data reduction are performed with the University of Adelaide's CDC 6400 computer. Scattering indices $I(h)$ and ratios $R(h)$ are automatically plotted, together with error bars corresponding to one standard deviation of the counts recorded. Temperature and humidity values obtained from radiosonde flights conducted at nearby Adelaide Airport are also plotted.

CHAPTER FIVE

STRATOSPHERIC OBSERVATIONS

Routine lidar soundings of the stratosphere began in April, 1969, and continued each evening when conditions were suitable until May, 1970. Thus the results presented here represent over one year's observations. Originally, the observations were carried out at the field station of the Mawson Institute for Antarctic Research, at Mt. Torrens (lat. 35°S, long. 138°W). The field station is about 48 km from Adelaide, and sufficiently removed from artificial sources of light to ensure a minimal background interference. The altitude of the site (583 m) is an important factor in reducing losses in signal intensity due to atmospheric attenuation, which is most significant in the lowest layers of the atmosphere.

Experience showed, however, that the Mt. Torrens site is prone to the formation of mists and fogs, which frequently develop when the air trajectory over the hills area is of maritime origin. The number of observations was therefore severely limited at Mt. Torrens. During the months of September and October, 1969, the lidar equipment was removed from the Mt. Torrens site and installed in a mobile instrumentation van (see frontispiece) on loan from the Department of Supply, Commonwealth of Australia, and consequently no records are available for these months. The mobility of the van will be of benefit for the investigation of spatial differences in aerosol concentrations, and for the comparison of results with those of other more immobile experiments.

At the present time the van is located in the grounds of Adelaide University and near the centre of the city. Measurements have shown the attenuation of the received signal to be 20% greater than at Mt. Torrens. In addition, the increase in sky background by a factor of two results in a net increase in the total noise signal by about 35%. However, as discussed in Chapter 4, the largest source of noise interference is of thermal origin in the photomultiplier. Thus operation of the laser radar at the Adelaide site has not seriously degraded its performance.

In Figure 5.1, experimentally derived values of the scattering index I(h), defined in Chapter 3, are plotted as a function of height over the range 3 - 60 km: the graph is the mean of some 49 profiles taken over the period April, 1969 to March 1970. Included for comparison in Figure 5.1 are curves representing values of I(h) calculated for the case of pure molecular scattering. The continuous curve represents the average of local radiosonde measurements taken on the same days as the laser observations, and the laser results are normalized to the calculated curve at a height of 10 km. The broken curve is calculated on the basis of density values from the U.S. Standard Atmosphere (1962), and is fitted to the radiosonde curve. It is of interest to note that the two molecular curves become nearly identical at 30 km, and hence densities from the U.S. Standard Atmosphere (1962) in the region immediately above 30 km appear satisfactory for the prediction of average molecular scattering profiles at 35°S.

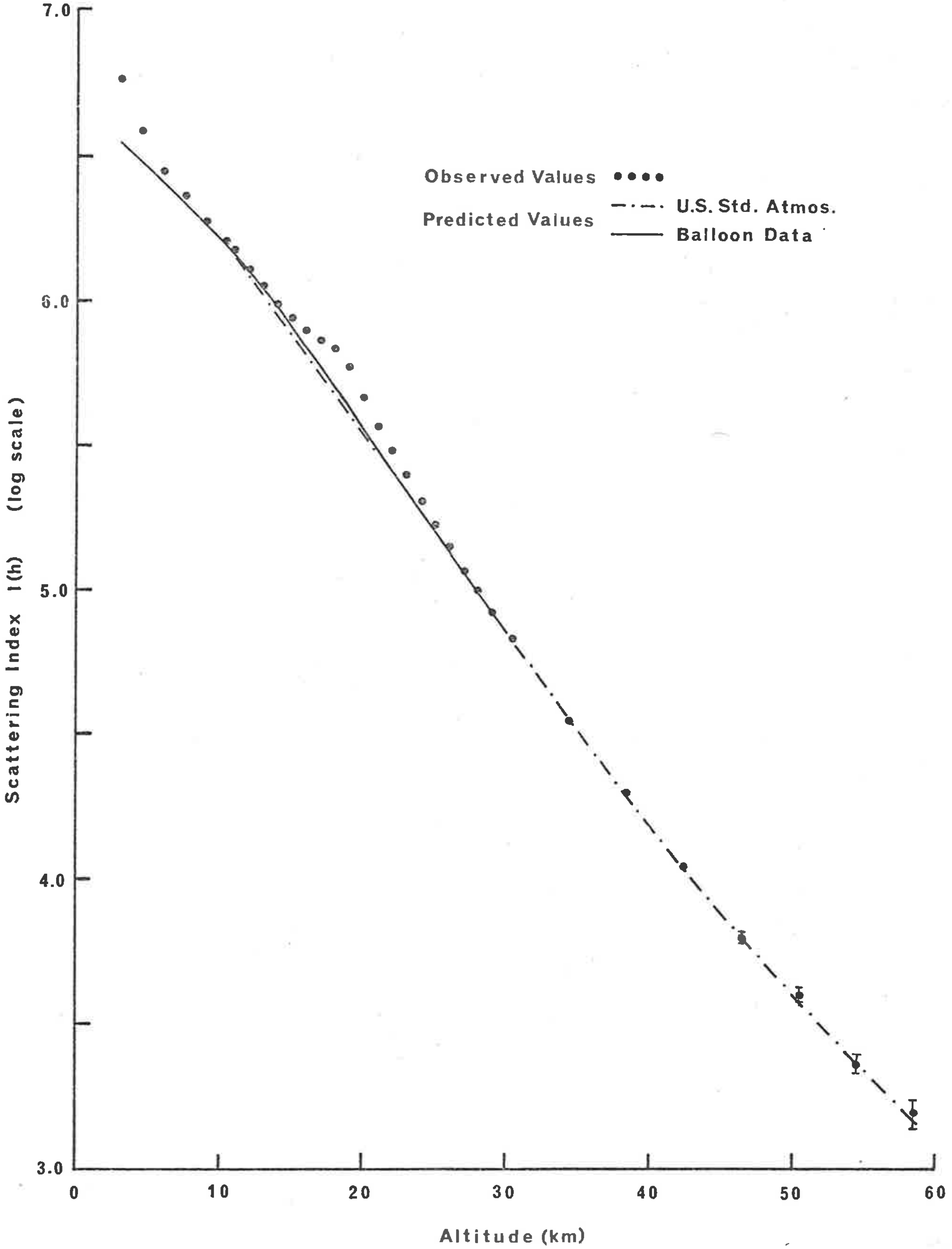

FIGURE 5.1 Observed variation of scattering index during 1969 and 1970, compared with values predicted for a molecular atmosphere.

The experimental values of I(h) are in close agreement with the curves calculated for pure molecular scattering, except in the 13-24 km region, where the experimental values are greater than the theoretical. The departure is interpreted as indicating the presence of aerosols, and the height corresponds to the well known stratospheric aerosol layer. The deviations from molecular scattering become more apparent when the ratio R(h) of experimentally observed to calculated molecular scattering is plotted as shown in Figure 5.2.

For the purposes of discussing the results, it is convenient to divide the observed height region into the 10 - 30 km interval, in which the stratospheric aerosol layer is found, and the 30 - 60 km region, which appears to be predominantly molecular. A discussion of the results follows.

5.1 10 - 30 km Region. General Characteristics

During the process of automatic computation, the experimental values of scattering index I(h) obtained on individual experiments are normalised to theoretical values calculated for a pure molecular atmosphere at 10 km, based on data obtained on local radiosonde flights. It has been found, however, that fluctuations in the signals received in individual experiments can lead to values of scattering ratios less than unity. These fluctuations are partly statistical in nature, while on some occasions they appear to be due to real variations in the aerosol contribution at the normalising height. These records have subsequently been renormalised in the 8 to 12 km altitude region. It is of interest

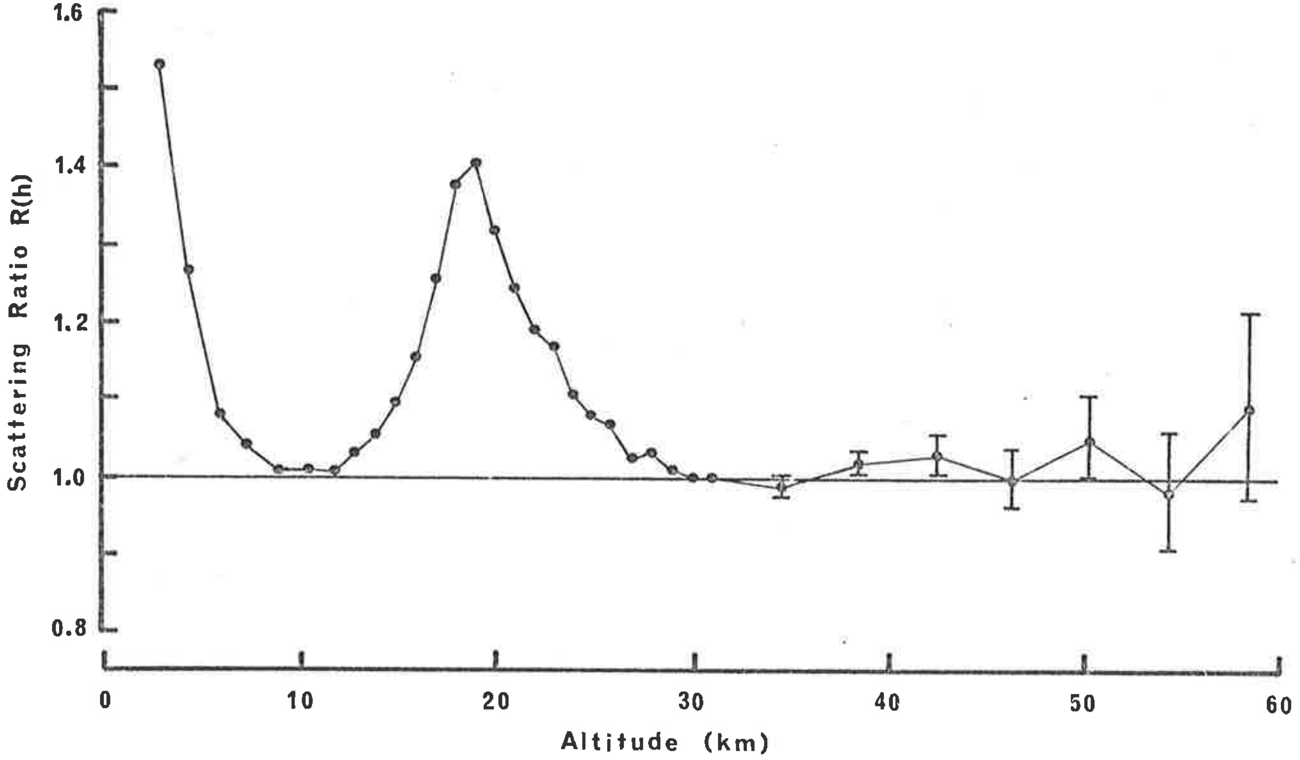

FIGURE 5.2 Values of the ratio R(h) between observed and predicted values of the scattering index for the mean of a year's observations carried out from April, 1969 to March, 1970.

to note that the mean of the scattering ratios measured in 1969 and 1970, shown in Figure 5.2, returns to unity at 10 and 30 km, indicating that on the average, there are equal proportions of aerosol scattering at these heights. On the basis of the evidence presented in the previous chapter, it is concluded that within the experimental error, and under average conditions, the optical turbidity is negligible in the 10 and 30 km regions.

In Figure 5.3, the average scattering ratio profile is compared with results obtained by workers in the northern hemisphere (Clemesha et al, 1966; Grams and Fiocco, 1967; Goyer and Watson, 1968). It can be seen that the shape of the profile obtained in the present work is similar in general character to the profiles obtained in the northern hemisphere, but the magnitudes of the scattering ratios measured in South Australia are significantly less than the northern hemisphere results. The maximum turbidities observed in the present work are less than one half of the corresponding values in the northern hemisphere. Assuming that the aerosol backscattering cross-sections in the two hemispheres are similar, the above result implies that the aerosol number densities measured at 35°S are less than one half of the concentrations measured in the northern hemisphere.

At the present time it is difficult to ascertain whether the observed differences are due to purely hemispherical variations, or to the differing times and latitudes of the compared results. The effect of the Bali eruption in 1963 complicates the comparison of aerosol measurements widely separated in time, as enhanced aerosol concentrations

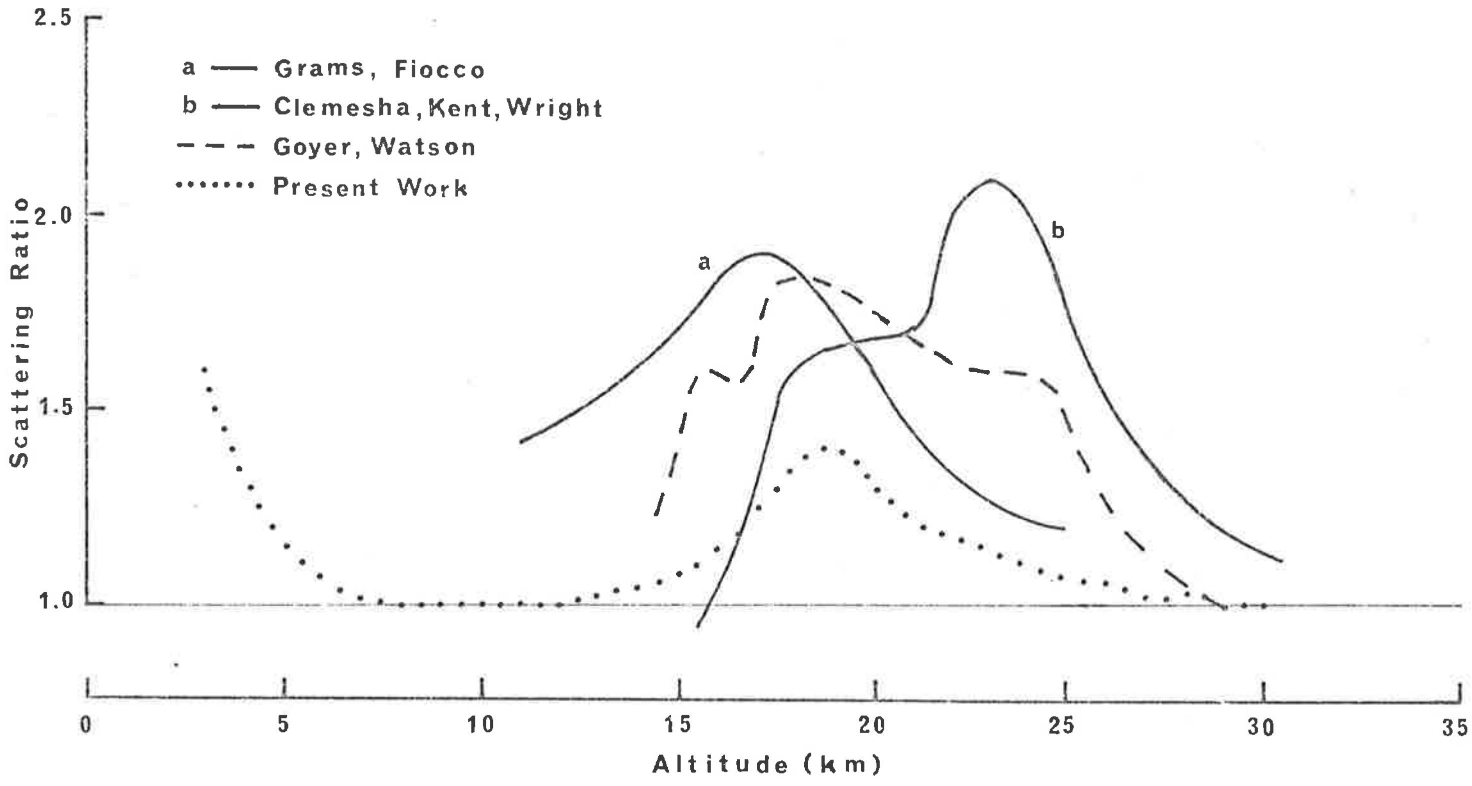

FIGURE 5.3 Comparison of scattering ratio profiles.

in the stratosphere have been noticed for more than three years after the event. The decrease in stratospheric aerosol content at 45°N measured by Rosen (1969(a)) since the Bali eruption is shown in Figure 1.7. The general decreasing trend is still evident in 1966, and a marked seasonal fluctuation is superimposed. Thus, the simultaneous observations of at least one year's duration and at similar latitudes are necessary to resolve the uncertainty.

A number density profile calculated on the basis of the mean laser results and using equation 3.13 is shown in Figure 5.4(a). The aerosol backscattering cross-section $\overline{\Sigma_A(\pi)}$ used in the calculation has the value of 2.616×10^{-14} m^2 $sterad^{-1}$, and corresponds to the exponential size distribution model discussed in Chapter 3. The peak aerosol number density in the stratosphere according to the exponential model is 0.7 cm^{-3}. Included for comparison in Figure 5.4(a) are the results of Rosen (1969(a)) measured in 1968. It can be seen that the present number densities are approximately one third of Rosen's, and are sufficiently close to substantiate the exponential size distribution used in the calculations. On the other hand, the concentrations measured by Chagnon and Junge (1961) are about one order of magnitude less than the optical results, confirming the presence of a significant volatile aerosol component which is not detected by impactor techniques. Curve 4 in Figure 5.4(a) represents a constant mixing ratio, and is proportional to the molecular number density. It can be seen that all profiles fall off with height more rapidly than the slope of constant mixing ratio, indicating that the

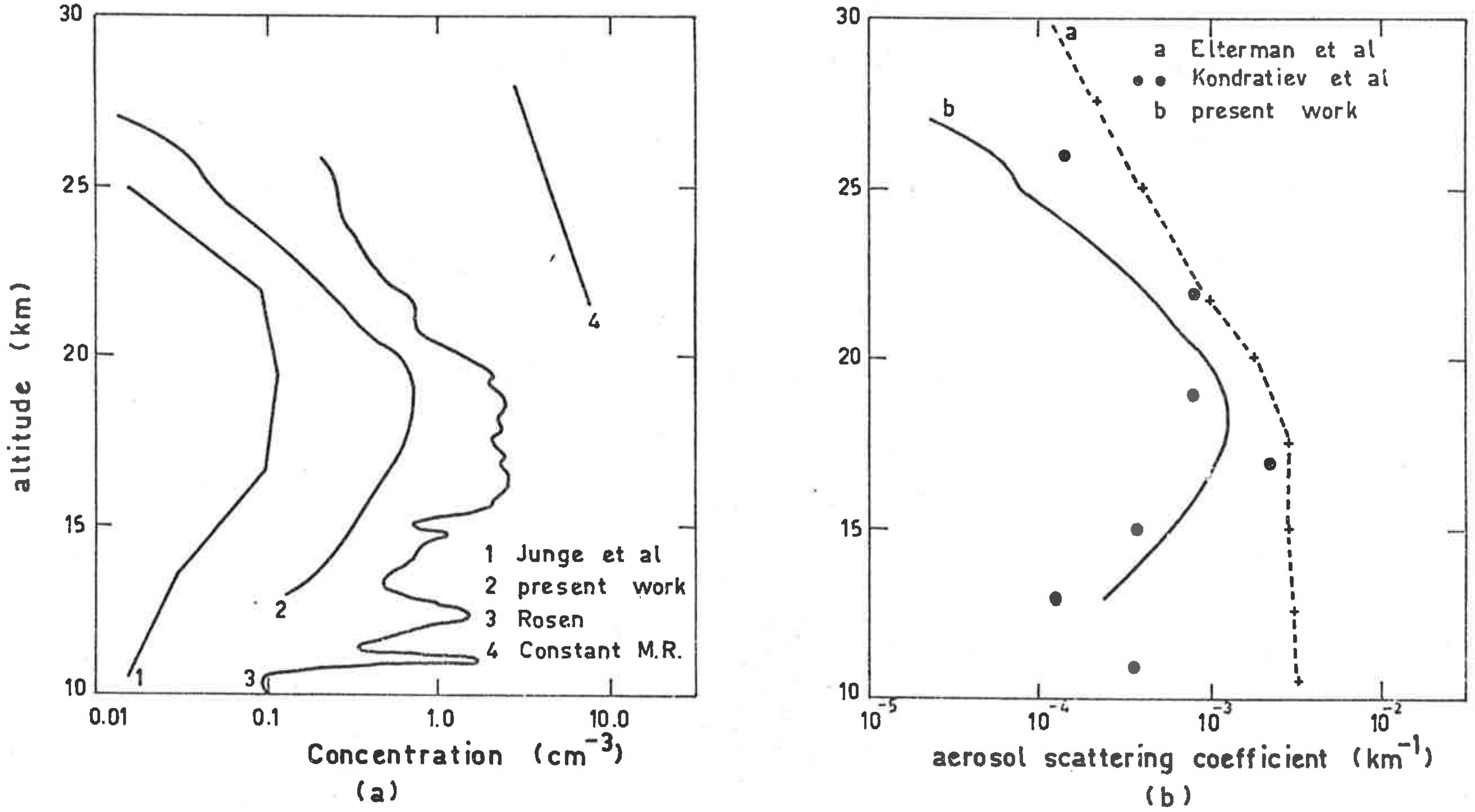

FIGURE 5.4 Comparison of stratospheric aerosol measurements. (a) Number densities. (b) Scattering coefficients.

source of the stratospheric aerosol layer lies in the lower stratosphere.

In Figure 5.4(b), aerosol attenuation coefficients, calculated using equation 3.12 and a value of $\overline{P_A(\pi)}$ based on the above distribution model, are shown as a function of height, and are compared with attenuation coefficients obtained by other workers. The present results are in closer agreement with those of Kondratiev et al (1967), which show a marked minimum at about 12 km, than with the results of Elterman et al (1969), which suggest an almost constant aerosol attenuation coefficient from 5 km to about 18 km altitude.

Assuming the volatile component of stratospheric aerosols to be composed of water droplets, one can estimate the effect of the stratospheric aerosol population on the humidity in the stratosphere. It is now well-established (Mastenbrook, 1968) that the stratosphere is exceptionally dry, compared with the humidities measured in the upper troposphere. Water vapour measurements in the lower stratosphere commonly yield mixing ratios with respect to the dry air of about 10^{-6} gm/gm. It is conceivable that at the low temperatures in the stratosphere, water vapour could condense on the Aitken nuclei already present. Moreover, in the process, the relative humidity of the vapour phase could be significantly reduced. An order of magnitude estimate of the upper limit of such an effect can be made using optical aerosol data. It is assumed that the stratospheric aerosol consists entirely of condensed water vapour, of number density 1 cm^{-3}. In order to simplify the calculations, a mean radius of 0.3μ is assumed, which is consistent with the exponential size distribution model measured by Rosen (1969(a)) and discussed in Chapter 3. Under these assumptions, the water droplet mixing ratio is of the order of 10^{-9} gm/gm, and is very much less than that of the vapour mixing ratio. It is therefore concluded that condensation of water vapour on Aitken particles in the stratosphere has a negligible effect on the stratospheric water vapour mixing ratio.

Individual scattering ratio profiles, compared with corresponding temperature profiles obtained from local radiosonde flights, are presented in Figures 5.5 and 5.6. Two points are noteworthy. The small scale fluctuations in the scattering ratio are not related to the presence of temperature inversions at the same height. This does not indicate, however, that temperature inversions in the stratosphere do not trap aerosols. As the thickness of aerosol layers in the stratosphere is generally less than 300 metres (Bigg, 1969), the present method of integrating over 1 km height intervals will tend to average out the thin layers. The second point worthy of note is the location of the main peak in the scattering ratio in relation to the temperature minimum in the stratosphere. As shown in Figures 5.5 and 5.6, the peak in aerosol scattering does not occur at the height of the temperature minimum, as found by Elterman et al (1969). In general, the present measurements indicate that the peak aerosol concentration in the stratosphere lies approximately 2 - 4 km above the height of the temperature minimum. The height of the peak aerosol concentration obtained in the present work is consistent with corresponding heights measured at similar latitudes in the northern hemisphere (Rosen, 1969(a)).

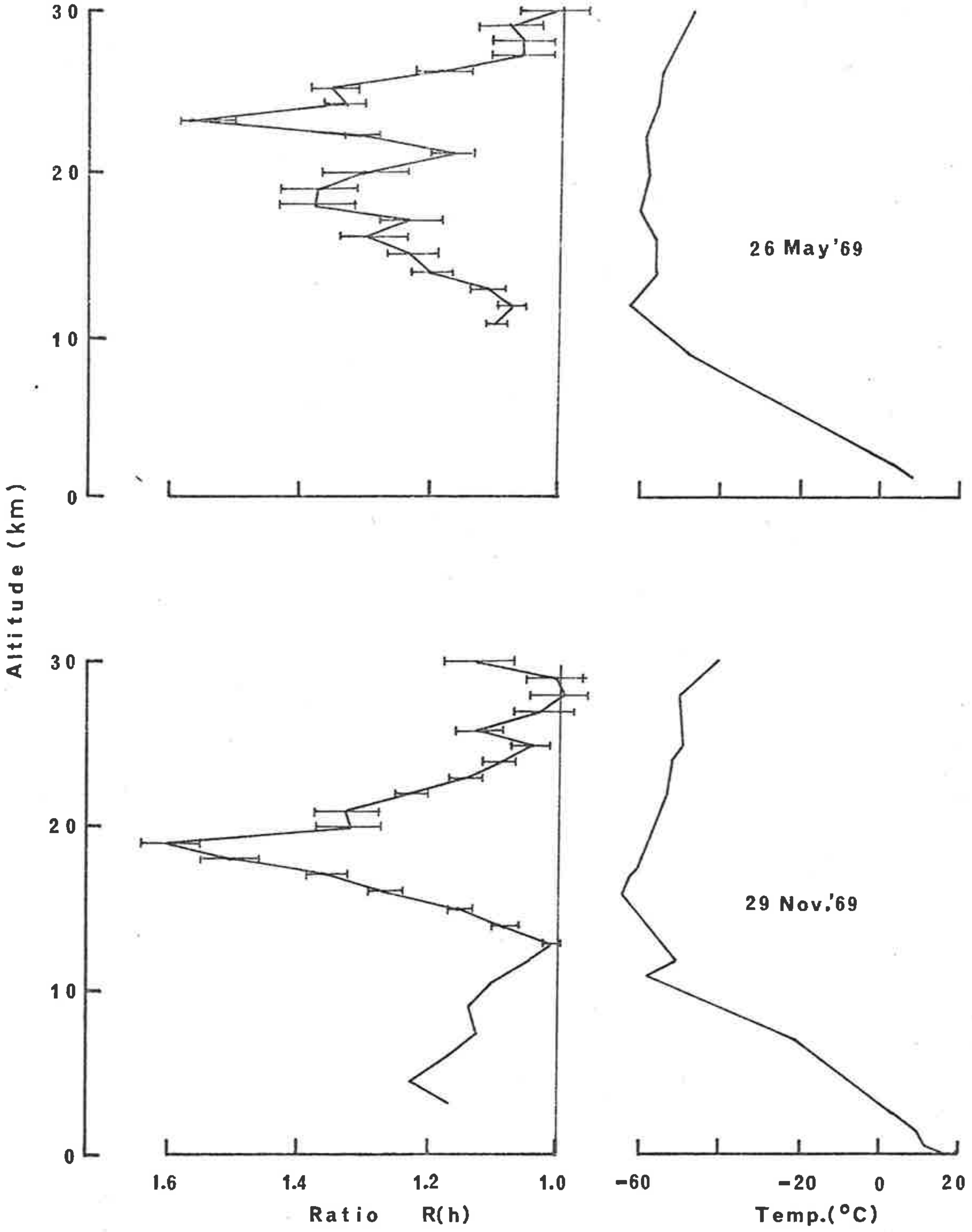

FIGURE 5.5 Scattering ratio measurements compared with corresponding temperature profiles.

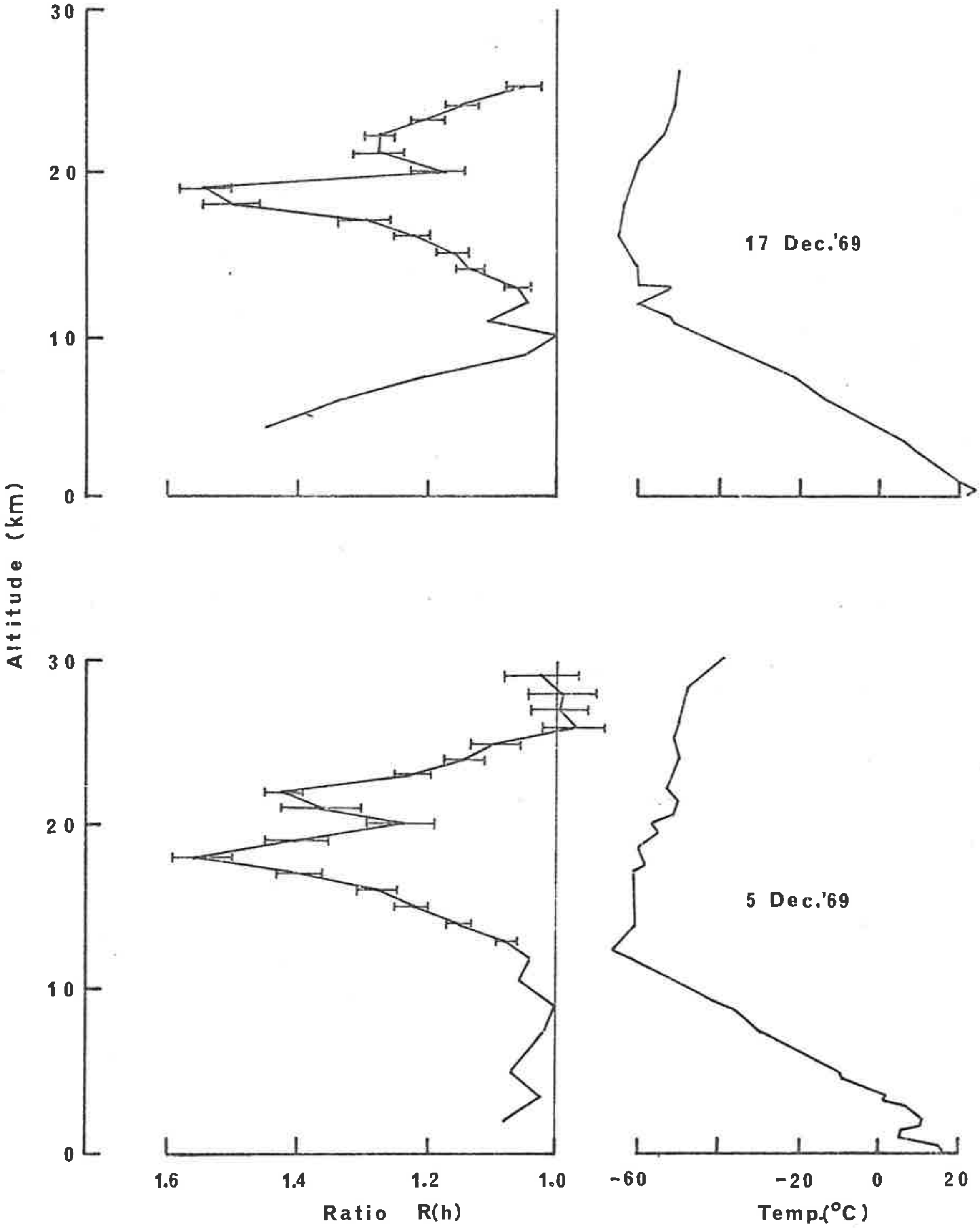

FIGURE 5.6 Scattering ratio measurements compared with corresponding temperature profiles.

Mean scattering ratios for each month of observations are shown in Figures 5.7, 5.8 and 5.9. The vertical lines at each data point represent statistical errors of plus and minus one standard deviation. An annual trend in the peak scattering ratio at 18 km is quite evident. The peak ratio steadily increased from 1.25 in April, 1969, to a maximum of 1.92 in July, after which it tended towards a minimum again in April, 1970. The most recent observations reported here are for May, 1970, and the individual results at the end of May indicate an increasing trend consistent with the annual variation. Unfortunately, for the reasons discussed earlier, no records are available for the months of September and October, 1969. The annual trend in scattering ratio is clearly demonstrated in Figure 5.10, which shows isopleths of mean monthly scattering ratios during 1969 and 1970.

The occurrence of the maximum ratios in the winter of 1969, with a further increasing trend towards the winter of 1970 is in agreement with the well known seasonal variation of transport processes in the lower stratosphere (Brewer, 1949; Dobson, 1956; Newell, 1963). A similar seasonal variation has been detected in volcanic dust injected by the Bali eruption (Dyer and Hicks, 1968), and in the concentration of ozone measured at a similar latitude (Pittock, 1968). As they are most likely to be transported by similar mechanisms, it is therefore not unexpected to find a similarity in the temporal characteristics of ozone and aerosols. These aspects are discussed more fully in the following section.

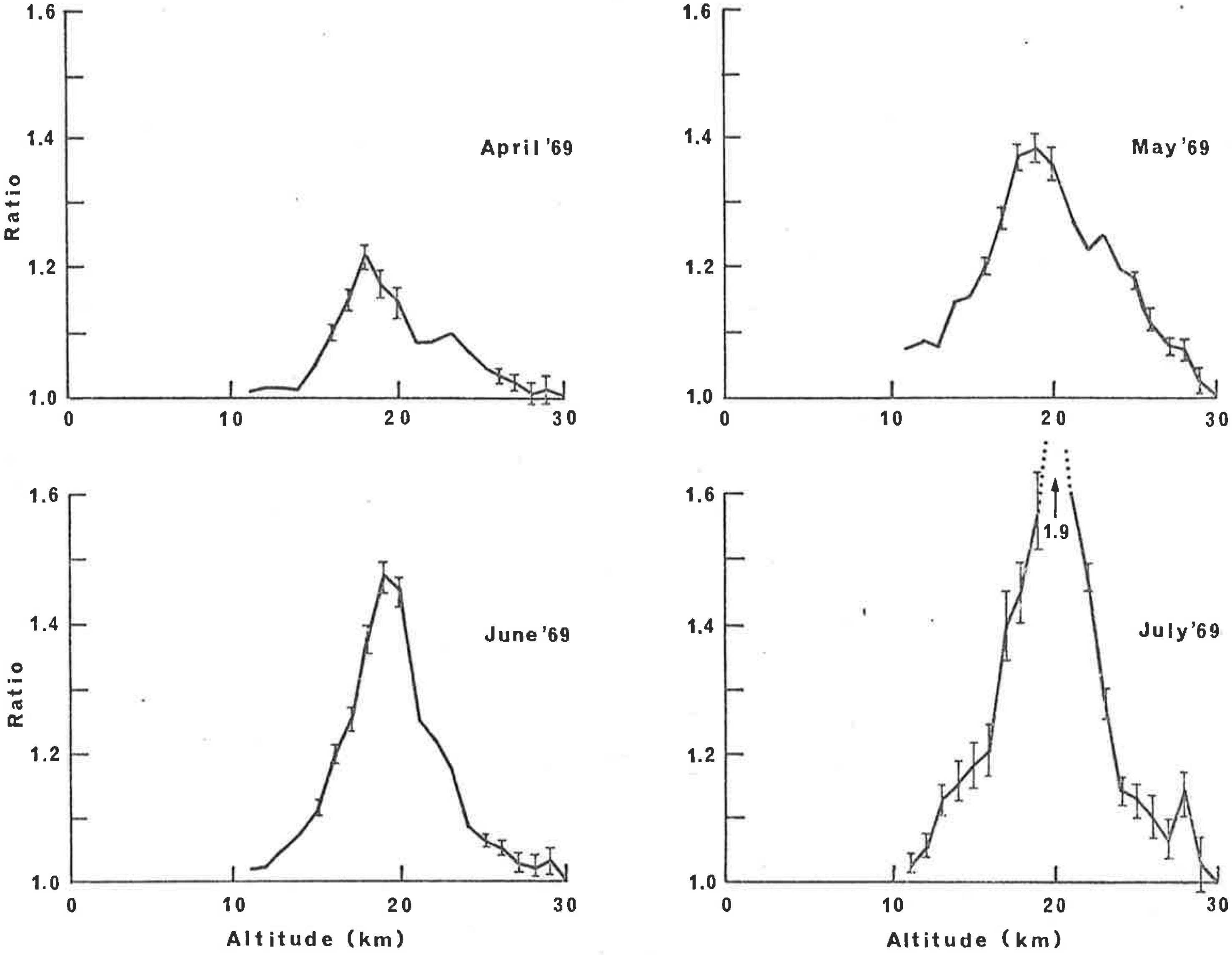

FIGURE 5.7 Monthly mean profiles of the scattering ratio R(h).

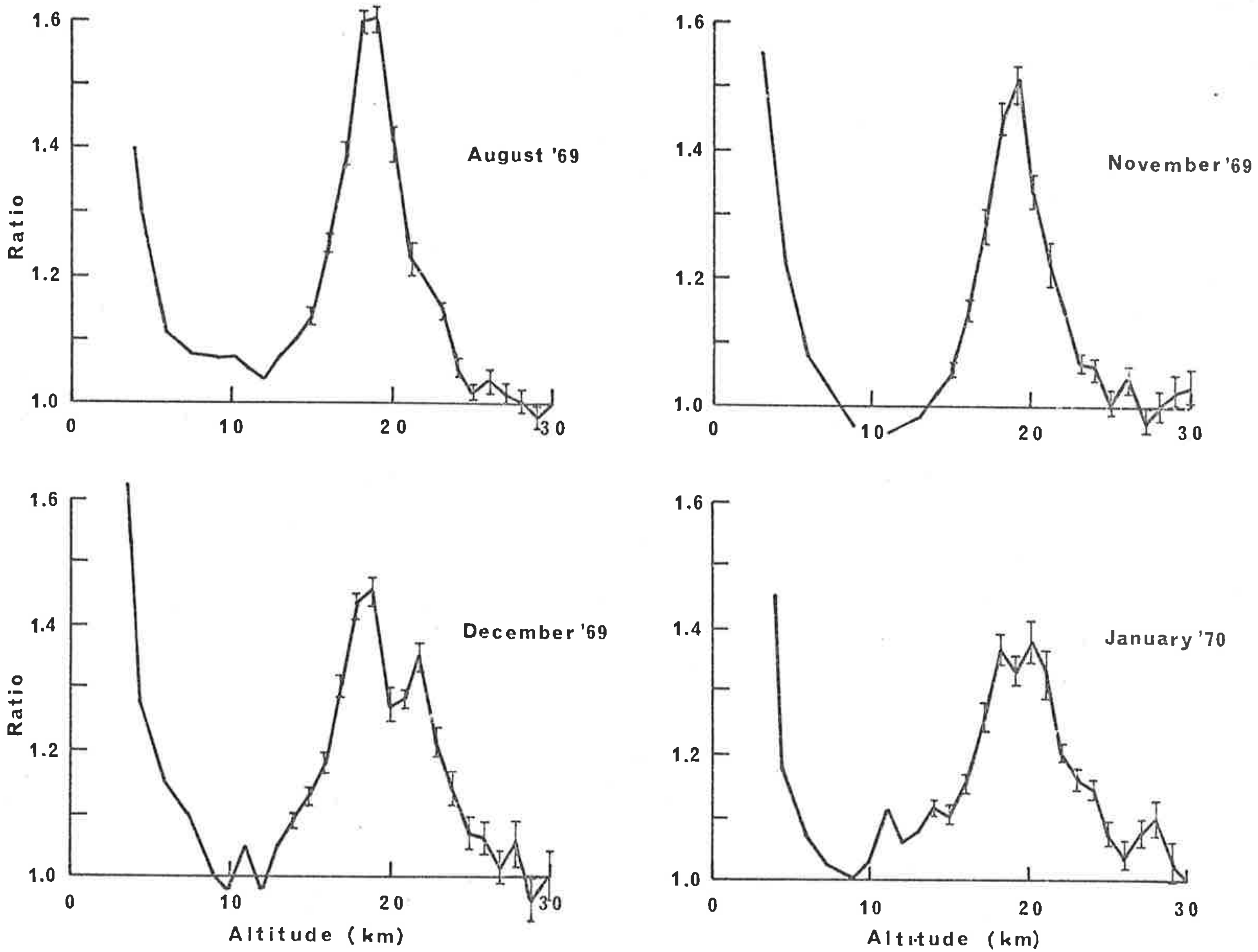

FIGURE 5.8 Monthly mean profiles of the scattering ratio R(h).

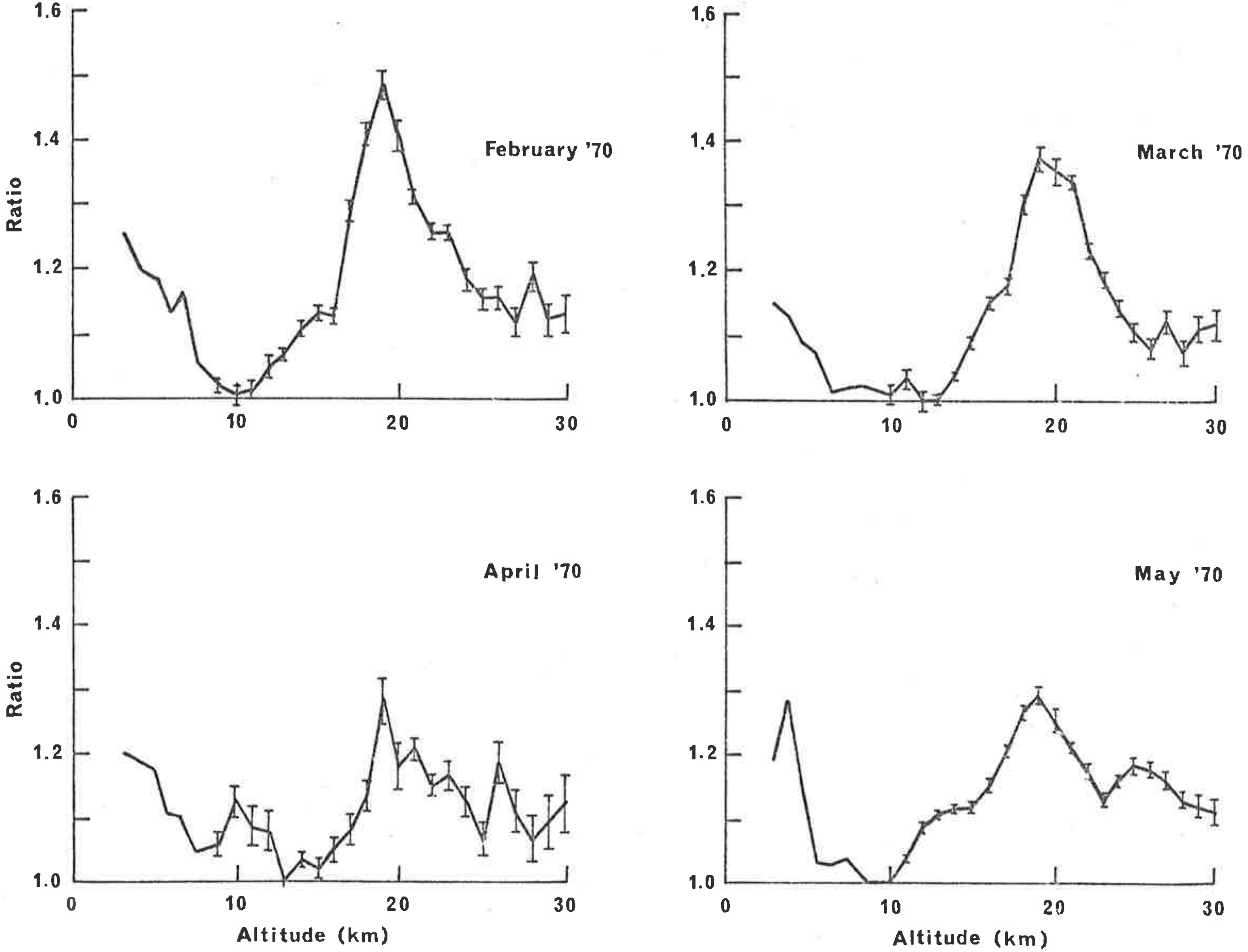

FIGURE 5.9 Monthly mean profiles of the scattering ratio R(h).

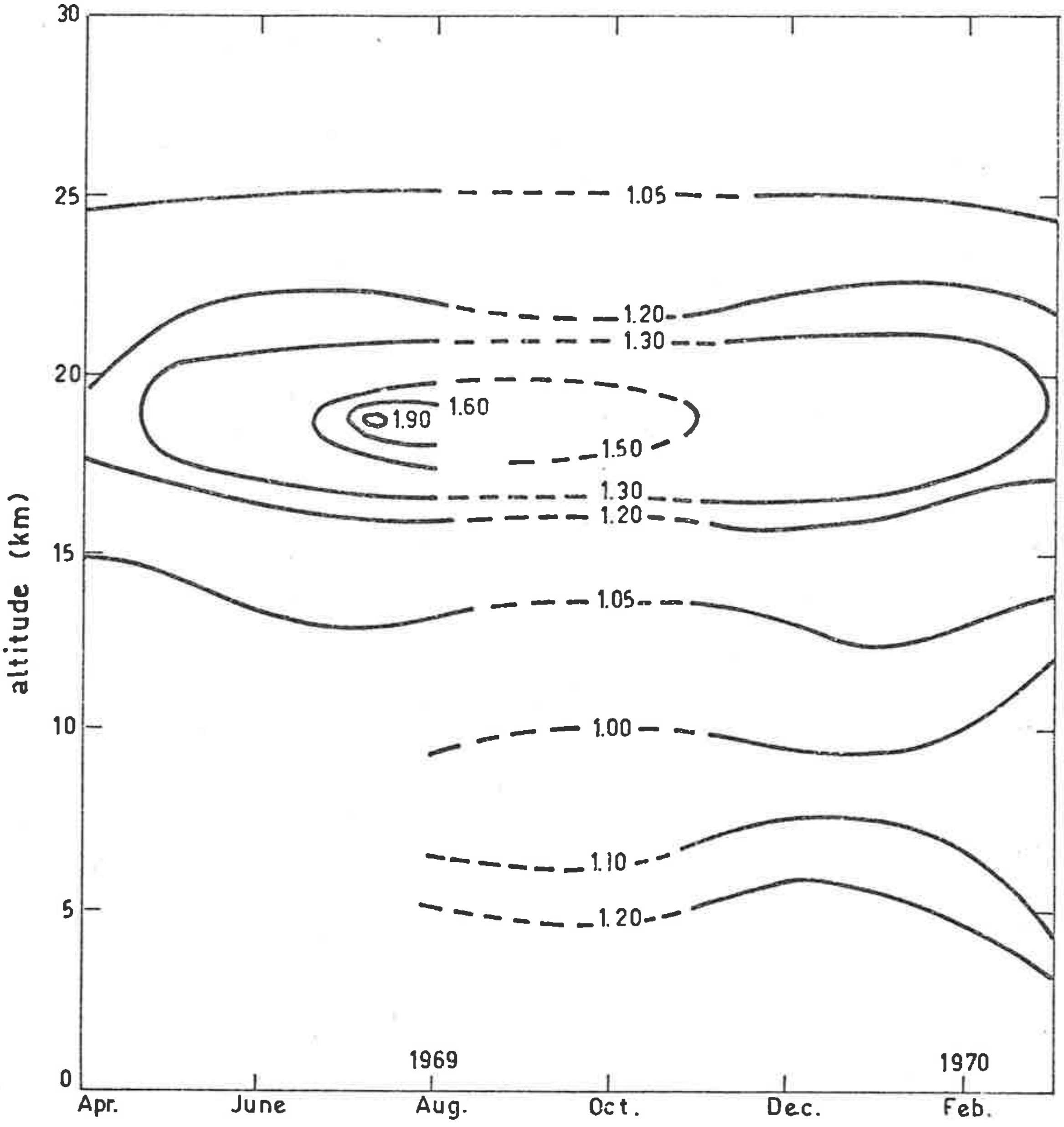

FIGURE 5.10 Isopleths of mean monthly scattering ratios at 35°S during 1969 and 1970.

5.2 Transport of Tracers in the Lower Stratosphere

It has long been recognized that an efficient transport process operates in the lower stratosphere between the equator and pole. For example, the lowest temperatures in the stratosphere are found in the vicinity of the equator, even though this region acts as a heat source, and vice versa, the highest temperatures in the stratosphere are found at the poles, despite the fact that this region acts as a heat sink. This apparent paradox can be resolved if one postulates a mechanism whereby heat is transported from equator to pole. Other observations are indicative of a similar transport mechanism. Photochemical theory predicts the greatest quantities of ozone in equatorial regions and in the summer months. The observation that ozone is found in the greatest concentrations at high latitudes during winter led Craig (1948) to postulate a mean meridional motion from equatorial to polar regions in the lower stratosphere. Brewer (1949) found that the low frost points recorded in the stratosphere were very similar to the temperature of the equatorial tropopause, and suggested that there is a direct mean meridional cell involved with rising motion through the tropical tropopause, a poleward flow, and then sinking motion towards the poles.

In recent years, observations of radioactive tracers (Feely and Spar, 1960), and of the spread of dust from the Bali eruption (Dyer and Hicks, 1968), together with intensive measurements of ozone, have resulted in more sophisticated theories of transport mechanisms. Several authors (Reed, 1953; Martin, 1956) have proposed that the distribution of tracers can best be explained by large scale eddy mixing processes with a flow down the concentration gradient for any particular tracer. It is now known that in middle and high latitudes, eddies primarily control the transfer of tracers in the lower stratosphere by means of correlations between the flow and the tracer fields (Newell, 1963). The meridional cell is still thought to predominate in the tropics, but the relative magnitudes of the two mechanisms are poorly known.

A stratospheric general circulation model has been employed to study the diffusion of two idealized tracers in the stratosphere (Hunt and Manabe, 1968). The three dimensional model covers an altitude range from ground level to 37.5 km, and for the winter and spring months is in agreement with many of the features observed in the atmosphere. The model generates its own meridional circulation and eddies, and thus both the major transport mechanisms in the atmosphere are intrinsic properties of the model. A particularly noteworthy feature of the model is the relationship between the eddy transport process and the upper level trough and ridge system observed in mid-latitudes. The model predicts an accumulation of tracers in the vicinity of upper level troughs, and a deficiency in the region of upper level ridges. This effect is apparently due to the fact that the principal source of the mid-latitude tracer lies in the higher levels of the equatorial region. The only way in which tracer in significant proportions can appear at mid-latitudes is by means of a downwards motion, which is associated with upper level troughs. A similar argument holds in the prediction of low concentrations in the vicinity of ridges. In this case, the vertical motion will actually produce a decrease of concentration because of the vertical concentration gradient of tracer. At the same time as the vertical motions are taking place in the troughs and ridges, an eddy transport mechanism acts in the horizontal direction in such a way that the tracer in the region of a trough is transported polewards, while in the vicinity of a ridge, equatorwards motion prevails. As the maximum concentrations of tracer are located in the trough system, the result is a net downwards transfer of material from equator to pole. Transport is achieved essentially by means of an eddy process, as the troughs and ridges represent the eddies of the general circulation flow pattern. The inability of the model to explain the easterly winds in the summer stratosphere is indicative of a different transport mechanism operating at this time, and hence the transport of material from equator to poles is essentially a seasonal process.

The predictions of the model of Hunt and Manabe are borne out in experimental observations of ozone. As this tracer has been observed for a number of years, there is a considerable amount of data available for statistical studies. Several workers (Normand, 1953; Kawamura, 1957; Ohring and Muench, 1960; Kulkarni, 1963) have related ozone concentrations to the upper level synoptic pattern, and have shown that troughs are associated with high ozone amounts, and ridges are relatively poor in ozone. Ohring and Muench (1960) suspect there is more total ozone immediately ahead of lower stratosphere troughs than immediately behind. It is of interest to note that this aspect is predicted by the model of Hunt and Manabe. Recently Pittock (1969) has reported an extensive statistical investigation of the relation between ozone amount and the synoptic pattern. The results verify the trough-ridge pattern, and also indicate considerable transfer of stratospheric air into the troposphere, and vice-versa by "folding-in" in the vicinity of the middle-latitude jet stream along the 300 mb trough. This folding process has been shown to exist by other workers (e.g. Cadle et al, 1969). There are periods when the synoptic pattern-ozone relationship breaks down (Kulkarni, 1963). Boville and Hare (1961) suggest that much of the remaining variance of total ozone is due to vertical motion in the baroclinic waves of the polar night westerly vortex affecting layers from 150 mb to above 25 mb.

Other relationships between ozone and meteorological parameters have been reported. Meetham (1937), Ohring and Muench (1960), Kulkarni (1963, 1968) and others have shown that ozone fluctuations are positively correlated with the temperature and equatorward component of the prevailing wind, and negatively correlated with geopotential and tropopause heights. The positive correlation with temperature, coupled with the negative correlation with tropopause and geopotential heights, suggests that the short term fluctuations of ozone are due primarily to subsiding air motion, accompanied by adiabatic heating. On the other hand, the positive correlation of ozone concentration and equatorward component of the prevailing wind, and with the temperature supports the concept of horizontal advection from the direction of the pole, where there is more ozone and where the temperature in the winter stratosphere is greater. Kulkarni

(1968) suggests that at 38°S vertical motions are more important than advection at the 20 mb level in winter, while in the lower stratosphere, both advection and vertical motions are responsible for changes in ozone.

It is now pertinent to discuss features of the aerosol measurements obtained in the present work in the light of the transport mechanisms reviewed in the preceding paragraphs. It is important, however, to stress the limitation of the laser radar in meteorological studies such as this. The ruby laser beam is unfortunately unable to penetrate cloud with sufficient intensity, except in the case of thin cirrus. It is therefore difficult to obtain representative measurements of seasonal and synoptic relationships, since cloudiness is correlated with the synoptic pattern and thus with aerosol content. Nevertheless, the results that have been obtained in the present work can be interpreted in terms of the transport mechanisms in the lower stratosphere.

The ratio profile observed in the present work normally features a single and well-defined peak as shown in Figure 5.2, with a maximum at a height of 18 to 19 km. However, during the months from April to June, 1969, the character of the ratio profile became markedly disturbed, with the sporadic formation of a secondary upper peak at about 25 km. Sometimes the upper peak was more pronounced than the normal maximum, as shown in Figure 5.11(b). Inspection of Figure 5.11 shows that significant fluctuations in aerosol concentration can take place in a time interval of less than 24 hours, at least in the winter months. It is of interest to note the magnitude of the fluctuation observed in scattering ratio at 23 km from 26 to

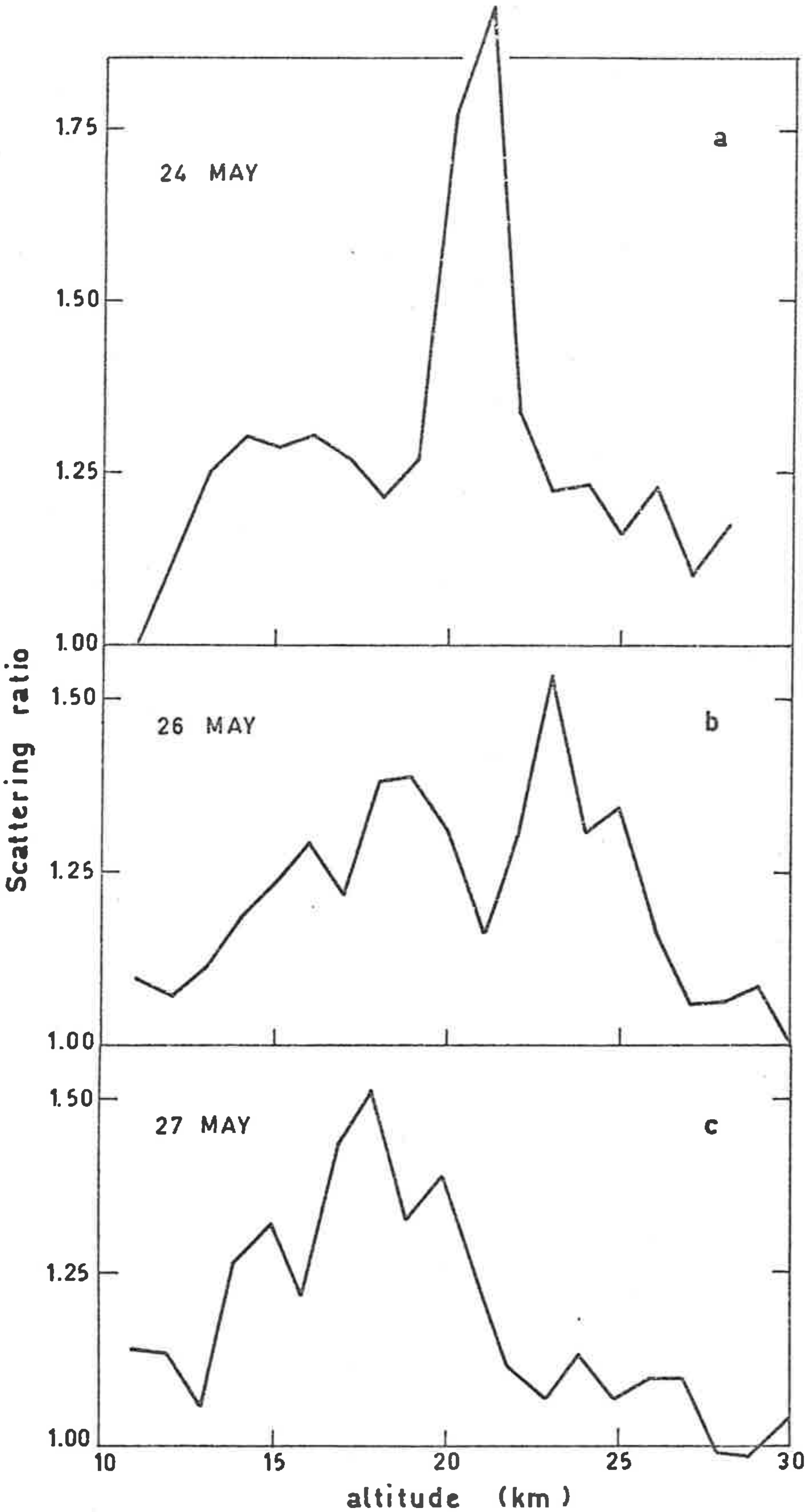

FIGURE 5.11 Changes in scattering ratio profiles in May, 1969.

27 May, 1969. The turbidity and hence number density during this particular period changed by the the factor 5:1. On the other hand the profiles in August, 1969, and January to March, 1970 are relatively stable, as is evident in Figure 5.12, which depicts three August profiles. This apparent seasonal effect in aerosol variability is more clearly shown by referring to Table 5.1, which lists cross-correlation coefficients for pairs of ratio profiles separated by a range of days, and for disturbed and undisturbed months. The cross-correlation coefficients for the disturbed group (April, May, 1969) are significantly less than those for the undisturbed group (January to March, 1970). The large time intervals over which the characteristics of the undisturbed group of ratio profiles still remain similar is particularly noteworthy. High cross-correlation coefficients are obtained for separations greater than 10 - 20 days. A similar seasonal effect in ozone variability has been noted by Kulkarni (1966). A statistical analysis of ozone results by Pittock (1968) has shown a significantly greater variation in the winter months than in the summer months. Pittock suggests that the high variability cannot result exclusively from a mean meridional transport mechanism, or from transport by standing eddies, unless one postulates similar variability in the ozone content at the source. The variability is therefore indicative of a significant seasonal fluctuation in the transport due to transient eddies.

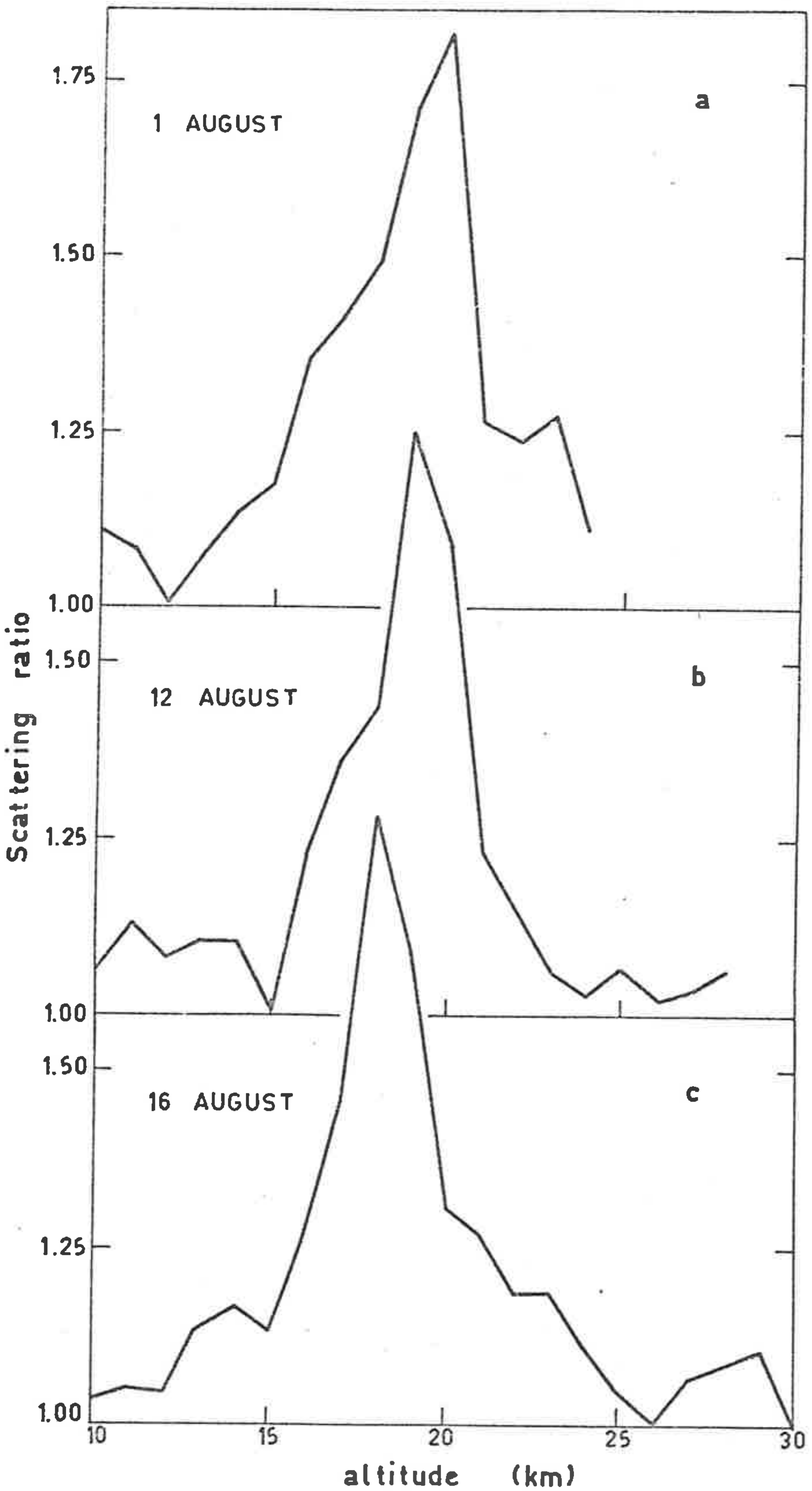

FIGURE 5.12 Changes in scattering ratio profiles in August, 1969.

TABLE 5.1

Group	Separation (Days)	Cross-correlation Coefficient
Disturbed (April, May, 1969)	1	.490
	1	.267
	1	.586
	2	.679
	2	.476
	2	.222
	8	.297
	9	.555
Undisturbed (Jan-Mar, 1970)	2	.782
	6	.880
	10	.883
	23	.805

An investigation was made of the relation between the upper level synoptic pattern at 200 mb, and the magnitudes of the scattering ratios measured with the laser radar. Although there are insufficient results at the present time to make a sound statistical analysis, the individual results, particularly for the autumn and winter months, are consistent with the trough-ridge hypothesis discussed previously. This will be demonstrated with two specific examples. The laser radar sounding on 15 April, 1969, measured ratios higher than the monthly mean values (Figure 5.13(a)). The peak ratio of 1.9 measured on 15 April represents more than a four-fold increase in optical turbidity, and presumably number density, over the monthly mean ratio of 1.25 at the same height. Inspection of the 200 mb synoptic charts shows that a low pressure trough had passed over South Australia at the time. In

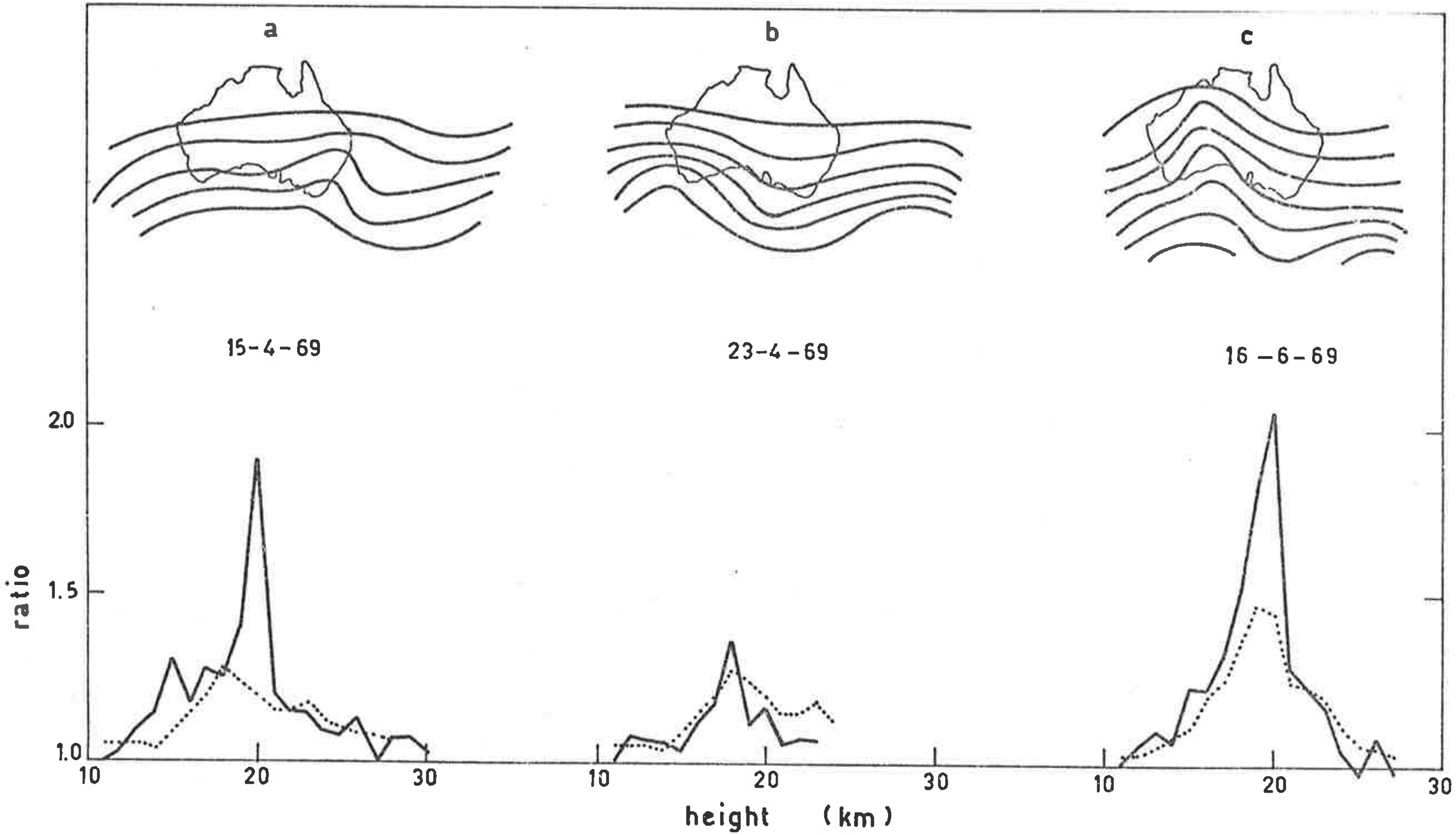

FIGURE 5.13 Illustration of the relation between features on the 200mb synoptic chart and fluctuations in aerosol scattering. Dashed curve; monthly mean ratio values.

Figure 5.13(a), the 200 mb chart for some 12 hours after the laser experiment is shown. The second period selected was when a ridge was travelling across southern Australia. In this case the ratios for 23 April, 1969, are less than the mean values for the month, except for the 18 km level, as shown in Figure 5.13(b).

It is of interest to consider the synoptic pattern for the day on which the highest ratio values were recorded in the present work. The peak ratio recorded on 16 June, 1969, was approximately 2.1, and as shown in Figure 5.13(c), a deep trough was situated to the west of the laser radar site. The occurrence of a maximum in aerosol concentration ahead of a trough is in agreement with the ozone results of Ohring and Muench (1960), and is predicted by the numerical model of Hunt and Manabe (1968). The maximum in aerosol scattering observed on 16 June, 1969, could also be attributed to the unusually large degree of curvature in the upper level flow pattern existing at the time. Experimental results of Ohring and Muench (1960) show a direct relationship between the degree of curvature in a trough or ridge and the magnitude of the deviation of ozone from the mean level.

The example of changes in scattering ratio cited above involve a large proportion of the total stratospheric aerosol layer. However, many of the fluctuations which occur over the space of a few days take place in a narrow height interval. Figure 5.11 shows that whereas the ratio at 21 km decreased significantly from 24 to 26 May, the ratio in the 23 km region increased. Similarly, the ratio at 23 km decreased from 26 to 27 May, while at the same time that in the 18 to 20 km region increased. These changes are shown more clearly in Figure 5.14 in which the ratios are averaged over the height intervals 18 to 20 km and 23 to 25 km. The corresponding temperatures and geopotential heights at the 70 and 30 mb pressure levels, obtained from local radiosonde flights, are also included. It can be seen that as in the case of the aerosol fluctuations, the changes in temperature at the two levels are not correlated, indicating that these levels are undergoing different meteorological processes. Figure 5.14 shows no significant correlation between the scattering ratio fluctuations and changes in the geopotential heights of the corresponding pressure levels, indicating that day to day fluctuations in aerosol scattering are more likely to be due to horizontal motions.

For comparison, Figure 5.15 is an example of the case when temperature and aerosol scattering fluctuations are taking place in unison at the 30 and 70 mb levels. The positive correlation between temperature and aerosol scattering changes which is evident in Figures 5.14 and 5.15 is a result of the biassed nature of optical measurements. As observations are limited to clear skies, the positions of the upper level synoptic patterns are biassed such that the trailing edge of troughs are favoured more than the centre or the leading edge. Consequently, high ratios are normally associated with the warmer air from higher latitudes. The fluctuations in geopotential heights of the two levels shown in Figure 5.15 bear no relation to the aerosol scattering changes, and are in support of the earlier conclusion that vertical motions are less important in affecting the day to day aerosol concentration.

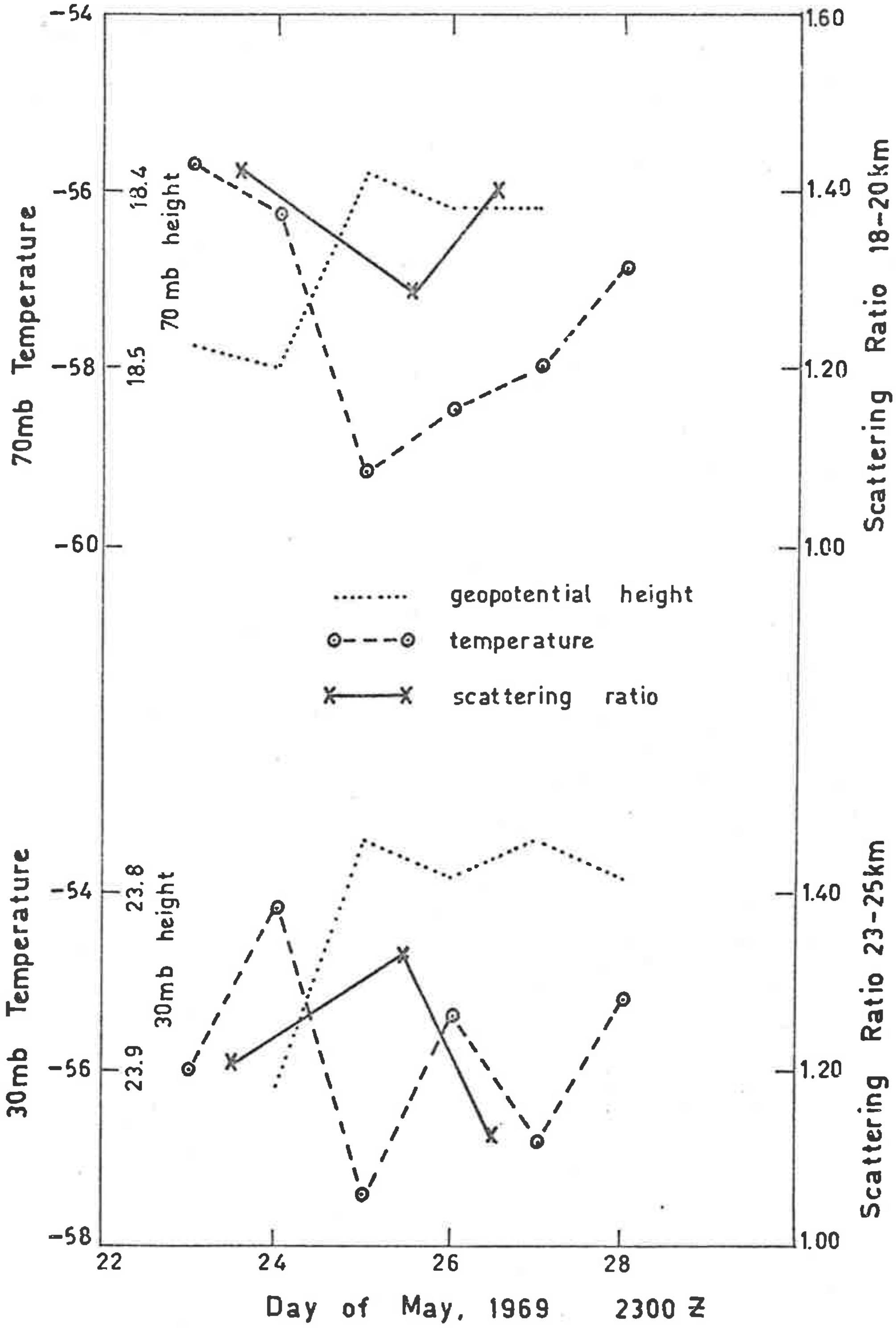

FIGURE 5.14 Changes in scattering ratio compared with fluctuations in temperature and geopotential height.

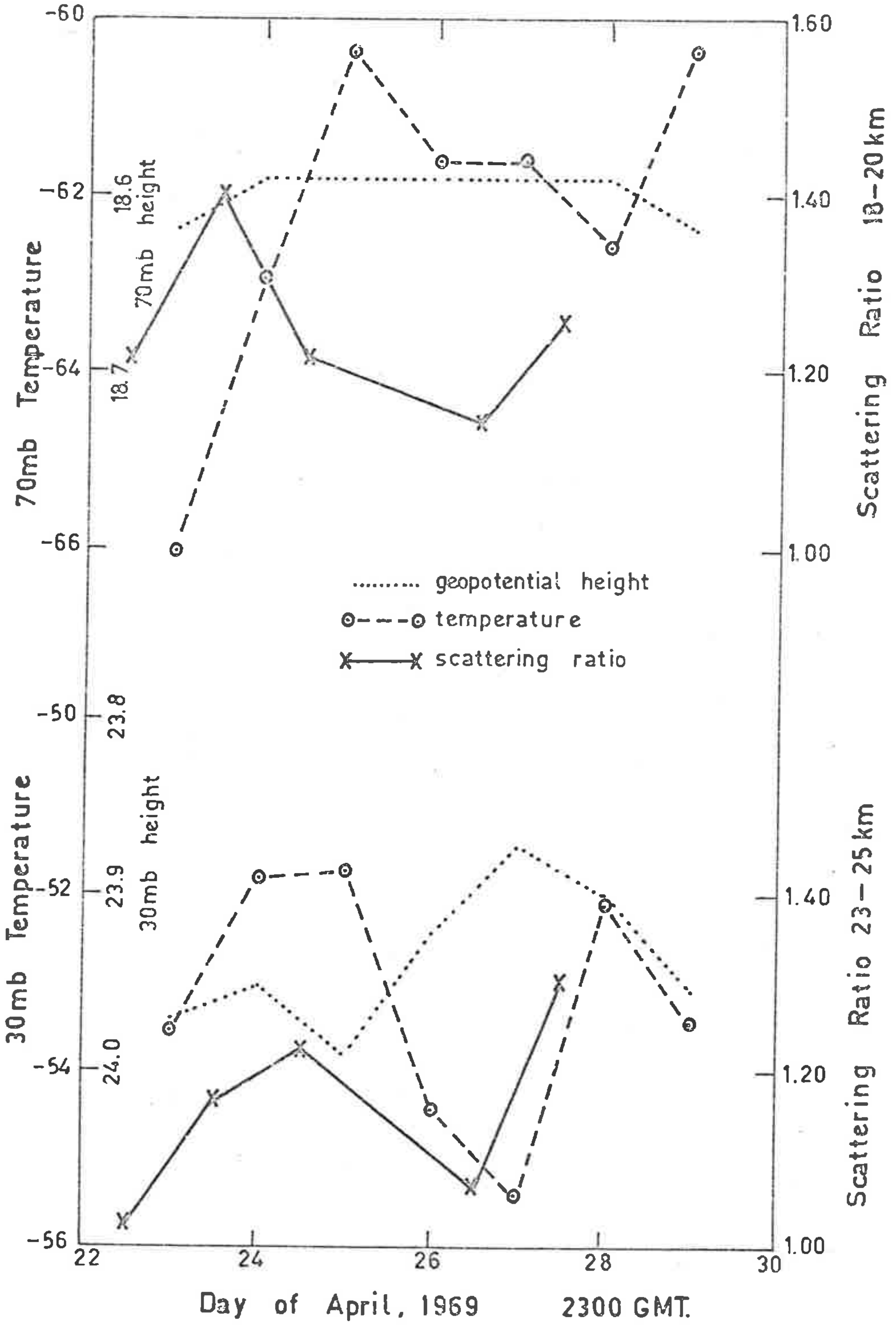

FIGURE 5.15 Changes in scattering ratio compared with fluctuations in temperature and geopotential height.

Although the mean height of maximum aerosol scattering in the stratosphere occurs between 18 and 19 km, high aerosol scattering is usually accompanied by a shift of the peak to greater altitudes. This is illustrated in Figures 5.11(a) and (b), and the tendency is also reflected in the monthly means for June and July when the maximum scattering ratios for the year were observed (Figure 5.7). It is of interest to consider the changes in the height of maximum aerosol scattering in the stratosphere which occurred in August, 1969, when the profiles had a tendency to be more stable (Figure 5.12). The tendency for ozone concentrations to be stable at this time of the year and at a similar location has been noted by Kulkarni (1966). It is likely that the tracers are more uniformly mixed. Figure 5.12 indicates a downward progression of the height of maximum aerosol scattering, from 20 km on 1 August to 18 km on 16 August. The higher altitude of maximum scattering at the beginning of the month is consistent with the features of the late June and July profiles, and is in agreement with the concept that the aerosols are being transported downwards from higher altitudes. The gradual downward progression of the peak in August is particularly noteworthy, as the upper level synoptic pattern changed considerably during the period. The results suggest a downwards progression of about 4 km per month, after which the height of peak aerosol scattering remained approximately constant. Radioactive debris measurements made by List et al (1966) at Mildura, South Australia, suggest a downwards propagation of about 1.5 km per month, and considering the limited data in the present work, the results are in fair agreement.

5.3 30 - 60 km Altitude Region

As the statistical errors for the results in the 40 - 60 km altitude region obtained on individual nights are significantly large, profiles were averaged over monthly periods. Four monthly mean ratio profiles for the 30 - 60 km region obtained in 1969 are presented in Figure 5.16. Monthly results were normalised at an altitude of 30 km, and the scattering indices were compared with theoretical values derived from the U.S. Standard Atmosphere, 1962, in order to deduce the scattering ratio. It can be seen that most of the departures of the experimental results from the Standard Atmosphere are not much greater than 1 standard deviation, and hence are statistically insignificant. The yearly scattering ratio profile shown in Figure 5.2 also shows no significant departure from the standard atmosphere in the 30 - 60 km altitude region.

The present results are in agreement with laser measurements made elsewhere (Bain and Sandford, 1966; Clemesha et al, 1967; Wright et al, 1969). Thus there is little evidence in support of a substantial aerosol layer at 40 km altitude as proposed by Dunkelman, Dave, Mateer and Evans (1968) in order to explain colours in the horizon sky observed by astronauts. However, using the present method of normalisation of the laser results, a constant background turbidity at all heights would remain undetected. Thus the proposal by Volz and Goody (1962) of a constant background turbidity of 0.2 remains in agreement with recent laser measurements.

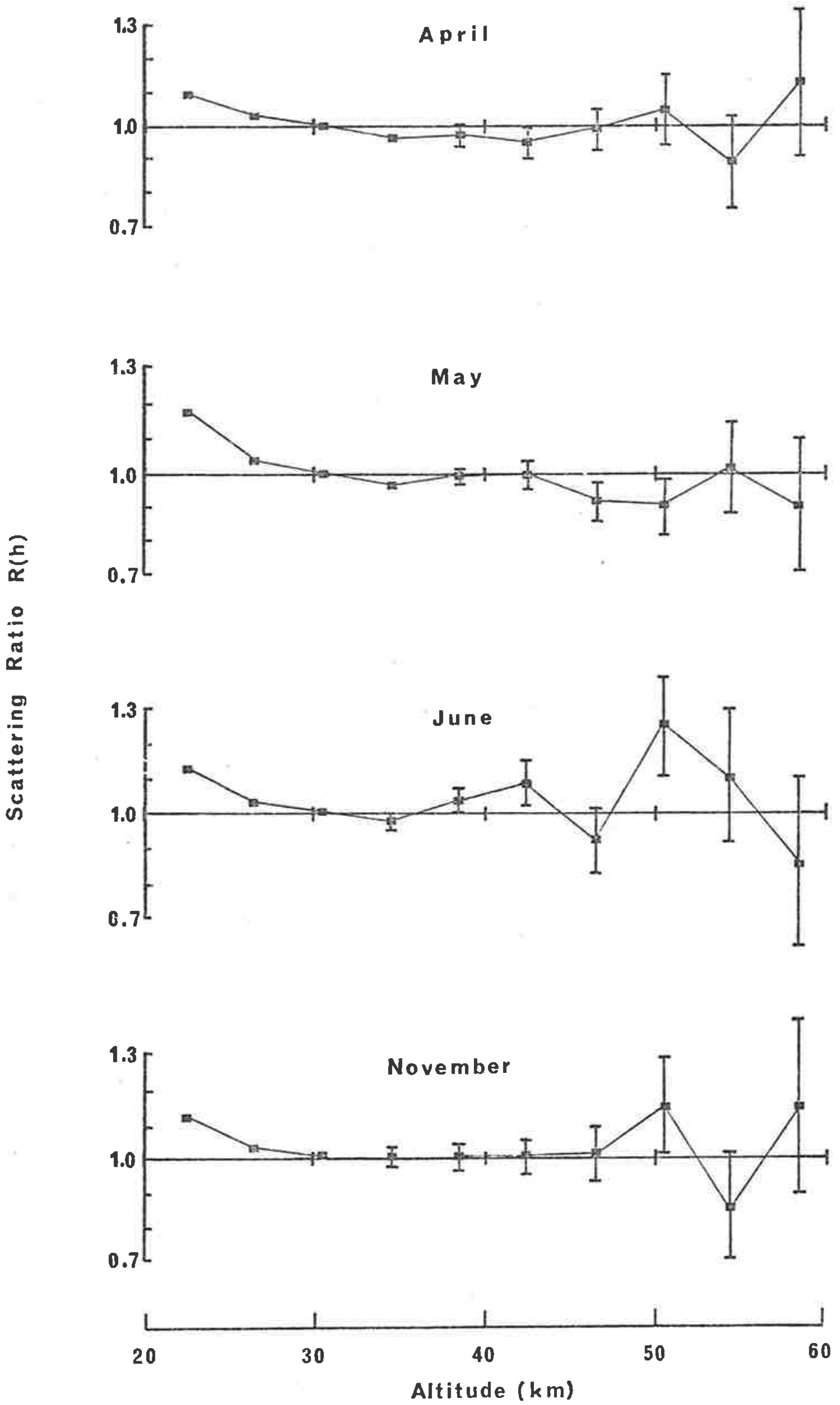

FIGURE 5.16 Mean monthly profiles of scattering ratio in the altitude region, 22-60 km.

It is of interest to note that the observations in the 30 - 60 km region for the winter of 1970 are different in one respect from the previous winter. Whereas the results for the winter of 1969 show an increase in aerosol concentration in the 18 - 20 km altitude region, the observations for the winter of 1970 show an additional significant increase in aerosol scattering in the 30 - 40 km region when an upper level trough is in the vicinity. Although this effect is to be expected on the basis of the transport mechanism in the stratosphere, it was not detected in the 1969 results. This would suggest that the source of aerosols at the equator was at a higher altitude in 1970 than in 1969.

CHAPTER SIX

TROPOSPHERIC OBSERVATIONS

In August 1969, the lower altitude capability of the laser radar was reduced from 10 km to 3 km by implementing the analogue recording apparatus, discussed in Chapter 2. In November 1969, this limit was further reduced to approximately 0.5 km when an adjustable diaphragm, which defines the field of view of the receiver, was incorporated in the equipment, enabling much wider fields of view to be attained.

The data analysis is described in detail in Chapter 4. Briefly, the experimental scattering index profile is normalised in the 9 - 10 km altitude region to a theoretical molecular profile calculated using local radiosonde data, and transmission corrections are made to the laser results using the method described in Section 4.3.2.

Figure 6.1 shows a number density profile from 3 to 7.5 km calculated from the average laser results for the period from August to December, 1969. The laser results were converted to number densities using equation 3.13. As noted in Chapter 1, measurements of the size distribution of aerosols by various observers in the mid-to-upper troposphere are not in agreement. However, the relative magnitudes of Aitken and large particle number densities in this height region are indicative of a Junge power law, with an exponent ν of approximately 2 to 2.5. It is of interest to note that the measurements of Junge et al (1969) are in agreement with the above size distribution. Accordingly, the present calculations are based on a Junge

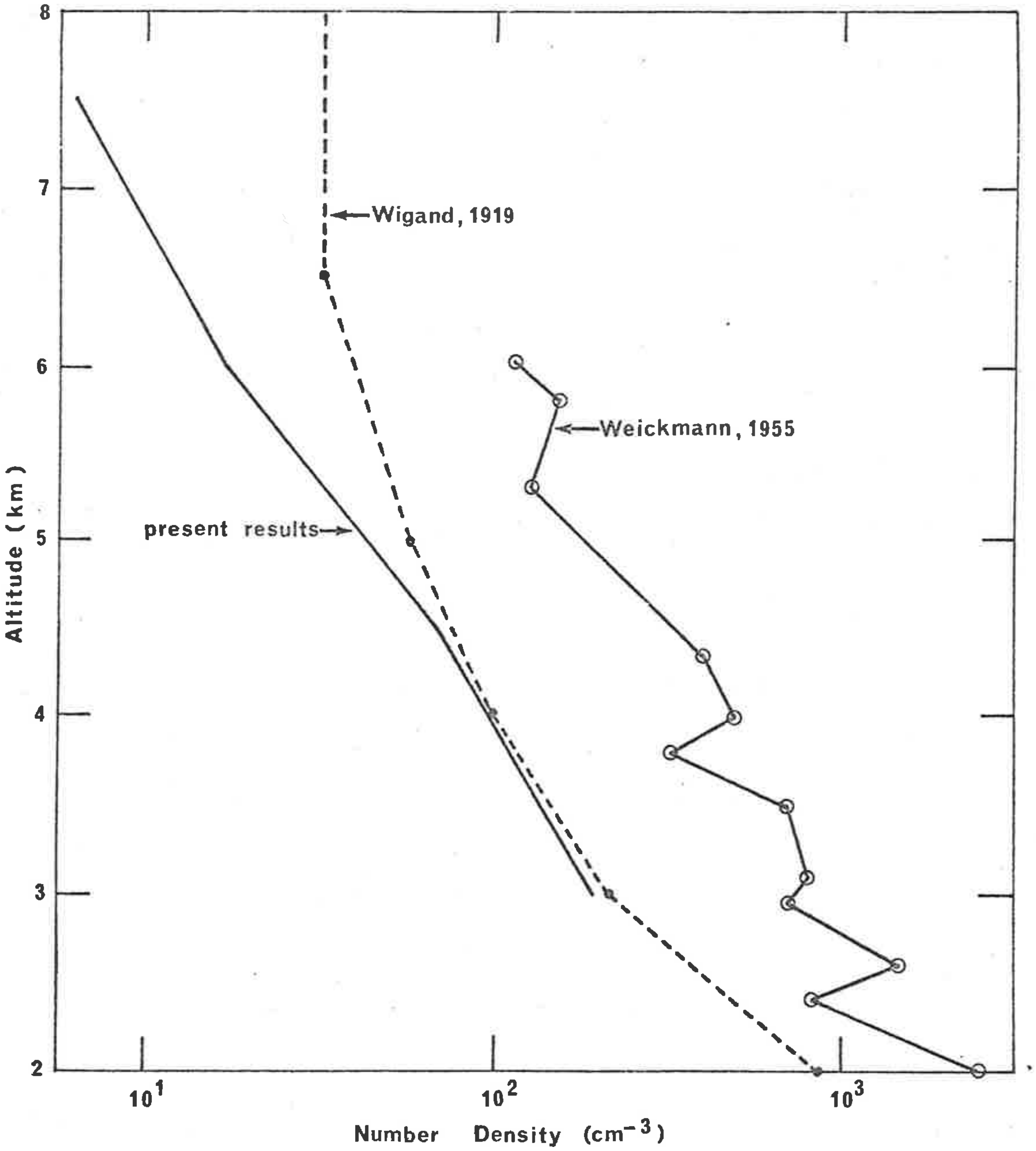

FIGURE 6.1 Comparison of number densities calculated from the laser results and Aitken nuclei concentrations.

size distribution, constant with height, with $\nu = 2.5$ and a lower cut-off radius of 0.04 μ. As the particles have a significant solid component, a refractive index of 1.5 is assumed. Considerations in Chapter 3 indicate that Aitken nuclei determine the optical characteristics of tropospheric aerosols, and the present results are compared with the Aitken nuclei measurements of Wigand (1919) and Weickmann (1955). It can be seen that the results are in good agreement, confirming the original deduction of the importance of Aitken nuclei in the troposphere. The number densities calculated using a Junge size distribution with $\nu = 2$ are approximately a factor of 3 smaller than those calculated assuming $\nu = 2.5$, and hence are not in good agreement with observed Aitken concentrations.

6.1 General Characteristics of the Scattering Ratio Profiles

The tropospheric ratio profiles above 0.5 km measured from November 1969 to May 1970 can be grouped into three typical classes, and are determined by the prevailing meteorological conditions. These are shown in Figures 6.2 and 6.3.

Figure 6.2(a) shows the ratio profile obtained in more than 70% of the measurements, which are observed when the air mass originates from the Southern Ocean. The relative humidity profile, and the corresponding ground level synoptic chart for the measurement period are also included. This group is characterised by at least one significant peak in the altitude region below 2 km, which is strongly correlated with features on the corresponding relative humidity profile. This would indicate that the maritime air mass from the south is rich in hygroscopic aerosols. The

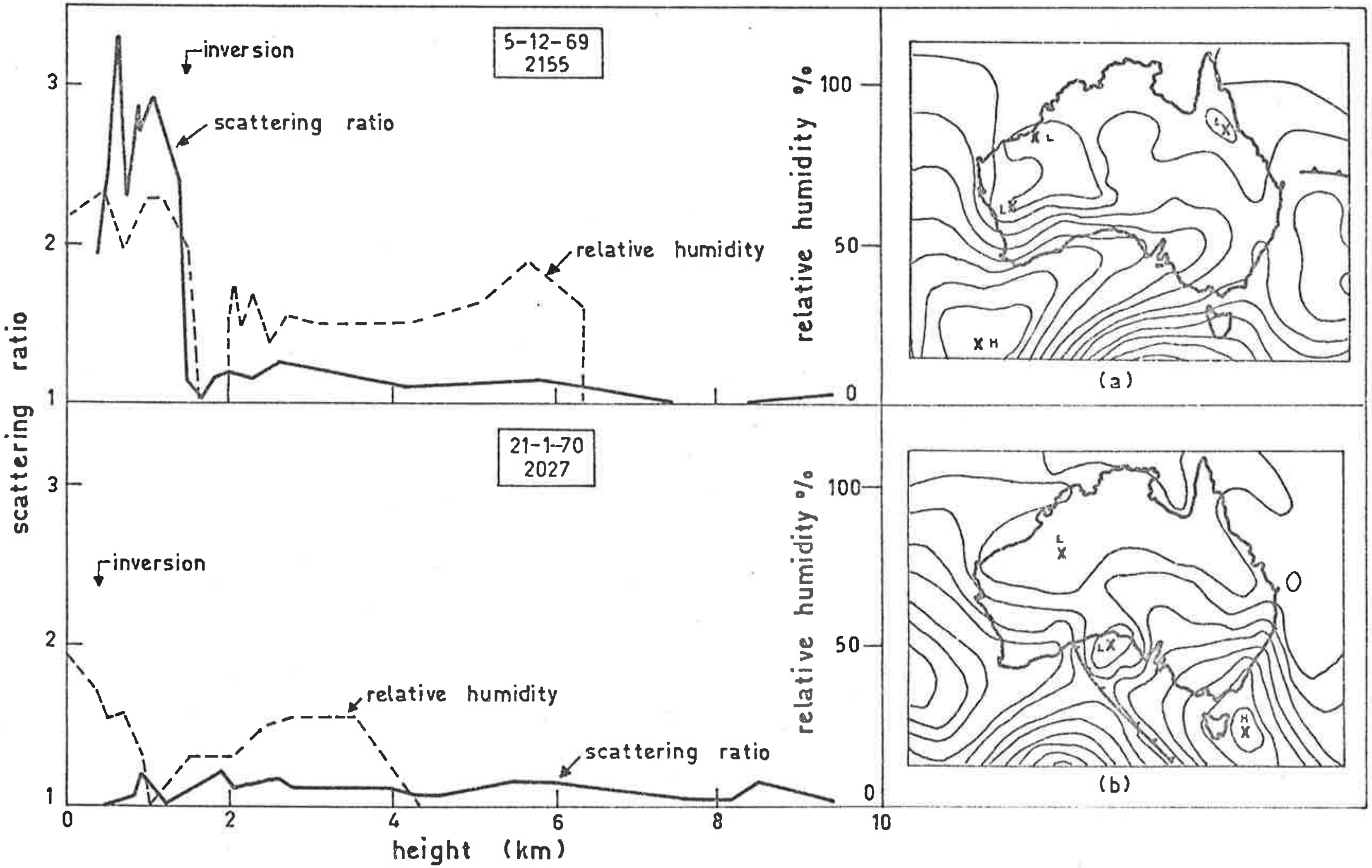

FIGURE 6.2 Two types of scattering ratio profiles observed in the troposphere, and the corresponding meteorological parameters.

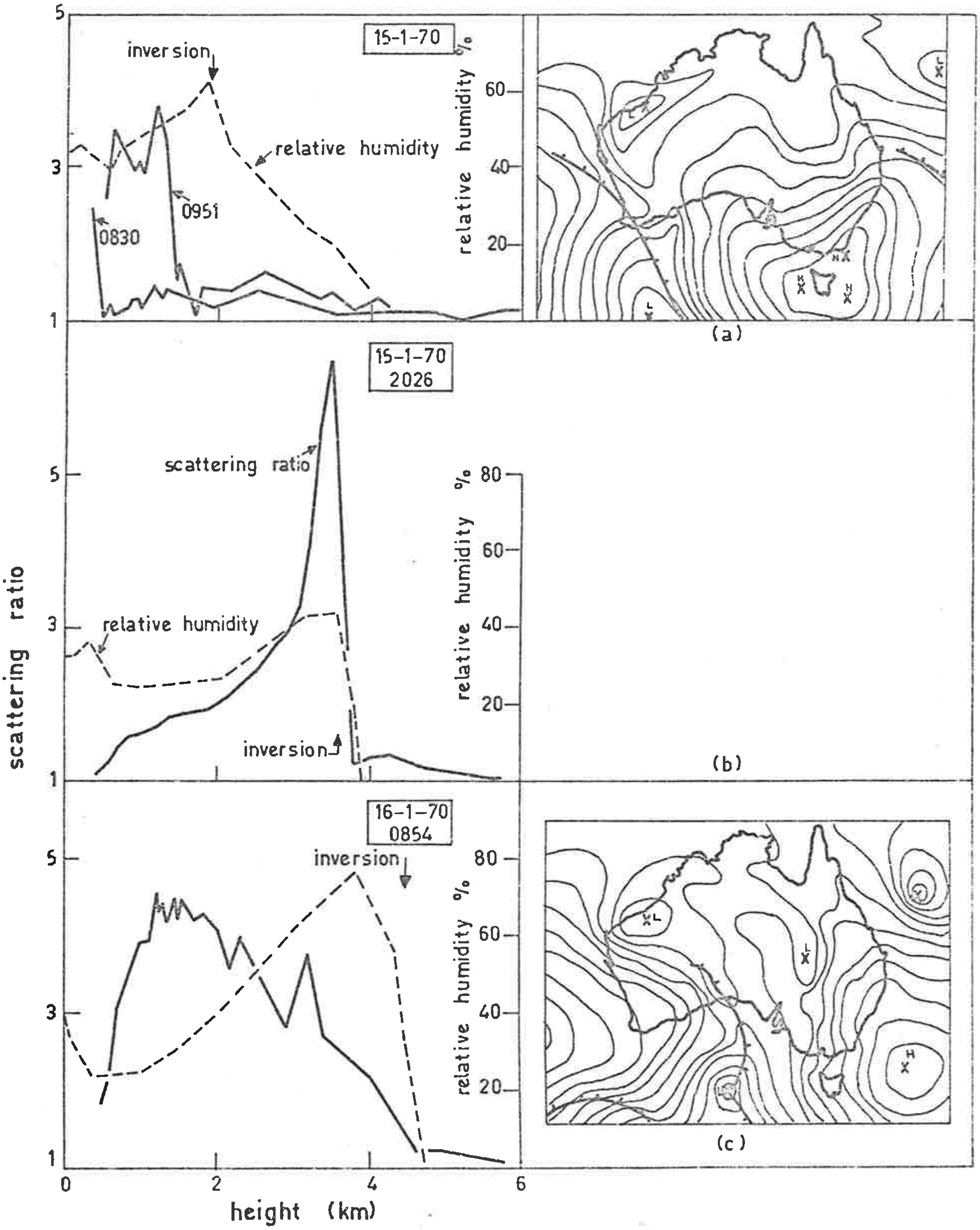

FIGURE 6.3 Changes observed in the scattering ratio profile and corresponding meteorological parameters during 15-16th January, 1970.

upper limit of the aerosol layer is nearly always bounded by a temperature inversion, which prevents very effectively any upward motion of the air mass by convection. The characteristics of this layer are in close agreement with the earlier measurements by Twomey (1955) in a similar locality, and under the same meteorological conditions. Twomey collected giant particles near Mt. Gambier, South Australia, in air of maritime origin up to altitudes of 2.5 km, and found them to be predominantly sea salt. The upper altitude limit of these particles was also limited by a temperature inversion, and often corresponded to the base of scattered cumulus cloud. It is of interest to note that the relative humidities in these aerosol layers are usually much less than the humidities necessary for the transition of hygroscopic particles from solid to liquid phase (> 70%). This could be indicative of a considerable degree of supersaturation, as discussed previously in Chapter 1. On the other hand, as the size distribution of these aerosols is likely to be described by a Junge power law, the particles in the Aitken size range would determine the characteristics of the scattered signal. The greater curvature of these droplets would thus tend to lower the humidities at which phase transition occurs (Junge, 1963).

The ratio values immediately above the height of the main aerosol layer are typically 1.2 - 1.4, and a slow reduction in ratio occurs with a further increase in altitude until about 6 km, above which the ratio is apparently constant, at least within the accuracy of the present experiments. The ratio profile above the height of the main peak is correlated to a lesser degree with the temperature and relative humidity curves, although in some instances, as in the example shown in Figure 6.2(a), a general agreement still persists.

The occurrence of the optically thick aerosol layer almost exclusively below 2 km when the air mass is of maritime origin is in agreement with the results of Junge et al (1969). They found that the sea spray component which was detected in aerosols 65 m above sea level at Cape Blanco, was not found at an altitude of 2200 m at Crater Lake National Park. This gives further support to the suggestion that the aerosol layer frequently detected in the present work consists predominantly of hygroscopic particles. The measurements of Junge et al indicate that the size distribution of these particles can be approximated by a Junge power law with an exponent ν of 2.

The second type of ratio profile is shown in Figure 6.2(b), together with the relative humidity profile and the corresponding ground level synoptic chart. This ratio profile is detected in about 20% of the measurements and when the wind has a northerly and hence continental component. The characteristics of this group is the very low ratio values at all heights. In contrast to the maritime ratio profiles, which often have peak values greater than 2 and sometimes exceeding 6, the continental ratio profiles typically range from 1.2 to 1.4, representing more than a 5 to 1 reduction in turbidity. This is contrary to what one might expect from considerations of particle concentrations over land and sea. The results of Landsberg (1938) in Table 1.1 suggest that continental number densities are approximately 10 times greater than maritime concentrations. This, coupled with the strong convection that occurs in the warm conditions accompanying a northerly air stream, would tend to increase the particle number density in the 0 - 2 km region.

The size distributions of maritime and continental aerosols could, however, be substantially different. Considerations in Chapter 1 indicate that although the size distributions of both types of particles can be described by the Junge power law, the exponent ν of the low level maritime aerosols is approximately 2, while that of continental aerosols lies between 3 and 4. Referring to Table 3.1, it can be seen that the scattering cross-section for aerosols with a Junge size distribution and $\nu = 2$ is a factor of 10 greater than the cross-section for particles with $\nu = 3$. Thus it is feasible that the difference in scattering ratio profiles of continental and maritime aerosols measured in the present work is primarily due to the difference in size distributions, as a consequence of the effects of humidity.

The third class of ratio profile observed is illustrated in Figure 6.3(b) and (c), and occurs less frequently than the other types. The notable characteristic of this profile is a broad, optically dense aerosol layer in the region from ground level to about 4 km. The upper boundary of the aerosol layer corresponds to the presence of either an isothermal layer or temperature inversion, together with a sharp cut-off in humidity. Above this height level, the air is warm and dry. The ground level synoptic chart indicates a northerly air flow, similar to the synoptic pattern accompanying the previous type of ratio profile.

These aerosols are believed to be hygroscopic, as the layer corresponds to the region of maximum humidity. The growth of the aerosol layer is illustrated in Figure 6.3. The observation at 0830 hrs on 15 January was taken at the same time as the radiosonde measurements, and shows a broad and weak aerosol layer between 0.5 and 4 km, which coincides with the peak in relative humidity. It is of interest to note that the temperature inversion at 2 km hardly affected the distribution of aerosols. The record at 0951 hrs on the same day shows aerosol layers at 1 and 2.7 km, which developed into a single, optically thick layer by 2026 hours. During this time interval, the height of the inversion increased by more than 1 km, as also did the upper regions of the humidity layer. This increasing trend in the height of the temperature inversion, and the upper boundaries of the aerosol and humidity layers, is still evident in the observations on the morning of the 16th January. By the evening of the 16th January, a cold front had approached, and no further observations were made.

The origin of this hygroscopic aerosol layer is not immediately obvious from considerations of the synoptic chart. However, as these characteristics were only observed in the summer months of December and January, it is possible that the moist air mass is of tropical origin.

The above considerations indicate that aerosol layers can originate due to the trapping action of temperature inversions, and that their effects can be enhanced by the presence of water vapour. The trapping effect of a temperature inversion is often noticeable in urban and industrial areas, an example of which is shown in Figure 6.4. The restriction of the upwards convection of the smoke plume (left of centre) is particularly noticeable. Frequently, however, minor aerosol layers detected by the laser radar bear no relation to either the temperature or relative humidity profiles, as illustrated in Figures 6.3(a), (b) and (c). It is possible that the radiosonde data are not sufficiently accurate for the detection of small fluctuations in either the temperature or the relative humidity. On the other hand in some instances, significant fluctuations in the temperature and relative humidity profiles are not accompanied by changes in the scattering ratio profile.

6.2 Rapid Fluctuations in Aerosol Scattering

Frequently, rapid fluctuations are observed in the signal scattered from low levels when the air mass originates from the Southern Ocean. The regions in which fluctuations take place correspond to humidity layers detected by the radiosonde equipment. Significant fluctuations can take place in time intervals of a few seconds.

An example of the nature of these fluctuations is shown in Figure 6.5, which is a sequence of oscilloscope traces between 2129 hrs and 2152 hrs on 5 December, 1969. The time interval between traces ranges from 1 to 5 minutes. The corresponding humidity profile may be seen by referring to Figure 6.2(a), which indicates that the fluctuations in aerosol scattering are taking place within the humidity layer which extends from ground level to 1.6 km. The sharp change in slope of the oscilloscope traces at 1.6 km corresponds to the temperature inversion.

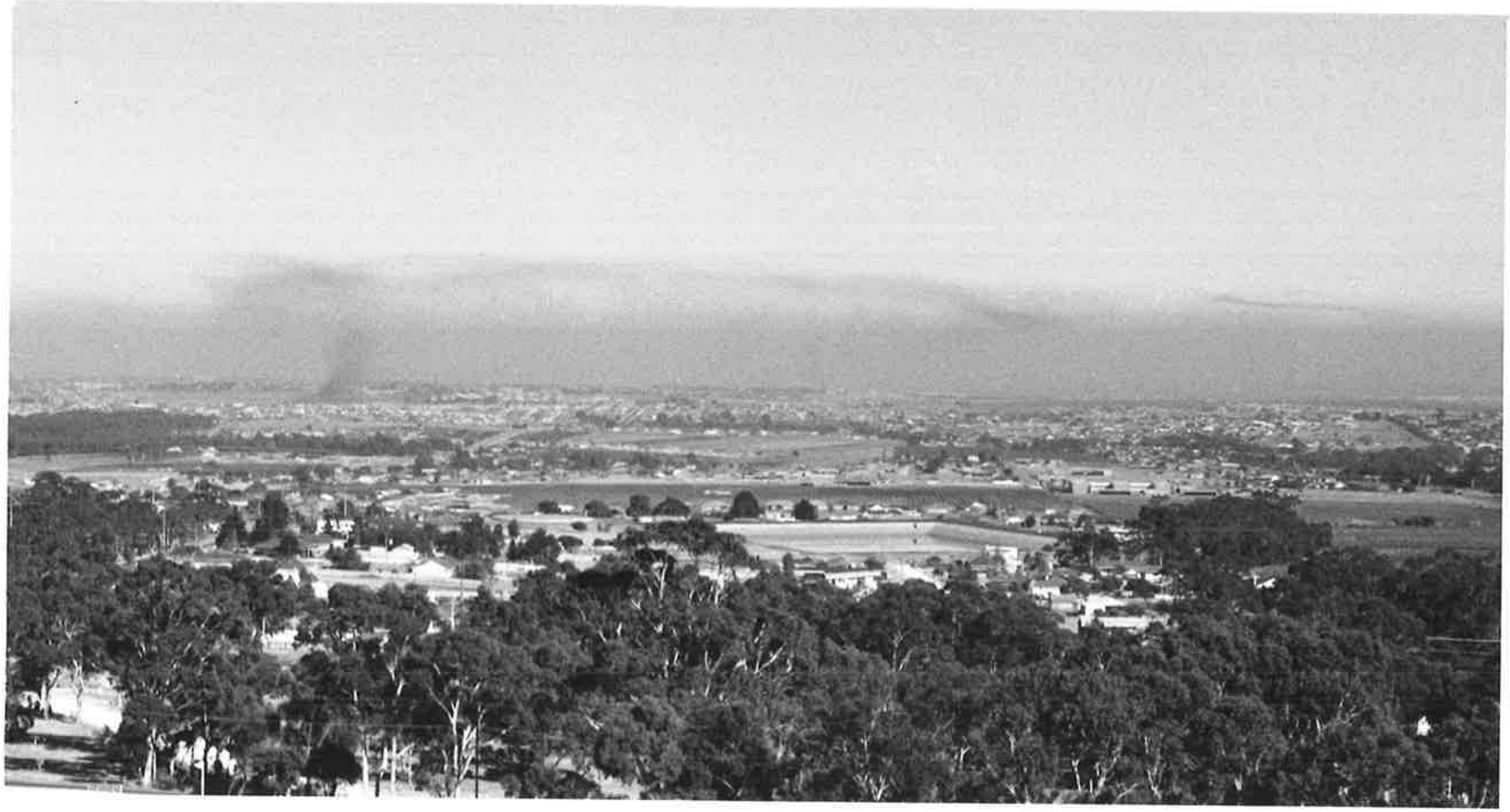

FIGURE 6.4 Illustration of the trapping effect of a temperature inversion.

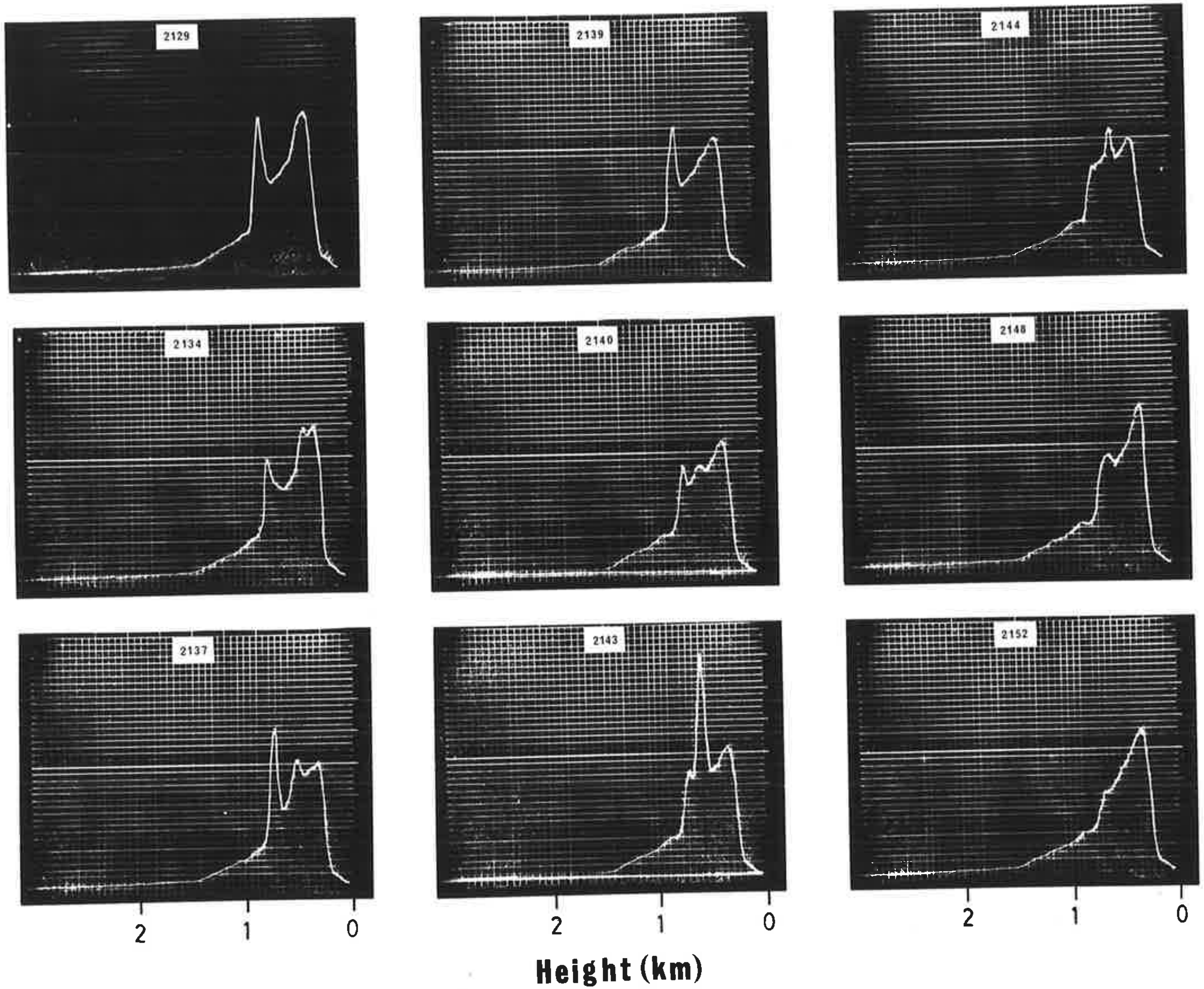

FIGURE 6.5 Illustration of rapid fluctuations observed in aerosol scattering in the lower troposphere.

It is possible that the fluctuations in aerosol scattering described above are due to rapid changes in the relative humidity. It thus follows that the direct sampling technique by means of a limited number of radiosonde observations could be subject to significant errors.

The fluctuations in aerosol scattering described above occurred in an apparently clear sky. An investigation was made of the characteristics of aerosol scattering which occur in the clear region between cumulus clouds. Rapid fluctuations were again observed, with a tendency for the signal scattered from cloud height to increase as a cloud approached the field of view. This effect is illustrated in Figure 6.6. In order to simplify the calculations, the scattered signal is presented in terms of the scattering index I(h) without transmission corrections. It can be seen that the scattering index measured at 1326 and 1332 hrs, corresponding to cases when the cloud was very close to the field of view of the receiver, is significantly greater than I(h) measured at the remaining times, when the cloud was further away.

6.3 Diurnal Variations

The diurnal variation in aerosol scattering observed with a laser radar has already been presented qualitatively by Viezee and Oblanas (1969). Their results show an increase in aerosol scattering from morning to noon due to the effects of convection.

The present results cover a period of more than 24 hours in a typical summer's day, and data are presented in terms of the scattering ratio Figure 6.7 shows scattering ratio profiles measured from 1530 hrs on

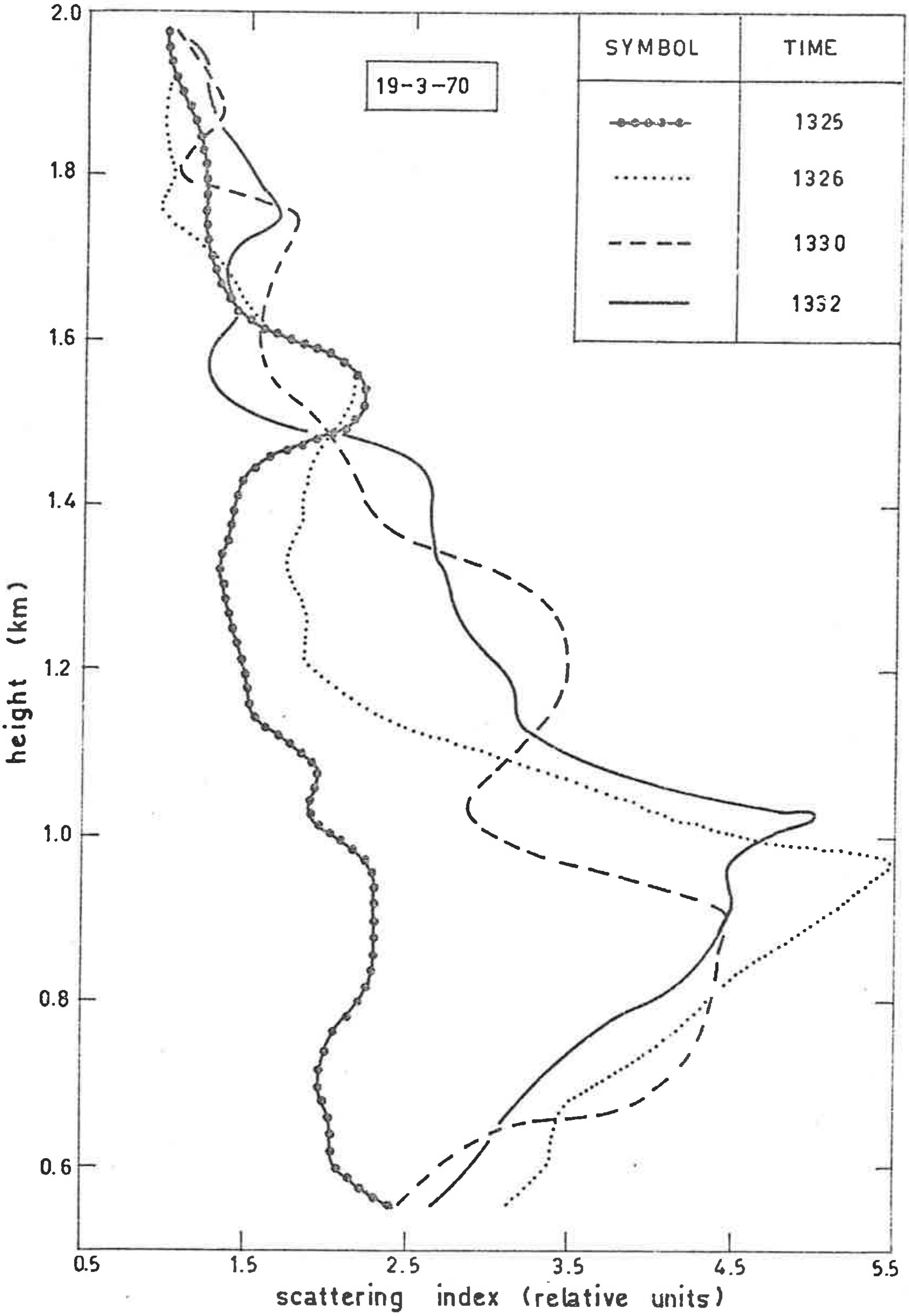

FIGURE 6.6 Fluctuations in scattering index observed between cumulus clouds.

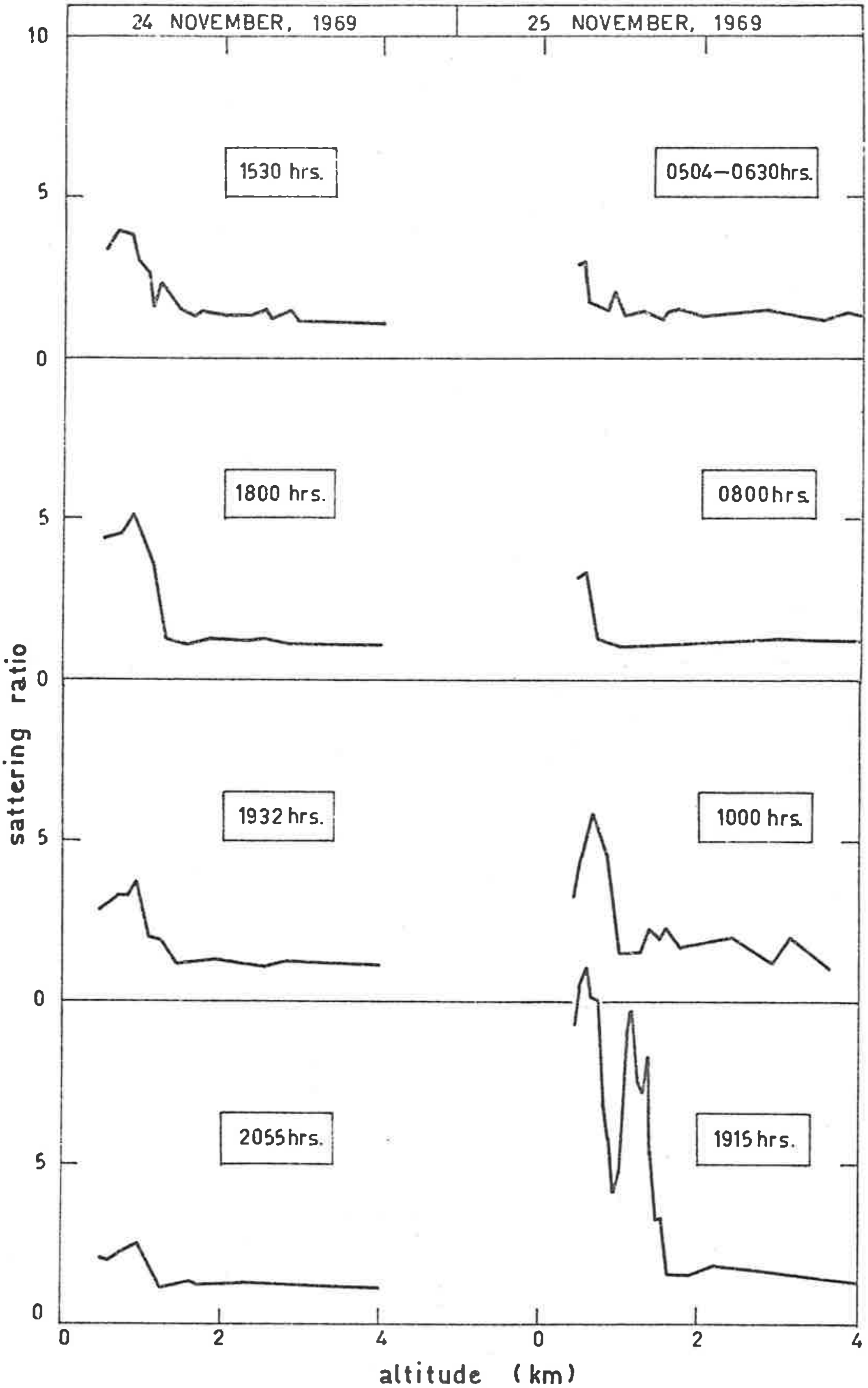

FIGURE 6.7 Diurnal variation of scattering ratio of tropospheric aerosols observed on 24-25th November, 1969.

24 November to 1915 hrs on 25 November, 1969. The results indicate that the optical turbidity of the low level aerosol layer is greatest in late afternoon. By 0504 hrs on 25 November, the layer had nearly vanished. However, by 0630 hrs, the effects of solar heating were already becoming evident, and the turbidity of the lower levels increased throughout the day. On 25 November, there was also a tendency for the upper boundary of the aerosol layer to steadily increase throughout the day. This effect has been noted by Naito et al (1968), and is due to the extent of heating that takes place at the earth's surface. Apparently, the air ascends dry-adiabatically, and stops at a level where a dry-adiabatic line starting from the surface temperature intersects the environmental temperature profile. As the convection activity is greatest when the maximum surface temperature occurs during mid-afternoon, it follows that the maximum height of the aerosol layer is greatest in the late afternoon.

6.4 Observations of Cirrus Cloud

On 1 June, 1970, observations were made of cirrus cloud preceding a cold front. The cloud, which was at an altitude of approximately 8 km, was almost undetectable against the star background. Due to its height and horizontal extent, the cloud was identified as either cirrostratus or cirrocumulus.

Two sequences of observations are shown in Figure 6.8. The traces were taken 30 seconds apart, and each trace was repositioned in the vertical direction to prevent overlapping. Figure 6.8(a) shows the

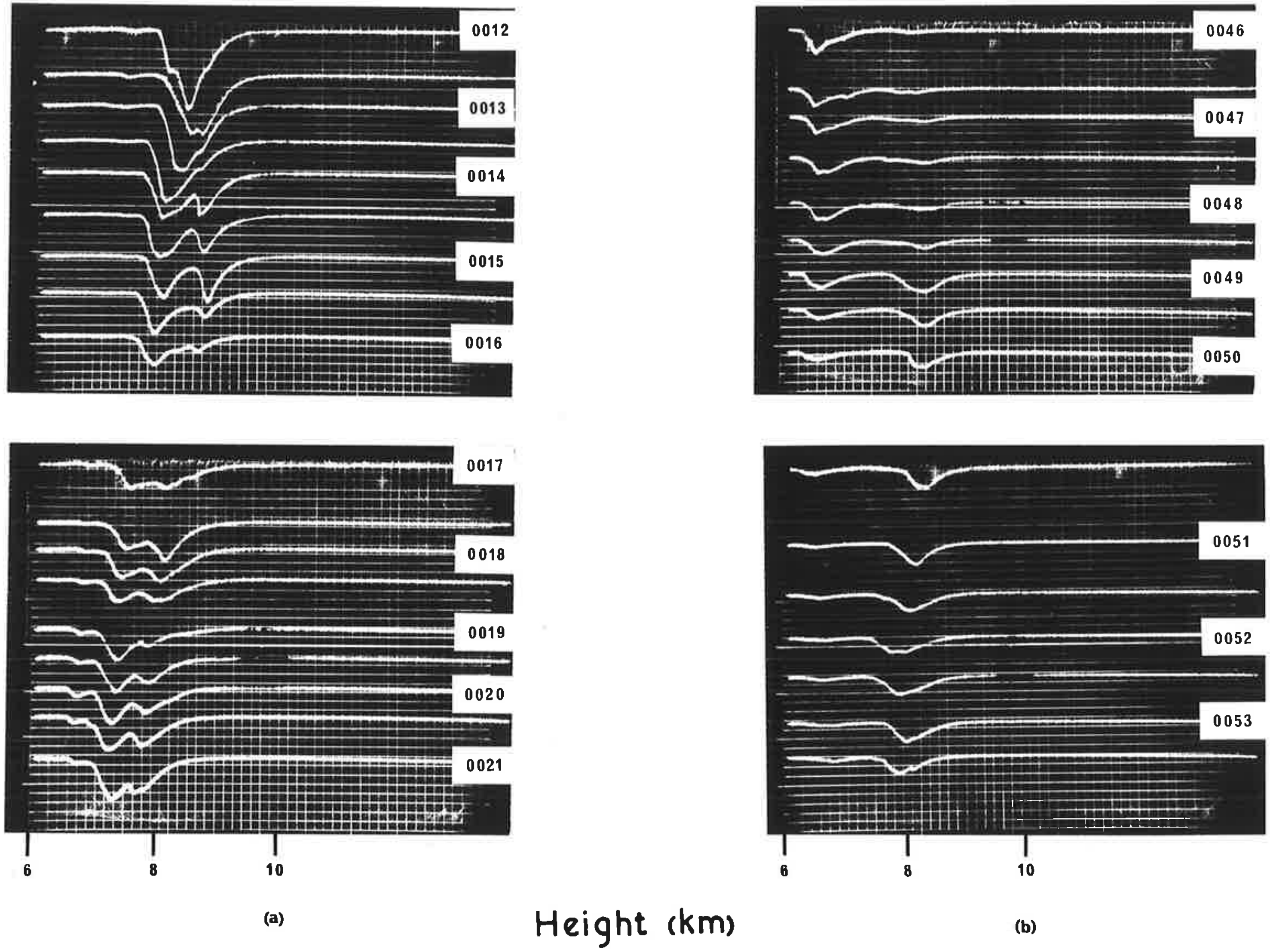

FIGURE 6.8 Observations of cirrus cloud on 1st June, 1970.

sequence of observations between 0012 hrs and 0020.5 hrs, indicating a tendency for the cloud structure to be bifurcated. Two further points are of interest. There is a general apparent downwards propagation of the cloud, amounting to about 800 m in the 8.5 minutes of observation. It is clear that this phenomenon could also be a result of the horizontal motion of a cloud sheet inclined to the horizontal. Superimposed on the mean apparent downwards motion is a slight oscillating trend. This could be due to oscillations in the cloud sheet itself, or due to the patchy nature of cirrocumulus type cloud.

The sequence of observations shown in Figure 6.8(b) are some 26 minutes later than the first sequence. By this time the cloud had apparently descended nearly 2 km, and the intensity was greatly reduced. The records show that this cloud eventually disappeared, to be replaced by another cloud sheet at the original height. As in the example shown in Figure 6.8(a), the cloud has a mean downwards motion, superimposed on which is a slight oscillation.

CHAPTER SEVEN

SOME ASPECTS OF THE TWILIGHT PHENOMENON

Of the three optical probing techniques discussed in Chapter 1, the twilight experiment has been most frequently used, due principally to the modest equipment that is required. Yet interpretation of the results, particularly for the lower atmosphere where aerosol scattering is of significance, has proved to be extremely difficult, due to the interrelation between the transmission and scattering characteristics of the atmosphere in this region (Rozenberg, 1966).

The present twilight experiments were initiated prior to the completion of the laser radar equipment, when it became evident that dust from the Mt. Taal (14°N, 121°E) eruption on 28th September, 1965, might provide an opportunity to study large scale circulation in the lower stratosphere. Although largely criticised by several workers (e.g. Volz and Goody, 1962; Rozenberg, 1966) the twilight gradient approach of Bigg (1956, 1964) was adopted. This technique has the advantage of simplicity and the method is outlined as follows. For a fixed elevation of the line of sight, the height of the earth's shadow boundary appears to increase as the sun sets further below the horizon. Bigg (1964) showed that for the case of a pure molecular atmosphere, the rate of change of brightness of the twilight sky with height of the shadow boundary (dI/dh) is related to the scale height H of the molecular atmosphere by the following relation;

$$-\frac{1}{I}\frac{dI}{dh} = \frac{1}{H} \qquad (7.1)$$

The left hand side of equation 7.1 is just $-\,d(\ln I)/dh$ and the variation with h is known as the twilight gradient. Bigg showed that a thin aerosol layer adds a contribution to the pure molecular term 1/H in equation 7.1. Later calculations will show that this is true also for the case of the broad stratospheric aerosol layer. As solar radiation grazing the earth is attenuated more than that passing higher up, the shadow boundary is not sharp, and the measured twilight gradient is smoothed. The extent of this smoothing has been the subject of controversy for a number of years. Bigg (1964) claims to have detected narrow layers in the stratosphere by virtue of the sharp discontinuity in the shadow boundary. These "layers" appeared to be well correlated with discontinuities in the corresponding temperature profile. On the other hand, extensive calculations of model atmospheres by Volz and Goody (1962) indicate that the shadow boundary is several kilometers thick, thus averaging out thin layers such as those claimed to have been detected by Bigg. Megrelishvili (1958) correctly suggests that the mean height of the twilight ray, frequently called the "screening height", should be used in place of the sharp shadow edge. However, it will be shown later that Megrelishvili's estimate of 20 km for the screening height is grossly in excess of values deduced in the present work, and by Volz and Goody (1962).

There is little doubt that the broad peak in the twilight gradient is primarily due to the presence of the stratospheric aerosol layer. The increase in stratospheric dust brought about by the Bali eruption in 1963 is clearly shown as an increase in the twilight gradient in the results of Volz (1969). Typical intensities and corresponding twilight gradients for a relatively clear and a turbid stratosphere observed by Volz (private communication, 1969) are shown in Figure 7.1. It can be seen that an increase in aerosol concentration in the lower stratosphere results in an increase in the brightness of the twilight sky, which is reflected in a decrease in the twilight gradient at small solar depressions, and an increase in the twilight gradient at larger solar depressions. However, scattering coefficients can only be deduced by the measurement of absolute intensities (Volz and Goody, 1962).

The construction of the laser radar at Adelaide has afforded an excellent means of comparing the twilight results with the results of an independent experiment. In the following pages, the twilight experiments conducted at Adelaide are reviewed, and the comparison with the laser radar results is discussed.

7.1 Experimental Aspects

Light gathered from a 0.5 degree field of view by a 15 cm diameter Cassegrain telescope is recollimated, and passed through a Wratten No. 29 red filter to an EMI 9558B photomultiplier. The combined response of the filter and photocathode extends from 6200 Å to about 8000 Å. The output from the photomultiplier is amplified by a D.C. amplifier, the output of which is maintained within the range 3.0 to 3.1 volts by step-wise adjustment of the E.H.T. voltage, and hence the gain, of the

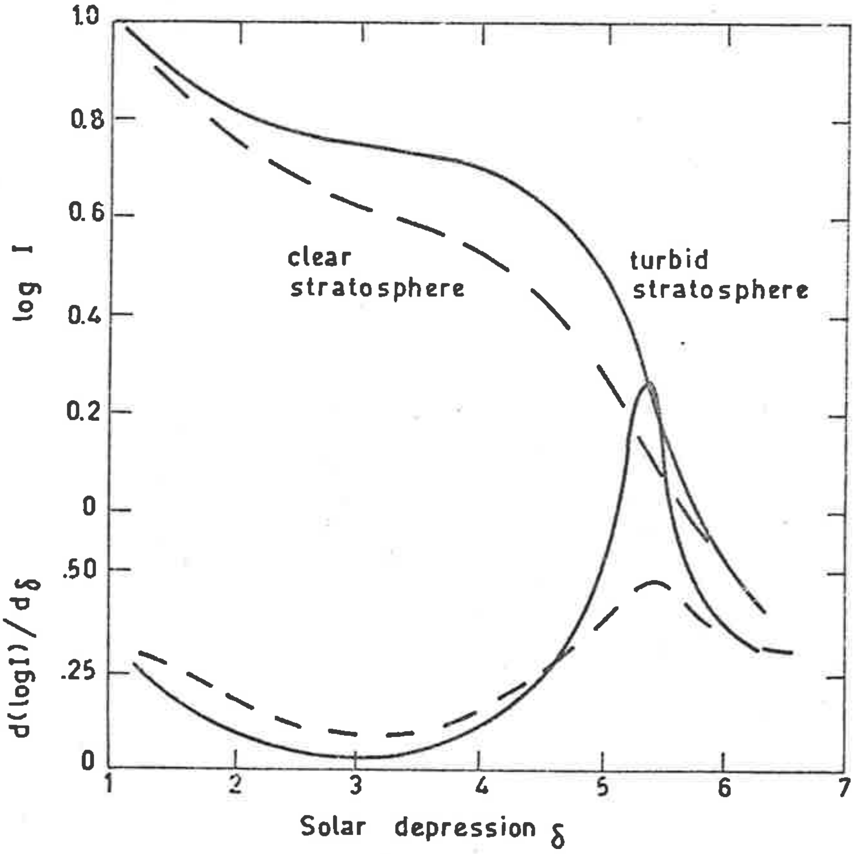

FIGURE 7.1 Schematic diagram of intensities and corresponding gradients for a relatively clear and a turbid atmosphere.

photomultiplier. A fast response pen recorder with 0.1 volt full scale sensitivity is placed between this varying output and a fixed potential of 3.0 volts. Whenever the pen recorder reaches the limit of its deflection, the gain of the photomultiplier is adjusted to bring the trace back to the other end of the scale.

Under these conditions we may write AI = kV, where I is the light intensity incident on the photomultiplier, A is the instantaneous amplification of the system, and V is the output voltage of the amplifier. Thus $A \frac{dI}{dt} = k \frac{dV}{dt}$, and we obtain

$$\frac{1}{I}\frac{dI}{dt} = \frac{1}{V}\frac{dV}{dt} \qquad (7.2)$$

Since V is approximately constant, being maintained within the range 3.0 to 3.1 volts, $\frac{1}{I}\frac{dI}{dt}$ is proportional to $\frac{dV}{dt}$, which is simply the slope of the pen recorder trace. Thus from (7.1),

$$\frac{1}{H} = -\frac{1}{I}\frac{dI}{dh} = -\frac{1}{V}\frac{dV}{dt}\frac{dt}{dh} \qquad (7.3)$$

The apparatus was originally located at St. Kilda, some 17 miles north of Adelaide, at latitude 34° 43' south and longitude 138° 34' east, and observations were begun in October, 1965. Precautions were taken to avoid twilights which were affected by distant clouds. The local weather map was inspected prior to each run, and cloud reports from the Bureau of Meteorology were obtained. A final check for distant clouds on the horizon was also made.

7.2 Results

The chart readings $\frac{1}{V}\frac{dV}{dt}$ were multiplied by $\frac{dt}{d\delta}$, the differential of central standard time with respect to solar depression, δ. The resulting quantity is thus proportional to $\frac{1}{I}\frac{dI}{d\delta}$.

Despite the precautions taken to avoid twilights contaminated by clouds, a large proportion of the results are nevertheless believed to be affected by clouds beyond the horizon. These results show sharp fluctuations in the twilight gradient, and have subsequently been discarded in the analysis.

Twilight gradients with respect to solar depression angle observed at St. Kilda are shown in Figures 7.2(a) to (f). The most frequently observed profile is shown in Figure 7.2(f). The value of $d(\ln I)/d\delta$ is typically 0.5 (degree^{-1}) at 2° solar depression, and reaches a peak of approximately 1.5 at 5.2° solar depression. For comparison, a twilight profile measured at Weissenau, Southern Germany in early summer, 1966 (Volz, 1969), is included in Figure 7.2(f). The results are in very good agreement, considering the entirely different localities, and indicates similar vertical distributions of aerosols.

Of particular interest is the sequence of twilight gradients which were observed between December 1, 1965 and February 28, 1966, shown in Figures 7.2(a) to (f). It can be seen that the twilight gradients observe over a wide range of solar depressions between 8th December, 1965 and 18th February, 1966 (curves (b) to (e), Figure 7.2) are significantly greater than the normal twilight gradients, represented by curves (a) and (f) in Figure 7.2. The disturbed records show none of the usual signs of cloud

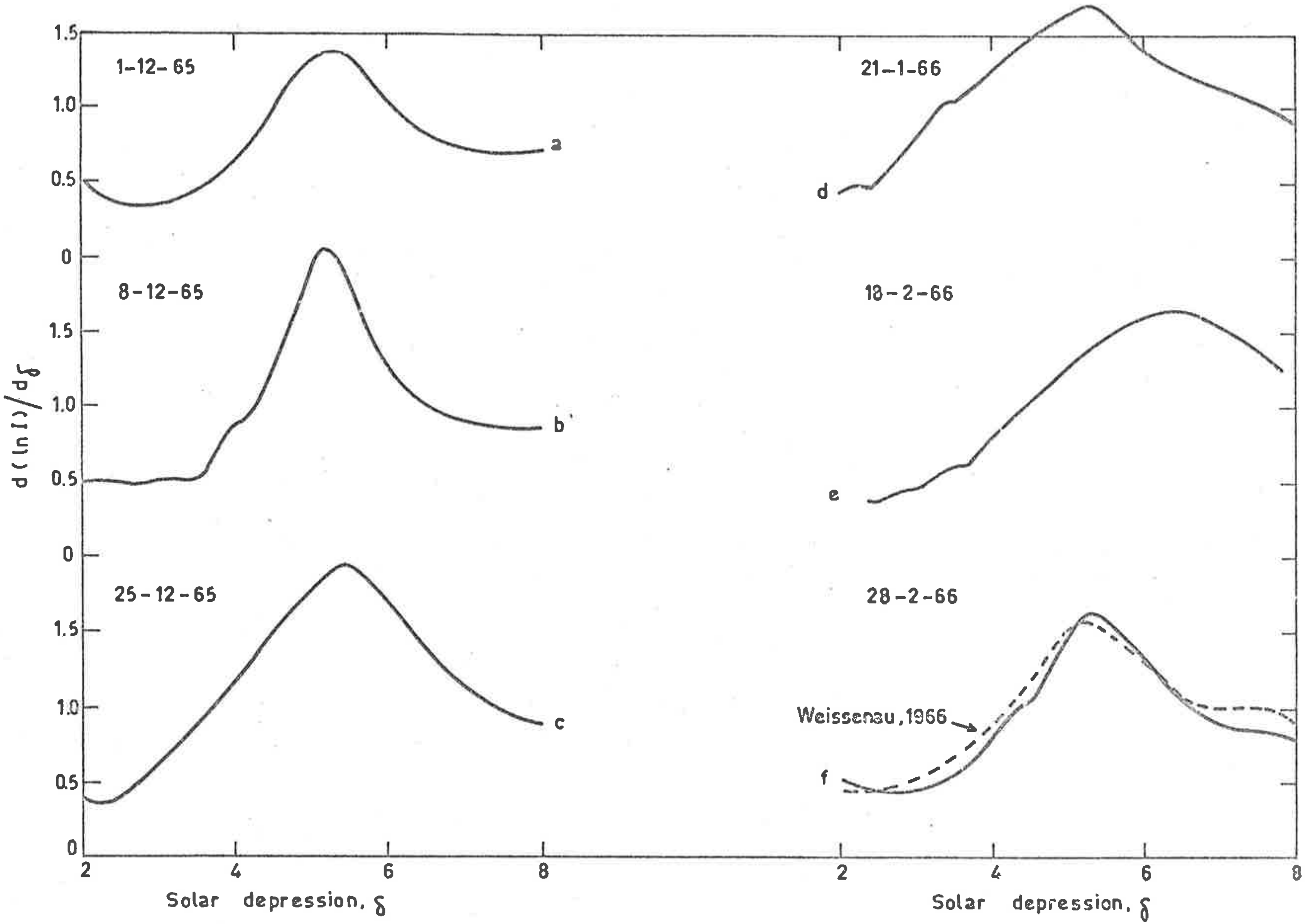

FIGURE 7.2 Sequence of twilight gradients measured at St. Kilda, South Australia.

interference, and have never been recorded since, in over 4 years of observations. It is therefore concluded that the change in twilight profiles during this period is due to an abrupt and abnormal change in the vertical distribution of aerosols over southern Australia. The increase in $d(\ln I)/d\delta$ at solar depressions between 3° and 7° suggests an influx of aerosols in the lower stratosphere.

An enhancement in stratospheric aerosol concentration was also observed at Mt. Stromlo, Australia, in the same period. Measurements at Mt. Stromlo of the ratio of red to green intensities of the twilight sky, which is sensitive to the stratospheric aerosol content, showed a significant increase during December, 1965 and January, 1966 (Volz, private communication, 1969). Enhanced twilight intensities were also recorded at Kitt Peak (32°N) and at San Salvador (13.7°N) during this period. Volz (1970) has ascribed the disturbances in the northern hemisphere to the eruption of Mt. Taal in Luzon on 28th September, 1965. It is also conceivable that the corresponding disturbances in the southern hemisphere could have been due to volcanic debris from Mt. Taal. The material apparently took about 3 months to reach latitude 35°S.

Apart from an enhanced twilight on 18 November, 1966, other twilights observed at St. Kilda up to the end of 1968 were of undisturbed character as shown in Figure 7.2(f). It is of interest to note that enhanced twilight effects were also observed at Kitt Peak in August and September, 1966 (Volz, 1970).

In the above discussion, inferences about the altitude of the stratospheric aerosol layer have been deliberately excluded, due to the uncertainty in the real height of the diffuse shadow boundary. The completion of the laser radar at Adelaide has enabled a direct comparison to be made between twilight and laser measurements made at the same time and location. It is then possible to deduce a value of screening height such that the vertical twilight profiles are compatible with the vertical laser profiles.

7.3 Comparison of Twilight and Laser Results

According to the twilight gradient approach of Bigg (1956, 1964), the vertical profile of d(ln I)/dh versus height h of the shadow boundary reflects the vertical profile of the stratospheric aerosol number density. In the present work, d(ln I)/dh is calculated by the following relation:

$$\frac{d(\ln I)}{dh} = \frac{d(\ln I)}{d\delta} \cdot \frac{d\delta}{dh} \qquad (7.4)$$

It will be shown in a later section that for the wavelengths of importance to the present work (7000 Å) the boundary between the shadowed and sunlit portions of the atmosphere is not sharp. The twilight rays grazing the lowest layers of the atmosphere near the earth's surface are nearly completely attenuated. For radiation of 7000 Å wavelength, attenuation of the twilight rays is significant for perigees of several kilometers, and hence the shadow boundary is very diffuse. Thus it is exceedingly difficult to deduce the quantity h and the corresponding value of dδ/dh.

In order to overcome this difficulty, Rozenberg (1966) has introduced the concept of the "twilight layer". For a given solar depression, the twilight layer represents the range of heights which give rise to most of the observed intensity of scattered sunlight. Above the twilight layer, the optical thickness of the atmosphere is so small, that the scattered intensity contribution is negligible. Below the twilight layer, the scattered intensity is significantly reduced by attenuation of the grazing rays in the lower layers of the earth's atmosphere. However, the concept of the twilight layer is unsatisfactory for most atmospheric investigations because it can be many tens of kilometers in extent.

The concept of a screening height, frequently used in noctilucent cloud analyses (e.g. Fogle, 1966), is employed in the present work. All solar rays grazing the atmospheric layers below the screening height are assumed to be completely attenuated, while those passing above the screening height are assumed to be unaffected. Although it is not possible to determine the value of the screening height from the twilight profile itself (Rozenberg,1966), the comparison of the laser and twilight profiles would enable an estimate to be made.

The present method of determining h and $d\delta/dh$ also includes the effects of atmospheric refraction. According to Rozenberg (1966), refraction is of significance for solar rays of perigees less than 15 km. The refraction is calculated by means of a modified form of the ray tracing process formulated by Lloyd and Low (1964), a brief resume of which follows. A schematic diagram of the path SNQ of a ray from the sun, tangential to the earth's surface and of perigee or screening height, s, is shown in Figure 7.3. For an observer at P, the depression δ of the sun's upper limb corresponding to a shadow height h is

$$\delta = \theta_1 + \theta_2 + \rho_1 + l \tag{7.5}$$

where θ_1 is the angle NOQ, θ_2 is the angle POQ, ρ_1 is the angle TNS describing the refraction undergone by the sun's rays in traversing the path SN, and l is the correction for the semi-diameter of the sun's limb (l = 16'). This correction is required since the position of the sun is defined with respect to its centre, whereas sunset is defined in terms of the setting of the sun's upper limb. The value of ρ_1 is dependent on the screening height s, and for zero screening height the normally accepted value of ρ_1 is 34' (Lloyd and Low, 1964). The variation of ρ_1 with s used in the present work follows that reported by Rozenberg (1966), but modified so that ρ_1 at ground level is 34'. The relation is

$$\rho_1 = 0.0099 \exp(-0.16s) \tag{7.6}$$

where s is expressed in km and ρ_1 in radians.

Applying Snell's law of refraction, the differential equation relating increments of $\chi(= \frac{h - s}{r + s}$, where r is the radius of the earth) to those of θ_1 for a ray such as NQ in Figure 7.3 can be shown to be

$$d\theta_1 = \frac{d\chi}{(1 + \chi)\left[\frac{\mu^2}{\mu_s^{\,2}}(1 + \chi)^2 - 1\right]^{\frac{1}{2}}} \tag{7.7}$$

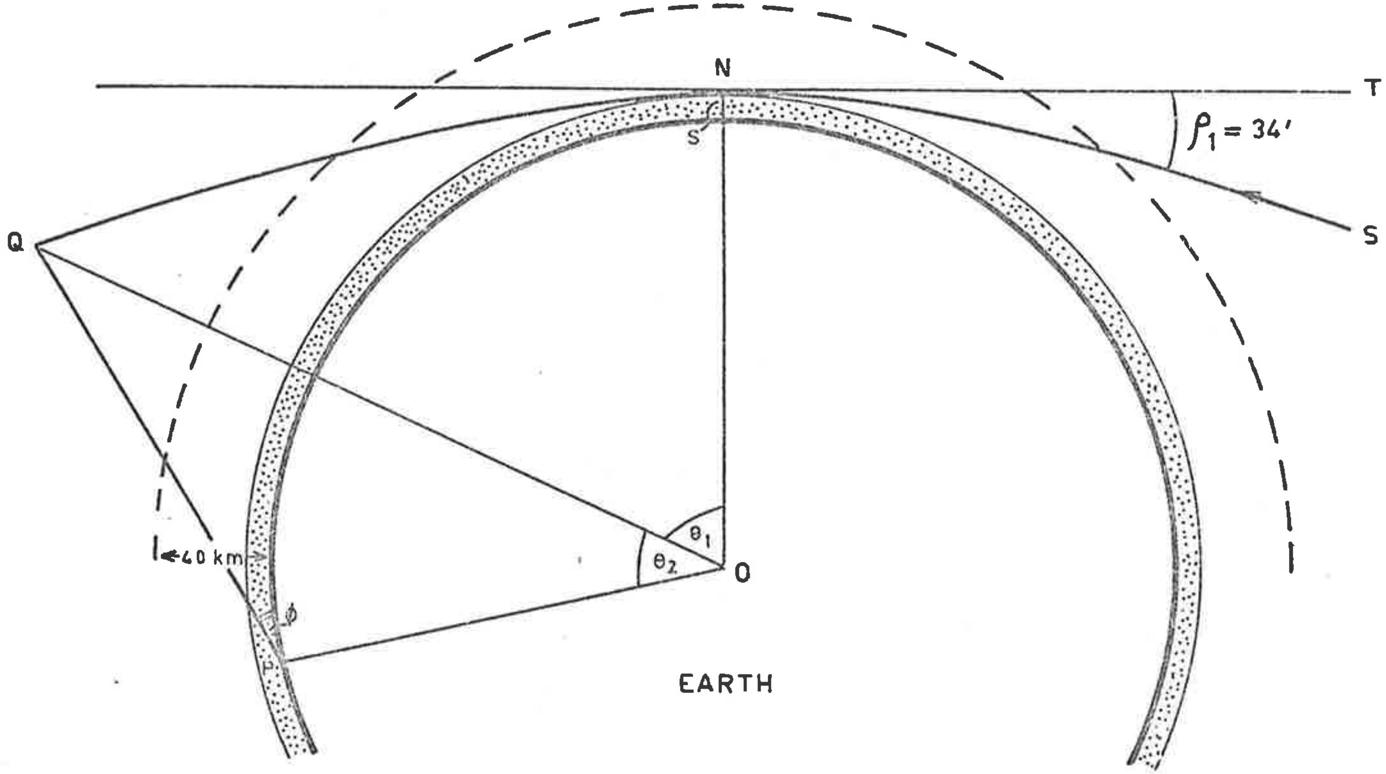

FIGURE 7.3 Schematic diagram of the twilight scattering experiment.

The refractive index μ at height h above ground level is calculated using the following relation.

$$\mu = 1 + \kappa \frac{\rho}{\rho_o} \tag{7.8}$$

where $\kappa = 0.000275$ for a wavelength of 7000 Å, and ρ/ρ_o is the ratio of the density at height h to that at ground level. The parameter μ_s is the refractive index at the screening height s and is calculated using equation 7.8.

In the altitude range $h' = h - s = 0$ to 0.5 km, $\chi << 1$, and equation 7.7 can be integrated analytically to give

$$\theta_1 = c \ln \left\{ \frac{\sqrt{\chi}}{\sqrt{a^2}} + \sqrt{1 + \frac{\chi}{a^2}} \right\} \tag{7.9}$$

where

$$c = 2\left\{\frac{\kappa}{H_s'^2} (1 + H_s'\tau)\right\}^{-\frac{1}{2}} , \tag{7.10}$$

$$a^2 = \frac{2H_s'(H_s' - \kappa)}{\kappa(1 - H_s'\tau)} , \tag{7.11}$$

$$\tau = \frac{1}{H} \left(\frac{\partial H}{\partial \chi}\right)_{h'=0} \tag{7.12}$$

and $H' = \frac{H}{r + s}$, H being the density scale height. The parameter H_s' is the value of H' at $h' = 0$. Equation 7.7 may also be integrated analytically for high altitude values ($\gtrsim$ 40 km) where $\mu \rightarrow 1$. Then

$$\theta_1 = \cos^{-1} \left\{\frac{\mu_s}{1 + \chi}\right\} + \rho_1 \tag{7.13}$$

where ρ_1 is given by equation 7.6.

For values of h′ between 0.5 and 40 km, expression 7.7 cannot be integrated analytically, and hence a numerical method is used.

Referring to Figure 7.3, the line of sight of an observer at P, elevated by an angle ϕ above the horizon, intersects the twilight ray at point Q. For an angle ϕ of 19° used in the present work, refraction effects are relatively small, and a linear sightline PQ is assumed. It can be shown that under this assumption, the angle POQ is

$$\theta_2 = \cos^{-1}\left\{\frac{\cos\phi}{1+\chi}\right\} - \phi \quad . \qquad (7.14)$$

It can be seen in Figure 7.3 that knowledge of both θ_1 and ϕ uniquely determines the value of θ_2, and hence solar depression, δ, according to equation 7.5. Thus for each value of solar depression considered, the present computational procedure progressively increases θ_1 until equation 7.5 is satisfied, thus determining the shadow height h.

All computations have been performed on the University of Adelaide's CDC 6400 computer. The numerical integration of equation 7.7 is carried out in 25 m height intervals for the lower levels, increasing to 100 m steps approaching 40 km altitude. Densities and scale heights are calculated using the U.S. Standard Atmosphere (1962).

In order to demonstrate the effect of altering the screening height, calculations of d(ln I)/dh profiles for several values of s using results obtained on 17 February, 1969, are shown in Figure 7.4. An increase in s by Δs gives rise to an increase in the peak of the twilight gradient by an amount slightly greater than Δs, due to the decrease

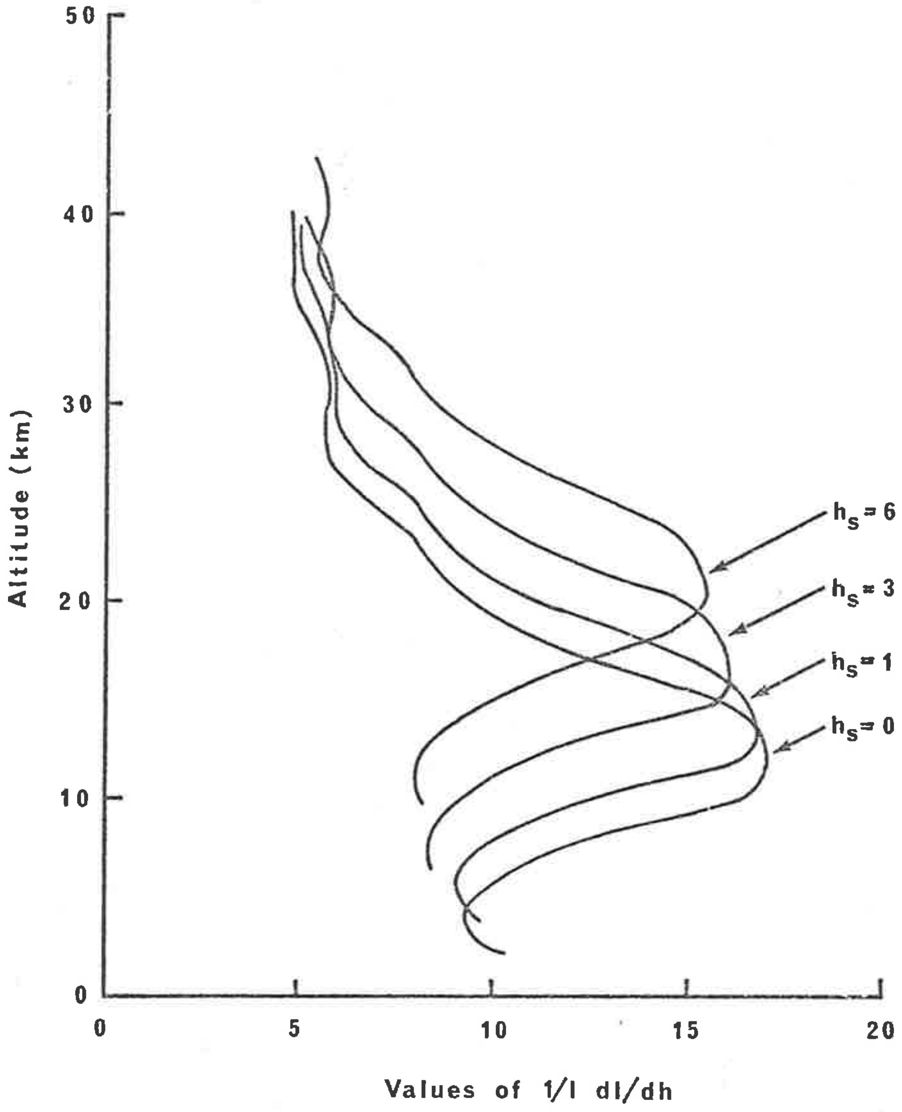

FIGURE 7.4 Variation of the twilight gradient profile with the value of the screening height, h_s.

in refraction with height. This effect becomes greater as the solar depression increases, and hence the twilight profile is broadened as s is made larger. At the same time, the magnitude of the peak is reduced due to the decrease of $d\delta/dh$ with solar depression.

Figure 7.5 shows the results of the comparison of laser and twilight profiles for a sequence of observations in August 1969. The value of screening height for each twilight observation was adjusted until the peaks in the twilight and laser profiles matched. Several points are noteworthy. For these observations, the screening height varies between 6 and 7 km, in agreement with the model atmosphere calculations of Volz and Goody (1962). However, other comparisons result in screening heights as low as 3 km. As the screening height is determined by the optical characteristics of the troposphere, it is understandable that the magnitude of s varies significantly from one day to another. The average screening height is about 4.5 km. The variability in s casts a serious doubt on the twilight gradient method for the study of the height distribution of aerosols, as the uncertainty in s leads to an uncertainty in the altitude of the peak aerosol concentration in the stratosphere.

A further point of interest revealed in the comparison shown in Figure 7.5 is the smoothness of the twilight profiles compared with the aerosol distribution determined by the laser radar. In particular, the peak in scattering ratio at 15 km in the laser profile measured on August 21 is not reproduced in the twilight gradient. This suggests that the vertical resolution of the twilight method is several kilometers, as noted by

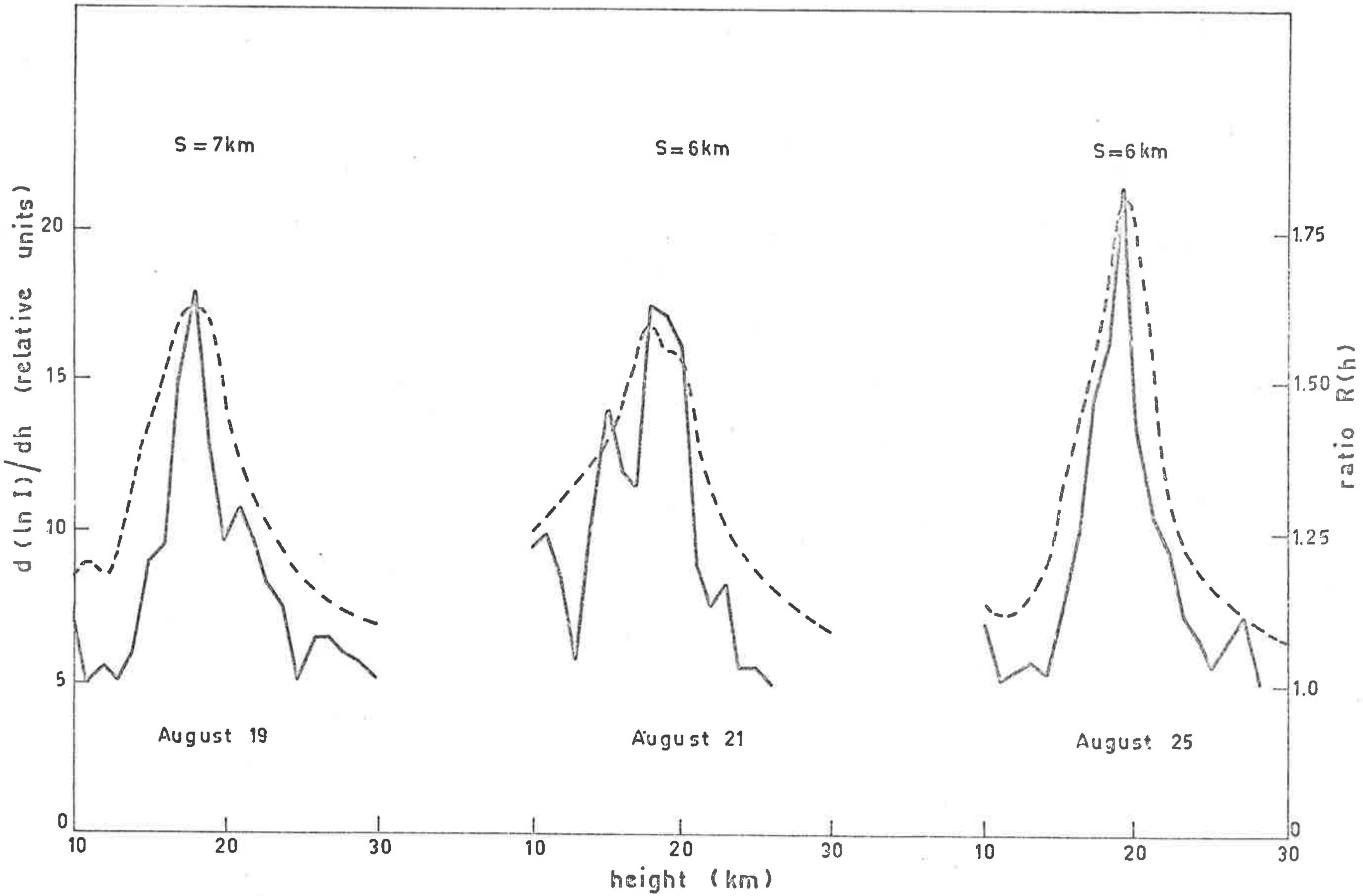

FIGURE 7.5 Comparison of laser (solid curves) and twilight (dashed curves) profiles.

Megrelishvili (1958) and Rozenberg (1966). This is in disagreement with the results of Bigg (1956, 1964), who related sharp discontinuities in the twilight gradient to temperature inversions, thus implying that the fluctuations represent real aerosol layers. It is of interest to note that in the present work no such discontinuities have been recorded, although on some occasions fluctuations of a random nature were observed.

The relative variation in the peak magnitudes of both the laser ratios and d(ln I)/dh in Figure 7.5 is of particular interest. On August 19 and 21, the peak values determined by both methods remain steady, while on August 25, both profiles show a sharp increase. The overall shapes of the two sets of profiles are also in good agreement.

In general, however, there is not a very good agreement between laser and twilight gradient results, as Figure 7.6 shows. The significant increase in aerosol concentration measured with the laser radar on July 2 was not reproduced in the twilight gradient. Furthermore, the marked seasonal trend evident in the laser results for 1969 is not shown in the twilight gradients measured over the same period. The twilight gradients measured over the previous years also show no evidence of a seasonal trend. This is contrary to the variations to be expected from the stratospheric circulation mechanism expounded in Chapter 5, and to the seasonal trend observed by Rosen (1969(a)) in the northern hemisphere.

Unlike the laser radar, which samples one particular height at a given time, the twilight method integrates the scattered solar radiation from the shadow boundary to the upper levels of the atmosphere. Furthermore,

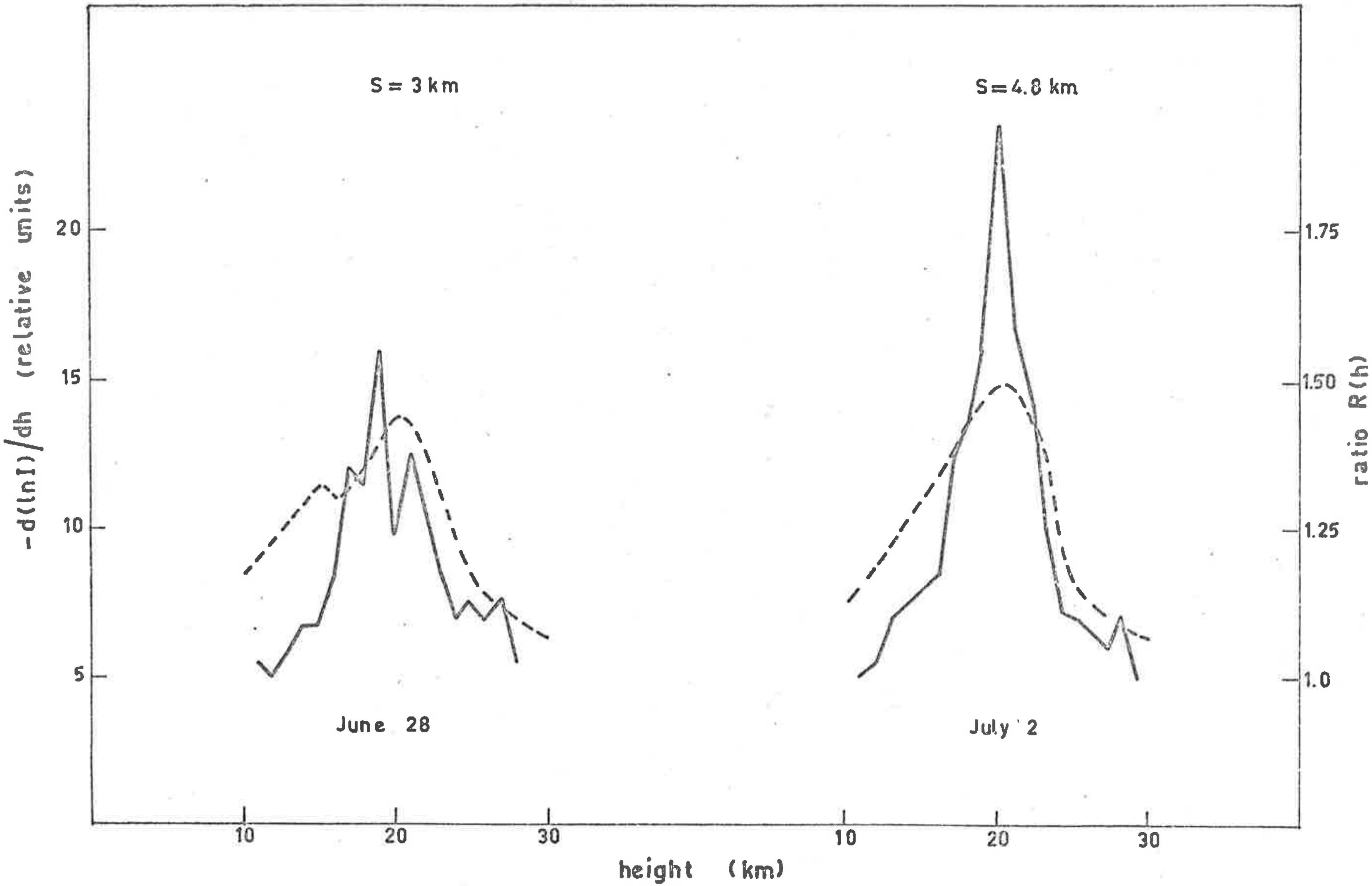

FIGURE 7.6 Comparison of laser (solid curves) and twilight (dashed curves) profiles.

the red solar radiation of significance to the present work is affected as it grazes the tropospheric layers in its path to the scattering volume. It is thus clear that a large region of the atmosphere plays a significant role in determining the radiance, and hence gradient, of the twilight sky at a given solar depression. It follows that factors other than the stratospheric aerosol layer could modify the peak in the twilight gradient. It is therefore concluded that the feature of the peak observed in the twilight gradient is principally caused by the stratospheric aerosol layer, but the relative magnitude of the peak is also affected by other factors, not immediately obvious in the present experimental results.

In order to examine this problem further, a theoretical twilight model was developed, and is discussed in the following section.

7.4 Theoretical Twilight Model

The geometry of the theoretical twilight model is shown schematically in Figure 7.7. The atmosphere is assumed spherically stratified, and is divided into 101 layers of equal thickness above the terminator, extending from ground level (layer 1) to 100 km (layer 101). Most of the computations never extend to the 100 km layer as the integrations converge at lower heights. The formula for the observed intensity of the twilight sky adopted in the model is similar to that proposed by Dave and Mateer (1968). Assuming primary scattering only, the ratio of the observed intensity I of the twilight sky to the incident irradiance E_o is given by

$$\frac{I}{E_o} = \int_o^\infty [\beta_A P_A(\psi) + \beta_R P_R(\psi)]\ T_1 T_2 T_3 \sec \xi \ dh \qquad (7.15)$$

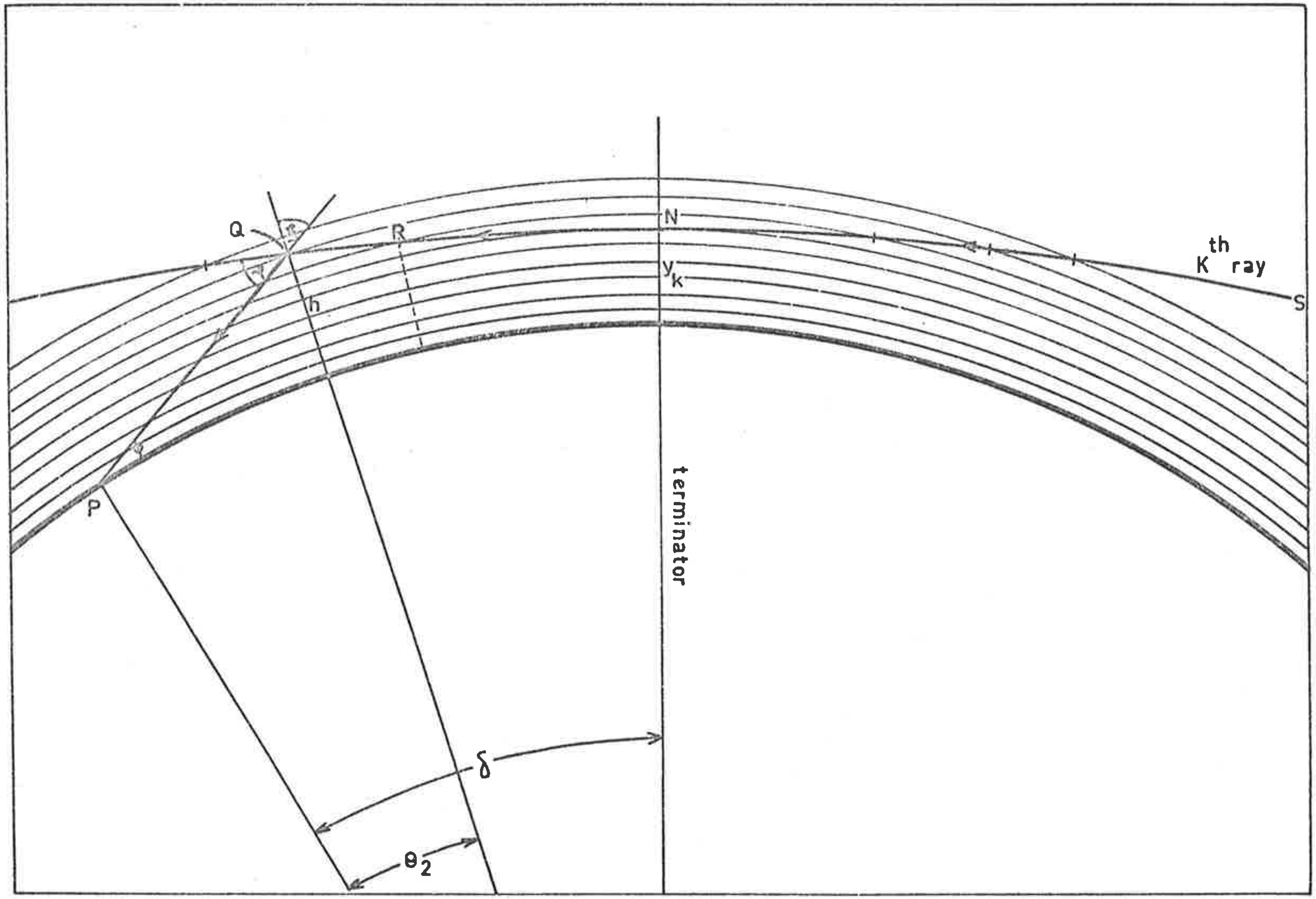

FIGURE 7.7 Geometry of the twilight scattering model.

where β_A and $P_A(\psi)$ are, respectively, the aerosol scattering coefficient at height h and the aerosol phase function at the scattering angle ψ. The variables β_R and $P_R(\psi)$ are the corresponding quantities for the molecular component. The term T_1 is the atmospheric transmission from the outer regions of the atmosphere to the perigee point, defined by the path SN in Figure 7.7. T_2 is the transmission over the path NQ, and T_3 is the transmission along QP. The angle ξ is shown in Figure 7.7, and the term sec ξ accounts for the variation in optical thickness of the scattering volume at Q due to the angle of approach of the solar ray. The integration in equation 7.15 is performed numerically by adding the contributions from k solar rays having perigee heights commencing at zero and increasing by 1 km steps.

The refraction of each ray along the path SQ having perigee height y_k is calculated by the ray tracing method outlined in the previous section. During the ray tracing calculation, the transmission terms T_1 and T_2 are calculated by the following method. Starting at point N, at height y_k, the ray is traced until it reaches height y_k + 1 km, the length of the path NR being $l_{k,i}$ ($i = 1$ in this case). The optical thickness over $l_{k,i}$ is

$$\tau_{k,i} = l_{k,i}\,\beta_j\,, \qquad j = k + i - 1 \qquad (7.16)$$

where β_j is the attenuation coefficient of the j^{th} layer. This procedure is continued, and in the case of T_2, the calculation is terminated at the scattering point Q after i_2 steps. In the case of T_1, the ray tracing is continued further until no significant contribution to the optical thickness is added (i_1 steps). The transmission of the k^{th} ray is in general

$$T_{1,2} = \exp-\left\{\sum_{i=1}^{i_1,i_2} \tau_{k,i}\right\} \qquad (7.17)$$

The transmission term T_3 is calculated by assuming a linear sightline and a horizontally stratified atmosphere.

The phase function for the molecular atmosphere is given by

$$P_R(\psi) = \frac{3}{4}(1 + \cos^2\psi) \qquad (7.18)$$

and the aerosol phase function $P_A(\psi)$ of Volz and Goody (1962) is adopted, values of which are reproduced in Table 7.1.

TABLE 7.1

ψ	16°	20°	25°	30°	60°	90°
P_A	5.70	4.50	3.78	2.53	0.64	0.18
P_R	1.44	1.41	1.37	1.31	0.94	0.75

The divergence effect of the refracted solar rays, which modifies the brightness of the twilight sky, is automatically generated in the model. The perigee height intervals were limited to 1 km in order to keep the computational time within reasonable limits. The molecular scattering coefficient were based on densities according to the U.S. Standard Atmosphere (1962), and the ozone profile of Elterman (1968) was included in the model. The purpose of the following calculations is to demonstrate the effect of various aerosol optical mixing ratio profiles on the twilight gradient, calculated assuming primary scattering. The aerosol data employed in the model are the results of observations made in the vicinity of Adelaide, and hence are as near as possible to the actual distributions occurring in the twilight measurements. All computations are for a wavelength of 7000 Å.

The profile of the first aerosol optical mixing ratio investigated is shown as curve 1 in Figure 7.8. The optical mixing ratio profiles represented by curves 2, 3 and 4 in Figure 7.8 will be referred to later in this chapter. The ground level value was derived from nephelometer measurements of Crosby and Koerber (1963), and the average results of the present laser measurements were used between 3 and 30 km. The data were interpolated between 0 and 3 km. Above 30 km, the optical mixing ratios were adjusted to match the profile proposed by Dave and Mateer (1968), with a constant ratio above 45 km of 0.032. The results of the model twilight calculations are shown in Figure 7.9 (curve 2), together with the twilight profile observe on 17 February 1969 for comparison (curve 1). The height scale on the abscissa is the altitude of the ray at the scattering point Q with zero screenin height. The theoretical and experimental profiles are in good agreement considering the averaged aerosol model used, and the simple primary scattering theory.

Curve 3 in Figure 7.9 is the theoretical gradient for a pure molecular troposphere, but for the same stratospheric aerosol distribution discussed above. The height of the peak is significantly increased, and in fact is centred at the height of the peak aerosol optical mixing ratio. This suggest

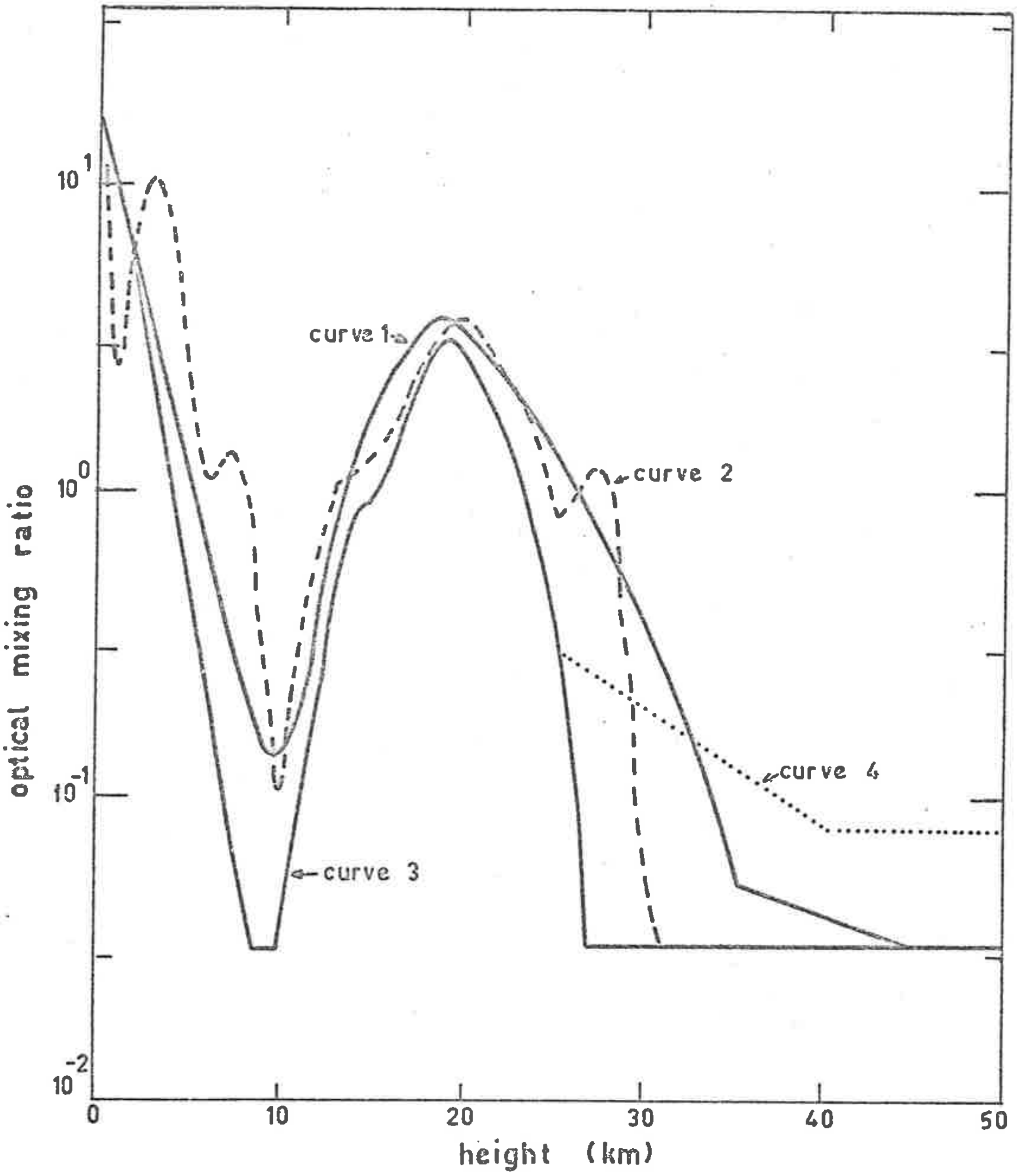

FIGURE 7.8 Optical mixing ratio profiles used in the model calculations.

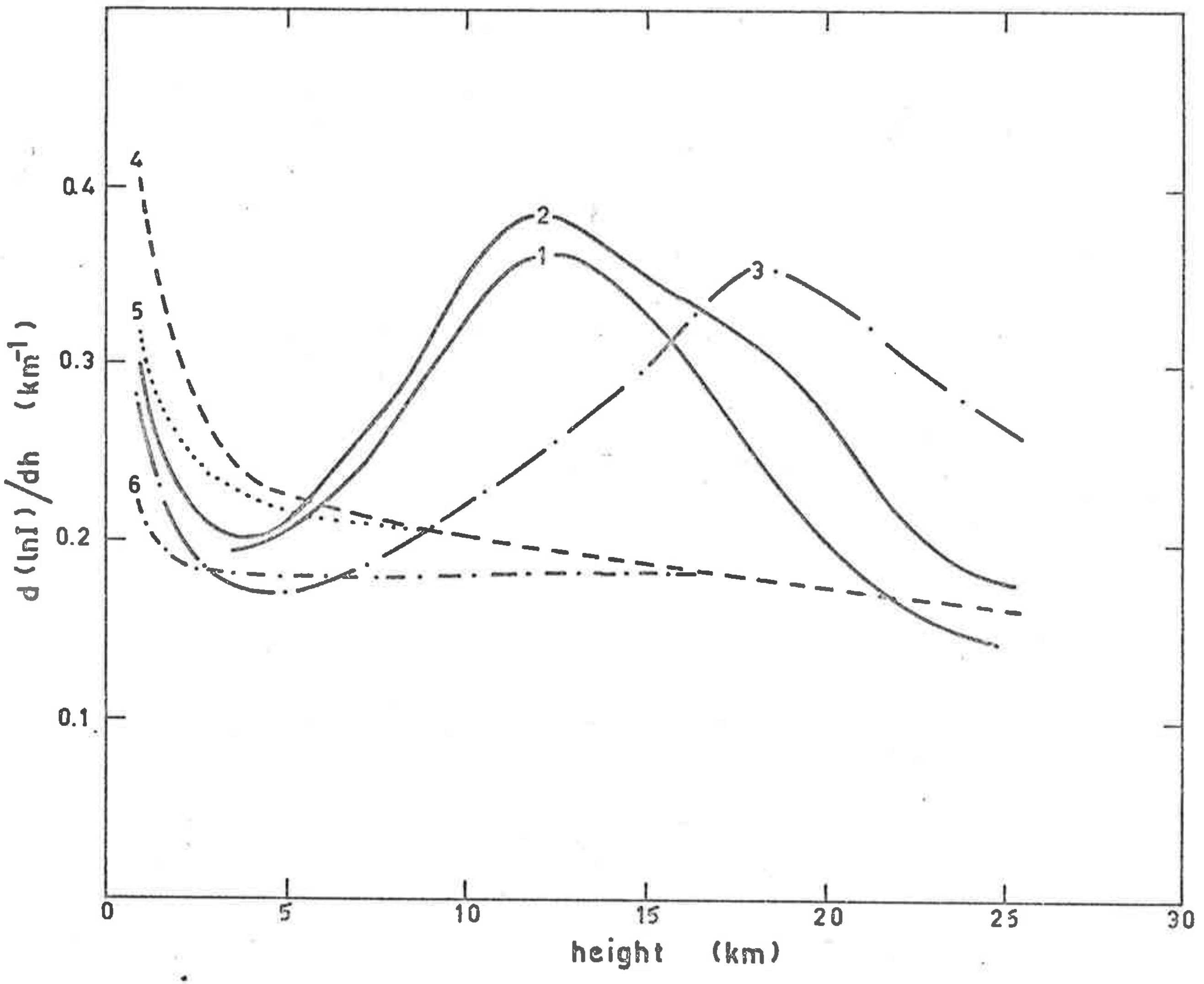

FIGURE 7.9 Calculated changes in the twilight gradient due to varying amounts of aerosols in the troposphere and stratosphere.

that the aerosols in the lower layers of the troposphere are primarily effective in attenuating the grazing solar rays, necessitating the use of a screening height in the data reduction. It is of interest to note that the difference in the heights of the peak gradients of curves 1 and 3 is approximately 6 km, and in good agreement with the value of screening height determined by comparing the laser and twilight profiles. Curve 4 is the twilight gradient for an atmosphere with tropospheric, but no stratospheric aerosols. As to be expected, the gradient in the tropospheric region is increased, due to the reduced intensity contribution from the stratosphere. The gradient in the stratospheric region (curve 4) approaches that of a pure molecular atmosphere, shown as curve 5. It is of interest to note that curve 5 still shows a significant increase in the region of the troposphere, and is much greater than the value of $^1/H$ predicted by equation 7.1 of Bigg (1956). This characteristic is principally a result of the variation in T_2 as the sun sets below the horizon. For small solar depression angles, the optical thickness of the path NQ (see Figure 7.7) rapidly changes. This effect is clearly demonstrated in curve 6 (Figure 7.9), which is the result of calculations for a molecular atmosphere for which T_2 was held constant for all solar depressions.

Figure 7.10 shows the variation of observed intensity of each solar ray as a function of the height of the scattering point Q (see Figure 7.7). The curves are for a pure molecular atmosphere, and for the model aerosol distribution discussed above. Two solar depressions are considered. Each dot on the curve represents the intensity of a given solar ray, and hence the sky brightness for a particular solar depression

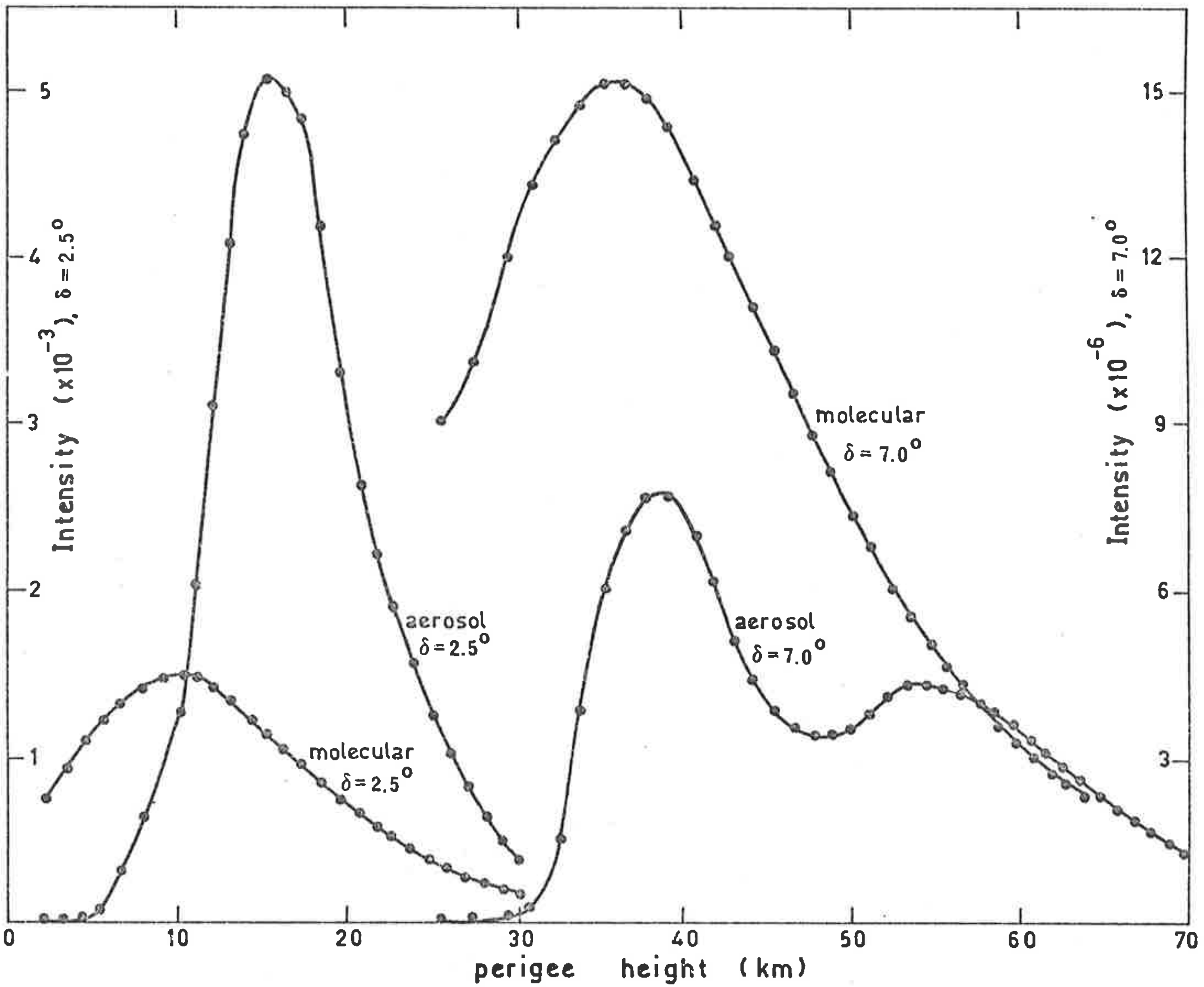

FIGURE 7.10 Calculated intensities of individual solar rays having various perigee heights, for two values of the solar depression.

is given by the area under each curve. The effect of attenuation of the rays by aerosols in the first 5 km of the lower troposphere is clearly evident in the curves for both solar depressions. It is of interest to note the relative magnitudes of the intensities for the different values of solar depression angle. At small solar depressions, the overall effect of aerosols in the troposphere and stratosphere is to increase the total sky brightness. The increase in attenuation due to aerosols in the lower troposphere is more than offset by the increase in scattering at the higher altitudes. However for solar depressions near 7°, most of the aerosols are in the earth's shadow, and no longer contribute to the sky brightness. The increase in attenuation by aerosols in the lower troposphere still takes place, however, and hence the brightness of the atmosphere with aerosols is less than that of a molecular atmosphere. The double peak in the curve for the atmosphere with aerosols and $\delta = 7^{\circ}$ is due to attenuation of the solar rays grazing the stratospheric aerosol layer. The maximum attenuation occurs in rays 17 and 18, which have perigee heights near the altitude of the maximum stratospheric aerosol turbidity.

Figure 7.11 shows a comparison of experimental and theoretical twilight gradients with respect to solar depression. The experimental gradient measured on 27 December, 1969, is shown as the continuous curve. The circles denote the theoretical calculations for which the aerosol profil (Figure 7.8, curve 2) was derived from laser measurements taken at the same time as the twilight observations. There is a discrepancy between theoretical and experimental twilight profiles at either side of the peak value of the gradient. For small solar depressions, the discrepancy is indicative

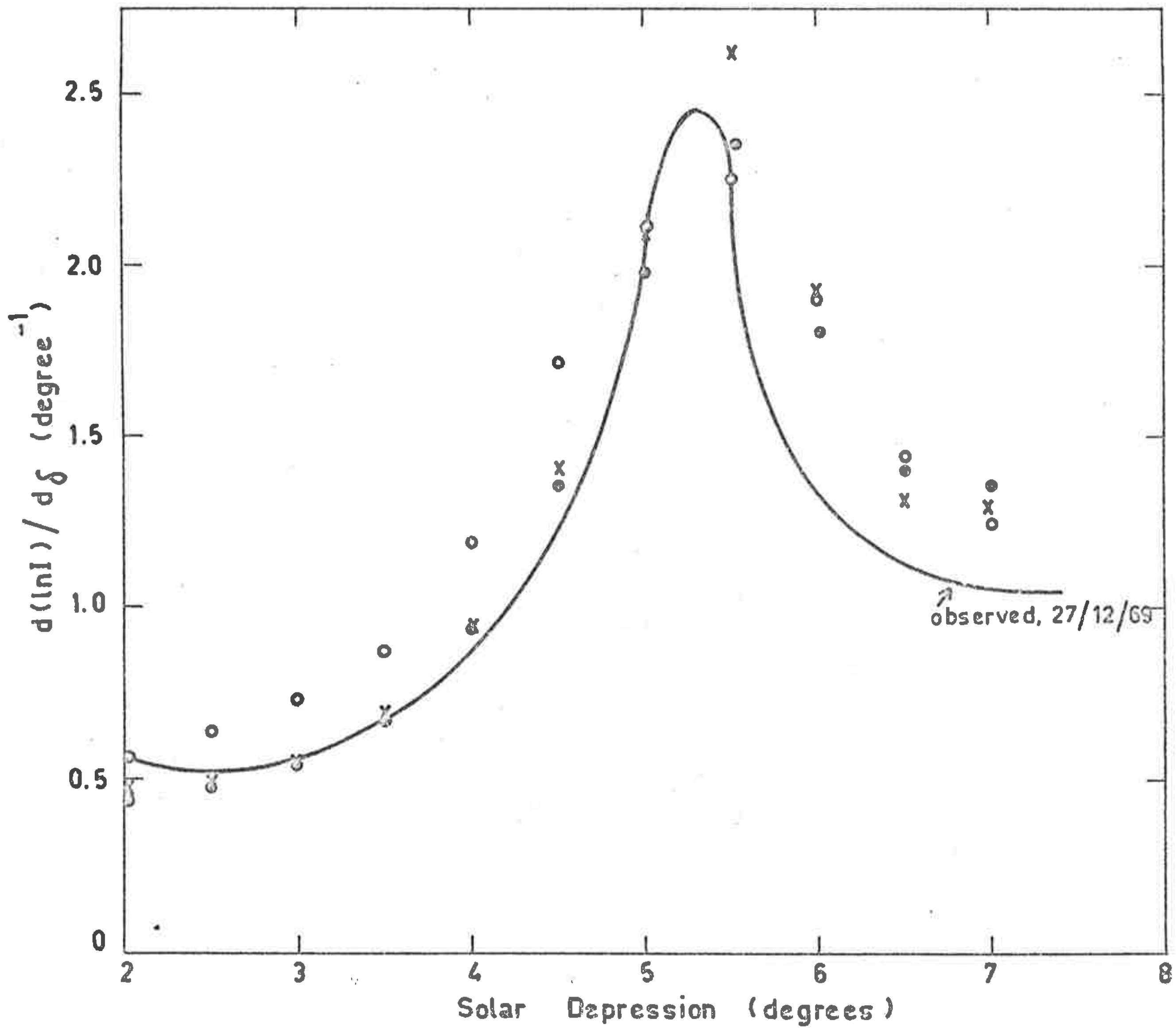

FIGURE 7.11 Comparison of theoretical and observed twilight gradients.

of an excess concentration of aerosols in the troposphere. It is of interest to note that the laser measurements on 27 December, 1969, indicated an unusually large concentration of tropospheric aerosols. As the spatial distribution of aerosols is affected by meteorological events, it is likely that the aerosol measurements using the laser radar are not representative of the mean aerosol distribution over the wide area sampled by the twilight experiment. This argument is also applicable to the stratospheric aerosol distribution, as results in Chapter 5 show a dependence of the stratospheric aerosol profile on the upper level synoptic pattern. For these reasons, the aerosol profile derived from the single laser radar measurement on 27 December, 1969, was replaced by the average for the month, and is shown in Figure 7.8 (curve 3). The theoretical twilight gradient for this aerosol model is represented by the crosses in Figure 7.11. The agreement between theoretical and experimental twilight gradients is good for solar depression angles less than 5°, but a discrepancy still exists for greater solar depression angles.

As the theoretical twilight gradient is greater than the experimental for large solar depression angles, a third model aerosol distribution was included, which differs from the previous profile by the addition of aerosols in the upper stratosphere (Figure 7.8, curve 4). The mixing ratio of these aerosols is constant with height above 40 km, in agreement with the results of Volz and Goody (1962). However, the value of the mixing ratio of these additional aerosols is less than the errors of measurement of the laser radar technique, and hence cannot be detected by the present laser method. The results of the twilight model calculations for this aerosol profile are shown as dots in Figure 7.11. The discrepancy at 5.5° solar depression has been eliminated, but a significant difference between theory and experiment still remains for greater solar depression angles.

The difference between the last two theoretical gradients discussed above suggests that an unusually large aerosol concentration would need to be postulated in the upper stratosphere to account for the discrepancy between theory and experiment. It is therefore suggested that multiple scattering effects cause the experimental twilight gradient to be less that the theoretical for solar depression angles greater than 5.5°. This is broadly in agreement with the results of Morozov (1966) who suggests that multiple scattering exceeds primary scattering at solar depression angles greater than 7°.

The twilight model proposed here has therefore demonstrated that reasonable concentrations of aerosols, undetected by the present laser radar technique,could significantly affect the peak value of the twilight gradient. Multiple scattering effects could also affect the peak gradient, and appear to play a significant role in determining the brightness of the twilight sky for solar depression angles greater than 5.5°.

CHAPTER EIGHT

CONCLUDING REMARKS

A study has been made of the characteristics of aerosols in the troposphere and stratosphere by means of their optical properties. The investigation was carried out using three principal avenues of research; theoretical calculations (Chapter 3), experimental work using a laser radar (Chapters 5 and 6), and experimental observations using the twilight technique (Chapter 7).

8.1 Stratospheric Observations

The results of over a year's observations of aerosols in the stratosphere at latitude 35°S have been presented. To the author's knowledge, these measurements are the first laser radar soundings conducted in the southern hemisphere, and the observations indicate a similarity in the general characteristics of the stratospheric aerosol layer in both hemispheres. The peak aerosol number density in the stratosphere occurs at a height of 18 km, and the layer is some 15 km in depth.

The minimum aerosol scattering at approximately 10 km altitude is in agreement with the measurements of Kondratiev et al (1967), and with the concept that the origin of stratospheric aerosols is entirely different from that of the tropospheric aerosols. This would suggest that the results of Elterman et al (1969), which show no change near the tropopause, are affected by enhanced scattering due to the Bali eruption (March, 1963), some 12 to 24 months prior to the observations. The measurements of Rosen (1969(a)) indicate that the effects of the Bali eruption persisted until at least 1966.

The most significant result of the present stratospheric work is the observation of an annual variation in peak scattering, with a maximum occurring in mid-winter, and a minimum in late summer. This is in agreement with the seasonal dependence of ozone concentration observed at a similar latitude (Pittock, 1968), and supports the concept of a large scale transport mechanism which takes place in the lower stratosphere. Tracers such as ozone, aerosols and radioactive debris appear to be transported polewards from an equatorial reservoir.

Although observations with the laser radar are limited to clear sky conditions and hence are somewhat biassed, the fluctuations observed in stratospheric aerosol scattering over time periods of days are consistent with the concept of an eddy transport mechanism. The variability is unlikely to be a result of a mean meridional motion, unless one postulates similar variability in the aerosol content at the source latitude (Pittock, 1968). In addition, the fluctuations appear to be related to features on the upper level synoptic pattern; high scattering ratios are observed when an upper level trough is in the vicinity, and low scattering ratios are detected whenever an upper level ridge is nearby. This substantiates the concept of an eddy transport mechanism, as the troughs and ridges essentially represent eddies of the general circulation flow pattern. The short time scale fluctuations observed in aerosol scattering do not appear to be correlated with the geopotential height, suggesting that advection is the primary mechanism for day to day variations.

The annual change in variability of scattering by stratospheric aerosols, with a maximum occurring in mid-winter, is very similar to the seasonal dependence of variability observed in stratospheric ozone concentration. Evidently, the tracers become more uniformly distributed in the summer months, when the poleward transport mechanism is least effective

At the time of writing, one interesting feature had become apparent. The observations indicate a considerable difference in aerosol scattering in the 30 to 60 km altitude region during 1969 and 1970. The laser radar results for 1969 show no significant deviation from predictions based on the U.S. Standard Atmosphere (1962), suggesting that the optical mixing ratio in this altitude region is either insignificant or constant with height. As the major source of the stratospheric aerosol appears to originate in the lower stratosphere (Rosen (1969(c)), one may conclude that within the accuracy of the laser experiment, the atmosphere in the 30 to 60 km region during 1969 was predominantly molecular. Calculations show that the optical mixing ratio in this region was less than 0.3. However, the results from February to May 1970, indicate a significant aerosol scatterin contribution in the 30 to 40 km region, suggesting an additional source of aerosols from higher altitudes.

8.2 Tropospheric Observations

At the present time, there are no measurements of the complete aerosol size distribution in the upper troposphere, although the observations of Junge et al (1969) at Crater Lake when subsidence of the air mass occurred, suggest a Junge size distribution with $\nu \sim 2$. Other measurements conducted in the upper troposphere (see Chapter 1) have unfortunately been made over only part of the aerosol size spectrum. However, a comparison of the relative magnitudes of Aitken nuclei and large particle concentrations indicates a Junge size distribution with ν between 2 and 2.5.

Calculations of aerosol number densities in the upper troposphere based on the present laser radar results and a Junge size distribution with $\nu = 2.5$ are in good agreement with measured Aitken nuclei concentrations. This supports the conclusion that due to their overwhelming numbers, the Aitken nuclei primarily determine the optical properties of a "clear" troposphere.

It has been shown that the form of the vertical aerosol scattering profile in the lower troposphere is closely related to the prevailing meteorological conditions. A well-defined aerosol layer at an altitude of approximately 1 km is usually detected when the air mass originates directly from the Southern Ocean. The aerosol layer normally coincides with a layer of moist air, suggesting that the particles are hygroscopic, and the upper altitude limit of the aerosol layer is bounded by a temperature inversion. The scattering characteristics of this aerosol layer quite often fluctuate throughout the day, and on some occasions rapid fluctuations over periods of seconds have been observed. Observations of this layer indicate a diurnal variation, with a maximum aerosol scattering in the late afternoon due to the effects of convection.

The same aerosol layer is observed in the clear blue region of sky between cumulus clouds, which further supports the concept that they are hygroscopic. Moreover, the magnitude of the aerosol scattering is observed to increase as cumulus cloud approaches the scattering volume.

The scattering layer is absent when the air mass originates from the north over the continent. The results, in fact, indicate exceptionally low aerosol scattering in the 1 to 2 km altitude region under these conditions. This is contrary to what one might expect from considerations of convection effects, which are much greater under the conditions of a warm northerly air stream. In addition, experiments discussed in Chapter 1 have shown that the concentrations of continental aerosols are approximately one order of magnitude greater than the concentrations of maritime particles. It is suggested here that the low scattering ratios observed when a northerly air mass is present are a result of the different size distributions of continental and maritime aerosols.

On rare occasions in summer, a third class of scattering ratio profile has been observed. It is identified as a deep, optically dense aerosol layer between 1 and 4 km, which coincides with a very humid air mass, and whose upper boundary is limited by a temperature inversion. The aerosols are believed to be hygroscopic, and could possibly originate from the tropics.

Although little attempt was made to investigate the scattering from clouds, some limited observations of cirrus cloud showed an apparent downwards propagation, superimposed on which were smaller oscillations. The results demonstrate the usefulness of the laser radar equipment in studying some aspects of the formation and development of clouds.

8.3 Discussion

The inherent limitations of the present lidar technique have been outlined in Chapter 3. Basically, the backscattered signal is calibrated at a height where the atmospheric scattering properties are known. As little is known of the scattering properties of aerosols in the upper atmosphere, the calibration is made at a height where it is assumed that the scattering effects of aerosols can be neglected. The present laser radar experiments show that on the average, the 8 to 10 km altitude region is predominantly molecular, as is also the region from 40 to 60 km. The results of the present work indicate that in some recent cases, the 30 to 40 km altitude region, which has been used by other workers as a height for normalisation, contains significant amounts of aerosols.

Two alternative techniques for separating the molecular and aerosol scattering contributions have been proposed. Fiocco and De Wolf (1968) report that due to the Doppler effect resulting from the motion of the scatterers, the frequency spectrum of the scattered light can be resolved into two components. The velocities associated with random

Brownian motions of the aerosols are much smaller than the thermal velocities of the atmospheric gases, and the energy scattered by aerosols is concentrated in a much narrower frequency band than that scattered by the molecular atmosphere. Calculations made by Fiocco and De Wolf indicate that a high resolution spectral analysis using a pressure-scanned Fabry Perot interferometer and a continuous gas laser could yield the ratio of the aerosol to molecular component. As a continuous laser is used, the bistatic experimental configuration, shown in Figure 1.8(b), is necessary, and the observations would be limited to the troposphere due to the low output powers available from existing gas lasers.

Cooney et al (1969) propose the observation of the frequency shifted Raman scattered radiation and the unshifted scattered radiation to separate the gaseous and aerosol contributions. By preferentially rejecting the backscattered return at 6943 Å, the return of the Raman component from N_2 due to the vibrational band centred at 8283 Å could be monitored. The backscattered intensity at 8283 Å depends only on the density of nitrogen molecules, apart from transmission losses, whereas the return at 6943 Å contains both the gaseous and aerosol components. A simple subtraction permits the identification of that fraction of the 6943 Å return due to aerosol scatter. The altitude range of present system is limited to about 5 to 6 km by the magnitude of the Raman return. The technique could, however, be used to calibrate the normal lidar soundings. The greatest error in the method at present appears to be the uncertainty in the Raman scattering cross-section, but accurate measurements of this quantity will no doubt render the Raman technique feasible.

A further difficulty arises in interpreting the value of the aerosol backscattering coefficient $B_A(\pi, h)$, as it is necessary to know the optical characteristics of the particles. Thus, in order to preclude any ambiguities, the annual variation in the scattering characteristics of the stratospheric aerosol discussed in Chapter 5 is presented in terms of the scattering ratio R(h), which is closely related to the aerosol backscattering coefficient (see equation 3.9). The winter maximum scattering ratio might be interpreted as an influx of aerosols, and considering the similarity in the temporal characteristics of aerosols and ozone (discussed in Chapter 5), this interpretation is likely to be correct. However, changes in scattering ratio could also be caused by changes in the chemical composition and physical structure of the aerosols due to chemical reactions, or by changes in the size distribution due to coagulation or condensation effects. The significance of these alternative possibilities is demonstrated in the calculations presented in Section 3.5.

The above uncertainties cannot be resolved using the present laser radar technique alone. It would be of considerable interest to conduct a laser radar sounding simultaneously with an air-borne optical particle counter similar to that described by Rosen (1969(a)). A multichannel optical particle counter would enable the measurement of the aerosol size distribution, in addition to the total number density, thus providing a comparison for the laser radar observations.

More sophisticated laser radar experiments, at present technically feasible, would enable an approximate determination of the size distribution. They include multi-wavelength observations, polarization measurements, and observations at several scattering angles. Three useful wavelengths could be generated using a neodymium-in-glass laser with a provision for frequency doubling, in addition to the existing ruby laser, giving 0.53, 0.694 and 1.06 μ. The wavelength dependence of the scattered intensity could be compared with theoretical values based on different aerosol size distribution models, and an optimum size distribution could thus be determined.

The use of the bistatic configuration of receiver and transmitter would enable the measurement of both the depolarization and a portion of the polar scattering diagram. Although the bistatic method introduces technical problems, such as the alignment of the beams, the additional knowledge gained should justify an investigation of the method.

As the scattered intensity and depolarization are both dependent on the total aerosol number density and the aerosol size distribution, the simultaneous measurements of both intensity and depolarization would enable the determination of the size distribution as well as the number density (Neumann et al, 1969). The depolarization for backscattered linearly polarized light is zero (Eiden, 1966), thus necessitating the bistatic configuration.

A portion of the polar scattering diagram could be measured using the bistatic method, and a mobile transmitter or receiver. The experimental results could be compared with theoretical profiles based on various aerosol size distribution measurements.

As the range of scattering angles is limited using the bistatic arrangement, ground-based measurements of the polar diagram appear less attractive than polarization and multi-wavelength observations.

The results of Mie scattering calculations presented in Chapter 3 are of general interest to optical studies of the atmosphere. In the troposphere where the aerosol size distribution is described by a Junge power law, the calculations show that under clear sky conditions, the Aitken nuclei determine the scattering properties of the atmosphere because of their overwhelming numbers. This is contrary to the normally accepted view that atmospheric haze is primarily caused by the "large" particles (e.g. Bullrich, 1964). A change in the lower cut-off radius of a Junge size distribution due to coagulation effects could significantly alter the optical characteristics of the ensemble of aerosols. The calculations also demonstrate the significance of the value of the slope ν of the Junge size distribution, indicating that the scattering cross-section of low level maritime aerosols ($\nu \sim 2$) is approximately one order of magnitude greater than that of continental aerosols ($\nu \sim 3$).

The investigation of the scattering properties of stratospheric aerosols indicates that of the size distributions reported to date, the exponential and lognormal functions are most compatible with other independent observations. An interesting characteristic of these size distributior is that the scattering cross-sections are virtually independent of wavelength, which is in agreement with the recently published results of direct optical measurements (Kondratiev et al, 1969).

8.4 Twilight Observations

Due to its simplicity, the twilight gradient technique of Bigg (1956, 1964) was adopted to investigate enhanced optical effects as a result of the Mt. Taal eruption, Luzon, in September, 1965. Disturbed twilight gradients were observed between mid-December, 1965 and February, 1966, and are consistent with twilight measurements made at Mt. Stromlo, Australia, during the same period. It is concluded that the abnormal scattering effects were due to volcanic debris, which apparently took about 3 months to reach latitude 35°S. These results are broadly in agreement with those in the northern hemisphere reported by Volz (1970).

The remaining investigation of the twilight phenomenon is concerned with the question of the possibility of deriving the vertical aerosol profile from twilight gradient observations. During 1969, both twilight and laser radar observations were made concurrently whenever possible, and the two vertical profiles were compared. It was shown that the main peak in the twilight gradient resulted principally from the stratospheric aerosol layer. However, due to the variability in the attenuation properties of the lower troposphere, it is not possible to accurately estimate the amount of refraction of the solar rays using the twilight method alone. Hence it was concluded that the twilight gradient approach alone is not suitable for the study of aerosols in the upper atmosphere. These results question the more detailed twilight technique of Volz and Goody (1962), which assumes a model tropospheric aerosol profile.

Some aspects of the twilight phenomenon were investigated using a theoretical model based on primary scattering. The agreement between theory and experiment is surprisingly good, considering the simplicity of the primary scattering model. These calculations clearly demonstrated the significance of tropospheric aerosols in affecting the twilight gradient. In particular, the variation of the transmission through the lower troposphere with the angular depression of the sun is an important factor.

A comparison of theoretically calculated and measured twilight gradients demonstrated the importance of the presence of aerosols above the stratospheric aerosol layer. These additional aerosols, in concentrations below the accuracy of measurement using the laser radar, could reduce significantly the peak value of the measured twilight gradient. The comparison also indicated that multiple scattering effects could be of importance for solar depressions greater than 5.5°.

The above investigation has demonstrated the limitations of the twilight gradient technique, and indeed the more sophisticated technique of Volz and Goody (1962), in studying stratospheric aerosols, and is in agreement with the conclusions of Rozenberg (1966). For this reason, experimental twilight observations have been discontinued at Adelaide.

8.5 Future Work

Some proposals for future work have already been suggested in the foregoing sections. Many of these involve considerable modifications and additions to the equipment, and will not be undertaken in the immediate future.

The stratospheric observations are being continued to monitor the seasonal variation, and to study the day to day fluctuations associated with the eddy transport mechanism. It is proposed to conduct concurrently aerosol and ozone soundings, the latter by means of balloon-borne Brewer sondes, in order to compare the day to day fluctuations. The pulse rate of the laser radar is being increased by a factor of 5, and will enable more accurate measurements. Alternatively the original accuracy could be achieved in a smaller time interval.

Simultaneous observations of aerosols using a laser radar and a balloon-borne optical particle counter would be of considerable interest. As the aerosol size distribution could be measured directly by the counter, the accuracy of the procedure used to normalise the laser radar results could be investigated.

The latitudinal variation in aerosol scattering could be studied using the present mobile apparatus, but is not planned for the immediate future. It would be of considerable interest to construct two additional laser radars to form a spaced receiver network in order to study the spatial and temporal characteristics of the aerosol layer, and to investigate further the nature of the eddy transport mechanism in the lower stratosphere. This project is unfortunately beyond the resources of one department.

An auxiliary receiver is currently being tested to enable laser radar soundings to be made to as low as several tens of metres. The aperture is approximately 6.5 cm, and the design is simplified due to the high light intensities measured. This will enable an investigation of urban atmospheric pollution to be made. The height resolution of the laser radar will be reduced by operating the laser near threshold, which effectively reduces the output to a single pulse approximately 50 nsec in width.

The use of the laser radar in investigating the nature of clouds has been discussed, and it is proposed to intensify efforts in this direction. Recently, laser radar measurements of backscattered radiation from alto-cumulus and cirrus clouds have been made simultaneously with infra-red observations conducted by workers from the Division of Meteorological Physics in the Commonwealth Scientific and Industrial Research Organization. The results will enable more accurate estimates to be made of the heat transfer properties of these clouds, as their height, thickness and optical characteristics can be determined by the laser radar technique.

BIBLIOGRAPHY

Aden, A. L., 1952, A.F.C.R.C. Geophys. Research Paper No. 15.

Aden, A. L., and Kerker, M., 1951, J. Applied Phys., 22, 1242.

Bain, W. C., and Sandford, M. C. W., 1966, J. Atmos. and Terr. Phys., 28, 543.

de Bary, E., and Rössler, F., 1966, J. Geophys. Res., 71, 1011.

Barteneva, O. D., 1960, Bull. Acad. Sci. USSR, Geophys. Ser., P. 1237.

Bigg, E. K., 1956, J. Meteorol., 13, 262.

Bigg, E. K., 1964, Tellus, 16, 76.

Bigg, E. K., 1969, Report presented to Australian Inst. Physics Summer School, La Trobe University, Victoria, January.

Bigg, E. K., 1970, Private Communication.

Blifford, I. H., and Ringer, L. D., 1969, J. Atmos. Sci., 26, 716.

Boville, B. W., and Hare, F. K., 1961, Quart. J. Roy. Met. Soc., 87, 490.

Brewer, A. W., 1949, Quart. J. Roy. Met. Soc., 75, 351.

Bullrich, K., 1964, Advances in Geophysics, 10, 99.

Bullrich, K. R., Eiden, R., Jaenicke, R., and Nowak, W., 1966, Final Tech. Report, J. Gutenberg U., Mainz, Germany, Contract No. DA-91-591-EUC-3458.

Cadle, R. D., Bleck, R., Shedlovsky, J. P., Blifford, I. H., Rosinski, J., and Lazrus, A. L., 1969, J. Applied Meteorol., 8, 348.

Clark, W. E., and Whitby, K. T., 1967, J. Atmos. Sci., 24, 677.

Clemesha, B. R., Kent, G. S., and Wright, R. W., 1966, Nature, 209, 184.

Clemesha, B. R., Kent, G. S., and Wright, R. W. H., 1967, J. Applied Meteorol., 6, 386.

Cooney, J., Orr, J., and Tomasetti, C., 1969, Nature, 224, 1098.

Craig, R. A., 1948, Sc.D. Dissertation, M.I.T., Cambridge, Mass.

Crosby, P., and Koerber, B. W., 1963, J. Opt. Soc. Am., 53, 358.

Dave, J. V., and Mateer, C. L., 1968, J. Geophys. Res., 73, 6897.

Deirmendjian, D., 1963, Rand Report R-407-PR.

Deirmendjian, D., 1965, J. Geophys. Res., 70, 743.

Deirmendjian, D., and Vestine, E. H., 1959, Planet. Space Sci., 1, 146.

Dobson, G. M. B., 1956, Proc. Roy. Soc., A, 236, 187.

Dunkelman, L., Dave, J., Mateer, C., and Evans, C., 1968, N.C.A.R. Quarterly, No. 20.

Dyer, A. J., and Hicks, B. B., 1968, Quart. J. Roy. Met. Soc., 94, 545.

Eiden, R., 1966, Applied Optics, 5, 569.

Eiden, R., 1968, Tellus, 20, 380.

Elterman, L., 1954, A.F.C.R.C. Geophysical Research Paper No. 29, Cambridge, Massachusetts.

Elterman, L., 1966, Applied Optics, 5, 1769.

Elterman, L., 1968, A.F.C.R.L. Environmental Research Papers No. 285, A.F.C.R.L.-68-0153.

Elterman, L., Wexler, R., and Chang, D. T., 1969, Applied Optics, 8, 893.

Feely, H. W., and Spar, J., 1960, Nature, 188, 1062.

Fenn, R. W., 1964, Beitr. Phys. Atmosphare, 37, 69.

Fesenkov, V. G., 1923, Trudy Glav. Ross. Astrofiz. Obs., 2, 7.

Fiocco, G., and De Wolf, J. B., 1968, J. Atmos. Sci., 25, 488.

Fiocco, G., and Grams, G., 1964, J. Atmos, Sci., 21, 323.

Fiocco, G., and Smullin, L. D., 1963, Nature, 199, 1275.

Fogle, B. T., 1966, Scientific Report UAG R-177, Geophysical Institute, University of Alaska.

Friedland, S. S., Katzenstein, J., and Zatzick, M. R., 1956, J. Geophys. Res., 61, 415.

Friedlander, S. K., and Paceri, R. E., 1965, J. Atmos. Sci., 22 571.

Friend, J. P., 1966, Tellus, 18, 465.

Friend, J. P., and Sherwood, R. D., 1961, Rept. Isotopes Inc., Westwood, New Jersey, February.

Garland, J. A., 1969, Atmospheric Environment, 3, 347.

Goyer, G. G., and Watson, R. D., 1968, Bull. Amer. Met. Soc., 49, 890.

Grams, G., and Fiocco, G., 1967, J. Geophys. Res., 72, 3523.

Greenberg, J. M., Pederson, N. E., and Pederson, J. C., 1961, J. Applied Phys. 32, 233.

Gruner, P., 1942, Hand. d. Geophys. (Borntraeger, Berlin), 8, 432.

Heard, M. J., and Wiffen, R. D., 1969, Atmospheric Environment, 3, 337.

Hemenway, C. L., Soberman, R. K., and Witt, G., 1964, Tellus, 16, 84.

Horvath, H., and Noll, K. E., 1969, Atmospheric Environment, 3, 543.

Hulburt, E. O., 1937, J. Opt. Soc. Am., 27, 377.

Hunt, B. G., and Manabe, S., 1968, Monthly Weather Review, 96, 503.

Johnson, E. A., Meyer, R. C., Hopkins, R. E., and Mock, W. H., 1939, J. Opt. Soc. Am., 29, 512.

Junge, C., 1953, Tellus, 5, 1.

Junge, C. E., 1954, J. Meteorol., 11, 323.

Junge, C. E., 1956, Tellus, 8, 127.

Junge, C. E., 1961, J. Meteorol., 18, 501.

Junge, C. E., 1963, "Air Chemistry and Radioactivity", Academic Press, New York.

Junge, C. E., 1969, J. Atmos. Sci., 26, 603.

Junge, C. E., and Manson, J. E., 1961, J. Geophys. Res., 66, 2163.

Junge, C. E., Chagnon, C. W., and Manson, J. E., 1961, J. Meteorol., 18, 81.

Junge, C. E., Robinson, E., and Ludwig, F. L., 1969, J. Applied Meteorol., 8, 340.

Kattawar, G. W., and Plass, G. N., 1967, Applied Optics, 6, 1377.

Kawamura, K., 1957, Papers in Meteorol. and Geophys., 7, 393.

Kellogg, W. W., 1968, Meteorol. Monographs, 9, 2.

Kent, G. S., Clemesha, B. R., and Wright, R. W., 1967, J. Atmos. Terr. Phys., 29, 169.

Kondratiev, K. Ya., Badinov, I. Ya., Ivlev, L. S., and Nikol´skiy, G. A., 1969, Izv., Acad. Sci. USSR, Atmos. and Oceanic Phys., 5, 270.

Kondratiev, K. Ya., Nicolsky, G. A., Badinov, I. Ya., and Andreev, S. D., 1967, Applied Optics, 6, 197.

Kulkarni, R. N., 1963, Quart. J. Roy. Met. Soc., 89, 478.

Kulkarni, R. N., 1966, Quart. J. Roy. Met. Soc., 92, 363.

Kulkarni, R. N., 1968, Tellus, 20, 305.

Landsberg, H., 1938, Ergeb. Kosmischen Phys., 3, 155.

List, R. J., Salter, L. P., Telegadas, K., 1966, Tellus, 18, 345.

Lloyd, K. H., and Low, C. H., 1964, Technical Note HSA 99, Weapons Research Establishment, Australia.

Long, R. K., 1966, Ohio State Antenna Laboratory Tech. Rept. 2156-2, 7.

Martin, D. W., 1956, Sci. Rep. 6, Dept. of Meteorology, M.I.T.

Mastenbrook, H. J., 1968, J. Atmos. Sci., 25, 299.

McCormick, M. P., 1967, Thesis, The College of William and Mary in Virginia, U.S.A.

Meetham, A. R., 1937, Quart. J. Roy. Met. Soc., 81, 262.

Megrelishvili, T. G., 1958, Bull. Acad. Sci., USSR, Geophys. Ser., p. 315.

Middleton, W. E. K., 1958, "Vision Through the Atmosphere", University of Toronto Press.

Mie, G., 1908, Ann. Physik, 25, 377.

Minnaert, M., 1959, "Light and Colour in the Open Air", Bell and Sons Ltd., London.

Minnaert, M. G. J., 1968, J. Opt. Soc. Am., 58, 297.

Moore, D. J., and Mason, B. J., 1954, Quart. J. Roy. Met. Soc., 80, 583.

Morozov, V. M., 1966, Izv., Acad. Sci. USSR, Atmos. and Oceanic Phys., 2, 505.

Mossop, S. C., 1965, Geochim. et Cosmochim. Acta, 29, 201.

Naito, K., Tabata, I., and Yokota, Y., 1968, Papers in Meteorol. and Geophys., 19, 615.

Napper, D. H., and Ottewill, R. H., 1963, "Electromagnetic Scattering", (Ed. M. Kerker) Pergamon Press, Oxford.

Neumann, J., Low. W., and Cohen, A., 1969, Final Rept., Depts. of Meteorol. and Phys., The Hebrew University of Jerusalem, Sept.

Newell, R. E., 1963, Quart. J. Roy. Met. Soc., 89, 167.

Newkirk, G., and Eddy, J. A., 1964, J. Atmos. Sci., 21, 35.

Newkirk, G., and Kroening, J. L., 1965, J. Atmos. Sci., 22, 567.

Normand, C. W. B., 1953, Quart. J. Roy. Met. Soc., 79, 39.

Ohring, G., and Muench, H. S., 1960, J. Meteorol., 17, 195.

Pilipowskyj, S., Weinman, J. A., Clemesha, B. R., Kent, G. S., and Wright, R. W., 1968, J. Geophys. Res., 73, 7553.

Pittock, A. B., 1968, Quart. J. Roy. Met. Soc., 94, 563.

Pittock, A. B., 1969, J. Applied Meteorol., 8, 308.

Powell, R. S., Circle, R. R., Vogel, D. C., and Woodson, P. D., 1967, Planet. Space Sci., 15, 1641.

Reed, R. J., 1953, J. Meteorol., 10, 296.

Reeger, E., and Siedentopf, H., 1946, Optik, 1, 15.

Rosen, J. M., 1964, J. Geophys. Res., 69, 4673.

Rosen, J. M., 1968, J. Geophys. Res., 73, 479.

Rosen, J. M., 1969(a), Rept. AP-28, School of Physics and Astronomy, University of Minnesota.

Rosen, J. M., 1969(b), Rept. AP-29, School of Physics and Astronomy, University of Minnesota.

Rosen, J. M., 1969(c), Space Sci. Rev., 9, 58.

Ross, M. D., 1958, Bull. Amer. Met. Soc., 39, 625.

Rozenberg, G. V., 1960, Soviet Physics Usp., 3, 346.

Rozenberg, G. V., 1966, "Twilight", Plenum Press, New York.

Rozenberg, G. V., 1966a, Paper presented at the International Conference on the Investigation of Noctilucent Clouds, Tallin, 1966.

Rozenberg, G. V., 1967, Izv., Acad. Sci. USSR, Atmos. and Oceanic Phys., 3, 545.

Rozenberg, G. V., and Nikolaeva-Tereshkova, V. V., 1965, Izv. Acad. Sci. USSR, Atmos. and Oceanic Phys., 1, 228.

Simons, D. G., 1958, Air University Quarterly Review, 10, 65.

Soberman, R. K., and Hemenway, C. L., 1965, J. Geophys. Res., 70, 4943.

Twomey, S., 1954, J. Meteorol., 11, 334.

Twomey, S., 1955, J. Meteorol., 12, 81.

U.S. Standard Atmosphere, 1962, U.S. Government Printing Office, Washington, D.C.

U.S. Standard Atmosphere Supplements, 1966, U.S. Government Printing Office, Washington, D.C.

Van de Hulst, H. C., 1957, "Light Scattering by Small Particles", John Wiley and Sons Inc., New York.

Viezee, W., and Oblanas, J., 1969, J. Applied Meteorol., 8, 369.

Volz, F. E., 1969, Applied Optics, 8, 2505.

Volz, F. E., 1970, J. Geophys. Res., 75, 1641.

Volz, F. E., and Goody, R. M., 1962, J. Atmos. Sci., 19, 385.

Weickmann, H., 1955, "Artificial Stimulation of Rain", Proc. 1st Conference Physics Cloud and Precipitation Particles, (H. Weickmann and W. Smith, eds.), pp. 81-88, Pergamon Press, New York (published 1957).

Wigand, A., 1919, Ann. Physik., 59, 689.

Witt, G., 1960, J. Geophys. Res., 65, 925.

Witt, G., 1968, Tellus, 20, 98.

Woodcock, A. H., 1953, J. Meteorol., 10, 362.

Wright, R. W. H., Sandland, P., Kent, G. S., and Clemesha, B. R., 1969, Aeronomy Report No. 32, 72.

Zinky, W. R., 1962, J. Air Pollution Control Assoc., 12, 578.

APPENDIX

PREPRINT OF A PAPER - "Stratospheric Aerosol Measurements by Optical Radar" by K. Bartusek, D. J. Gambling, and W. G. Elford.
J. Atmos. Terr. Phys., 1970 (in press).

GALLEY No. W.A.A 153

J.A.T.P. 2494 **Pergamon Press, Oxford**
1st Proof MS pages 1–15 Galleys 1–5
The Universities Press, Belfast 21.4.70

Journal of Atmospheric and Terrestrial Physics, 1970, Vol. ■■. pp. ■■■–■■■. Pergamon Press. Printed in Northern Ireland

Stratospheric aerosol measurements by optical radar

K. BARTUSEK, D. J. GAMBLING and W. G. ELFORD
Department of Physics, University of Adelaide, Adelaide, Australia

(*Received 5 November* 1969; *in revised form* 15 *February* 1970)

Abstract—A laser radar is being used at Adelaide, South Australia (35°S) for routine studies of upper atmosphere densities and aerosol concentrations to an altitude of 60 km. The transmitter operates at a wavelength of 0·694 μ and generates pulses of 0·2 J energy and 0·5 μsec pulse length at a rate of 20 per min. The receiver is a 12 in. Newtonian telescope equipped with an interference filter of bandwidth 8 Å. The light is detected by a cooled photomultiplier, and the recording is carried out by integrating photon counts from selected height intervals.

Results for the period February–June, 1969 show that, over the height range 10–60 km, the scattering can be considered as molecular with the exception of the region 13–24 km where enhanced scattering is attributed to aerosols. The maximum aerosol number density, averaged over the five months, is estimated as $7{\cdot}9 \times 10^5$ m^{-3} and occurs at a height of 18·5 km.

1. INTRODUCTION

SEVERAL research groups (e.g. KENT *et al.*, 1966; BAIN and SANDFORD, 1966) are using the laser radar technique for routine studies of upper atmosphere densities and aerosol concentrations. Although generally limited to night-time laser method has the advantage, as compared with in situ sampling techniques, that data are continuously available, subject only to weather conditions. The altitude limit of existing systems ranges between 40 and 90 km. All observations reported to date have been carried out from locations north of the equator (GOYER, 1968), and thus there has been a lack of complementary data from the southern hemisphere.

In this paper a laser radar now in operation at Adelaide, South Australia (lat. 35°S) is described, and some preliminary results are presented. The equipment is capable of producing scattering profiles to an altitude of about 60 km with a height resolution of approximately 1 km.

The theory involved in this type of experiment has been adequately described in a number of papers (KENT *et al.*, 1966; PALMER and ZDUNKOWSKI, 1964), and will not be repeated here.

2. EQUIPMENT

(a) *Transmitter*

The basic element is a $6 \times \frac{5}{16}$ in. ruby rod having a Brewster face at one end, and a totally-internally reflecting wedge cut at the other. The optical cavity is completed by a sapphire flat having 16 per cent reflectivity. '*Q*' switching and a 90° change in direction are achieved by a prism rotating at 12,000 rev/min within the optical cavity. The ruby rod is at one focus of an elliptical cavity and is optically pumped by an FX55 Xenon flash tube at the other focus. Both the ruby and flash tube are water cooled.

The laser generator was designed to produce pulses of 1 J energy at a repetition rate of one pulse per second. Unfortunately, in actual operation it was found that near 1 J output, the *Q*-switch prism had a very limited life and suffered severe pitting after 50–60 shots. In order to obtain a reasonable life it has been found necessary to operate the laser at well below its rated energy output. During normal operation the energy per pulse is 0·2–0·3 J distributed between 3 spikes in 0·5 μsec. Under these conditions a prism life in excess of 10,000 shots has been obtained. The firing rate at present is approximately 20 shots/min.

A simplified diagram of the transmitting system is shown in Fig. 1(a). The laser output beam divergence of 10 mrad. is reduced by a factor of twelve in the collimator. A rotating shutter positioned at the focus of the first lens of the collimator is used to cut off the long duration fluorescent emission from the ruby following the main laser pulse. The shutter rotates at the same speed as the laser Q-switch, and is phased in such a way that it is completely closed less than 50 μsec after emission of the laser pulse.

A thin wire stretched across the exit aperture of the collimator scatters a small fraction of the beam to a high speed photo diode. The photodiode output waveform is displayed on an oscilloscope, allowing a constant visual check to be kept on the laser pulse shape during operation. The leading edge of the oscilloscope's timebase gating voltage is used to trigger the recording system.

(b) *Receiver*

A simplified diagram of the optical receiver is shown in Fig. 1(b). The scattered light is gathered by a 12-in. dia., 6-ft. focal length parabolic mirror, and directed by a diagonal flat to an aperture which defines the receiver's field of view. The position of the aperture can be adjusted by means of micrometer screws to allow the receiver's field of view to be aligned with the transmitted beam.

Immediately behind the aperature is a rotating shutter, whose function is to block the receiver for a short period following each laser firing. If this were not done, the intense scattering from the first few kilometers of the atmosphere would lead to overloading of the photomultiplier, and a consequent increase in the noise count. This shutter is also synchronised with the laser Q-switch, and phased so that the receiver aperture is completely uncovered by the time the scattered light has returned from the lowest level of the height range being studied. The shutter rotates at 24,000 rev/min, and its opening time is approximately 30 μsec.

The light passing through the aperture is collimated by a lens of 5-in. focal length and then passed through an interference filter to the detector. The interference filter has a bandwidth of 8 Å, and is mounted so that it may be tilted with respect to the beam axis, allowing it to be accurately tuned to the wavelength of the laser emission.

The detector is an E.M.I. type 9558 B photomultiplier. In order to minimize thermoelectric emission from the photocathode, a Peltier battery is used to cool the tube to approximately −15°C. At this temperature, the noise contribution due to the tube is of the order of 120 counts/sec.

(c) *Recording system*

A block diagram of the recording system is shown in Fig. 2. Single photon pulses from the photomultiplier are amplified by a preamplifier mounted on the photomultiplier housing, and passed through 50 Ω cable to the electronics rack. Following further amplification, the pulses pass to a high speed discriminator whose

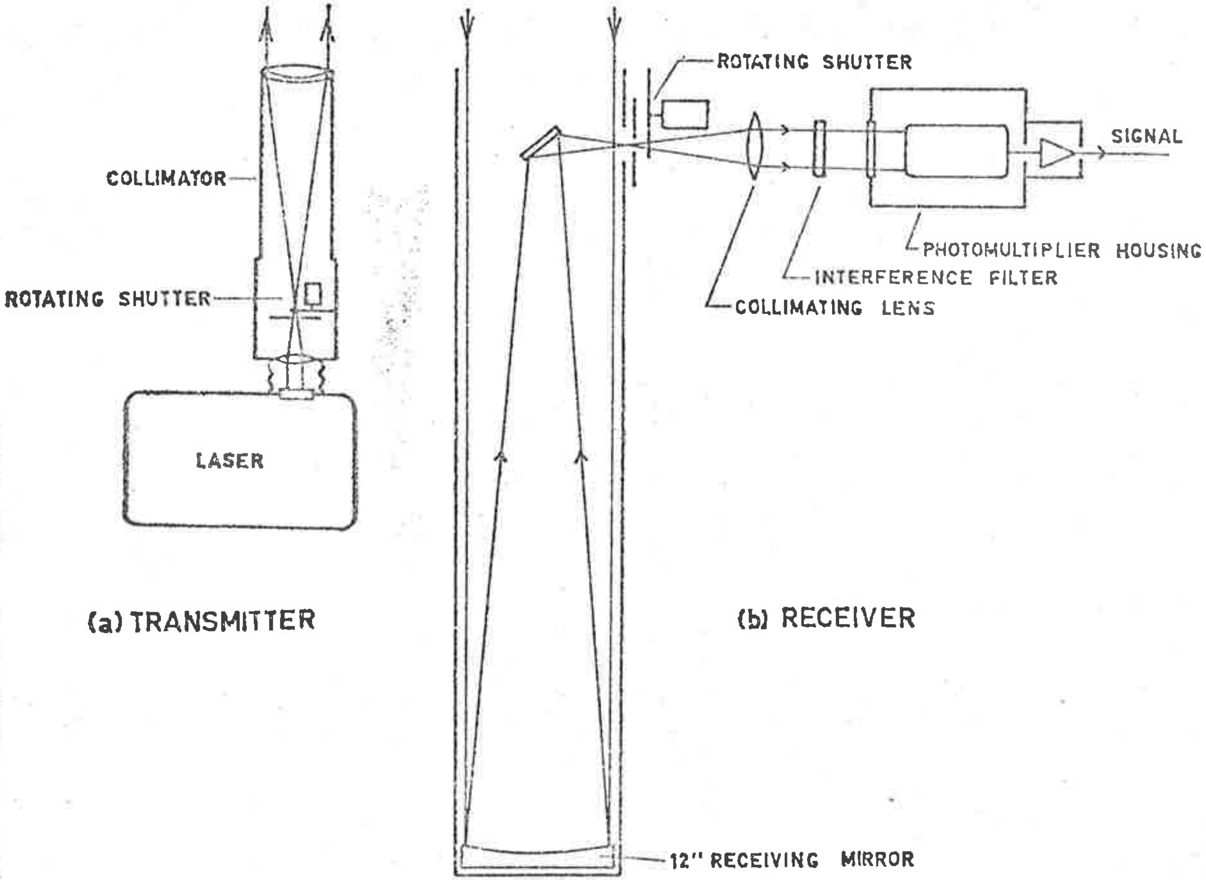

Fig. 1. Schematic diagram of the, (a) transmitting and, (b) receiving systems.

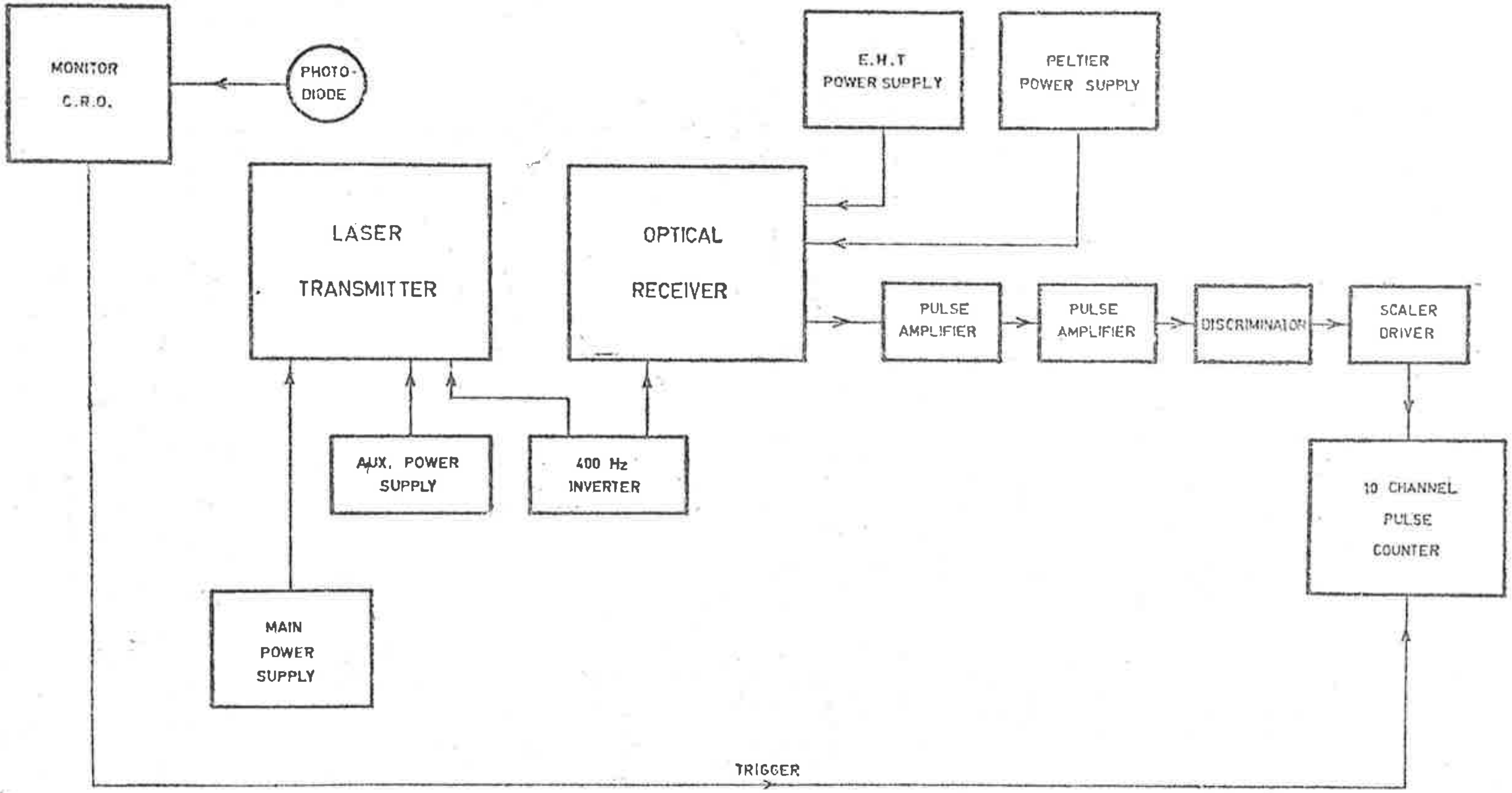

Fig. 2. Block diagram of the main electronic units of the laser radar.

threshold is adjusted to eliminate noise pulses due to the main power supply and triggering circuits.

The standarized output pulses from the discriminator are amplified and further shaped by the scaler driver, and passed to a 10-channel counter which has been specifically developed for the laser system. The channels form 10 successive recording intervals, which in the present equipment may be set at 1, 2, 4 or 8 km. The delay between the arrival of a trigger pulse and the opening of the first channel is adjustable, and may be set to 10, 20, 40 or 80 km.

The resolving time of the whole recording system is 50 nsec, and corrections for non-linearity are applied for average random pulse count rates over 0·2 MHz. In practice, the laser is triggered repetitively, and the signal return from a given height interval is accumulated by the counter. The signal count in each channel is read out manually at the end of a recording sequence, which is usually 200–300 shots. At altitudes up to approximately 20 km a neutral density filter is inserted in the receiver to reduce the count rate to a level which can be accepted by the recording system.

3. RESULTS

The atmosphere contains, in general, a suspended particulate (or aerosol) component, whose concentration varies with height. The photon count $C(h)$ received from a small height interval Δh at height h is therefore a function of the Rayleigh backscattering coefficient $B_R(\pi, h)$ (m^{-1} sterad.$^{-1}$) for the molecular component, and the backscattering coefficient $B_A(\pi, h)$ for the aerosol component. For the case of vertical soundings, it can be shown that $C(h)$ is given by

$$C(h) = k\,\frac{B_R(\pi, h) + B_A(\pi, h)}{h^2}\,\Delta h \qquad (1)$$

where k is a constant for the particular laser radar equipment. For the case of observations over a range of equal height intervals, Δh can be absorbed in the constant, and

$$C(h) = K\,\frac{B_R(\pi, h) + B_A(\pi, h)}{h^2}\,. \qquad (2)$$

The quantity $h^2C(h)$ is thus a measure of the total backscattering coefficient, or scattering index, of the atmosphere at height h.

In Fig. 3, experimentally derived values of $h^2C(h)$ are plotted as a function of height over the range 10–60 km: the graph is the mean of some 35 individual profiles taken over the period February–June, 1969. Included for comparison in Fig. 3 is a curve representing values of $h^2C(h)$ calculated for the case of pure molecular scattering. Molecular densities were obtained from the U.S. Standard Atmosphere 1962, and the laser results were normalized to the calculated curve at a height of 10 km. This choice of the level of normalization differs from that of previous workers who have usually chosen a height between 30 and 40 km where it is generally accepted that the scattering by aerosols is negligible compared to the Rayleigh scattering by the molecular atmosphere (GRAMS and FIOCCO, 1967). In the present investigations the statistical error in the observed scattering index at 30–40 km for an individual profile was considered to be too large for this region to be suitable for normalization of the laser results. Hence a much lower height for

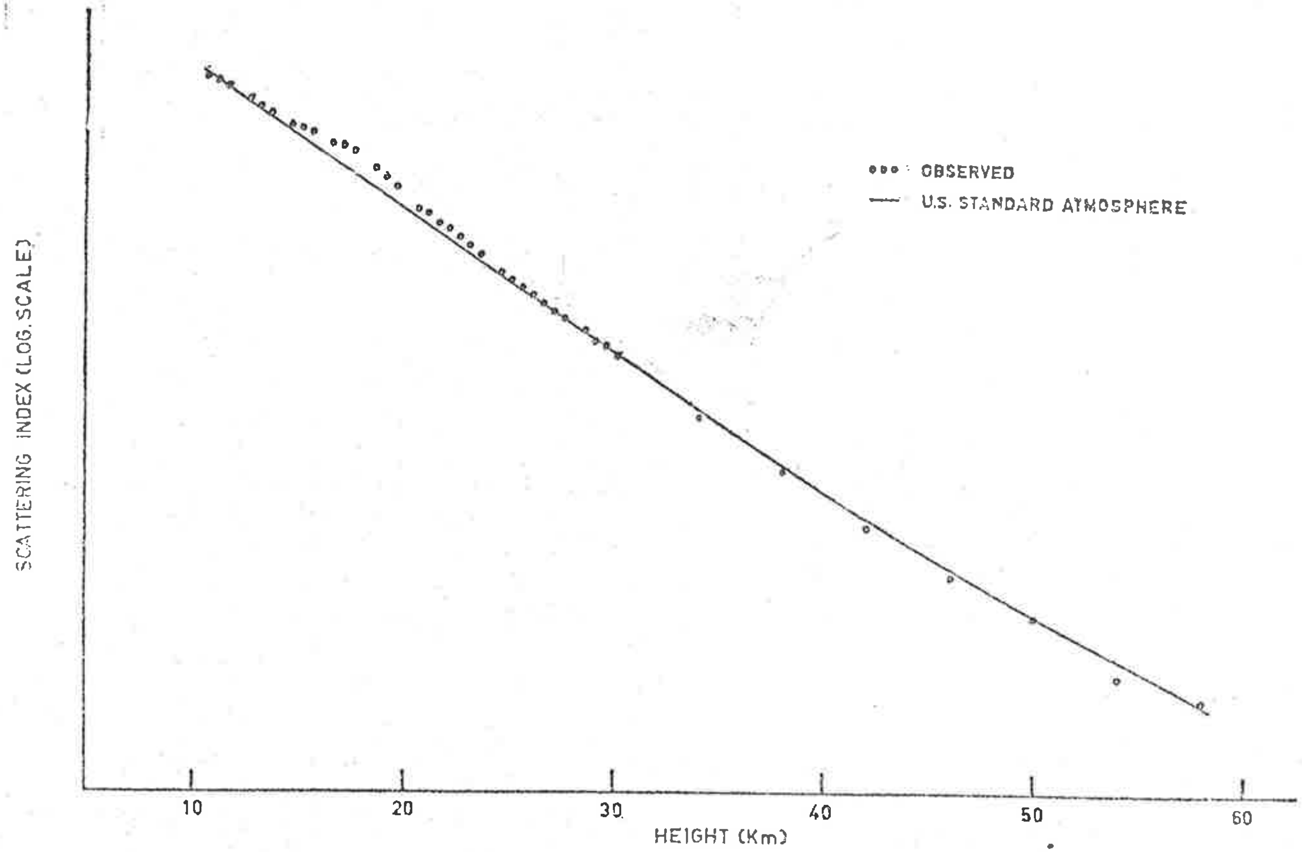

Fig. 3. Observed and calculated scattering profiles. The points representing the observations are the mean of 35 individual profiles for the period February–June, 1969.

normalization was sought and advantage was taken of the fact that particle sampling experiments (Junge *et al.*, 1961) have revealed a minimal aerosol number density at about 10 km. A simple analysis shows that within the accuracy of the laser experiment, the scattering at this height can be considered as molecular. A further advantage of the choice of the height of 10 km as the normalization level is that the lower portion of individual profiles can be compared with curves deduced from local radiosonde observations carried out on the same day. It is of interest to note that, at heights above 30 km, the experimental values of $h^2C(h)$ averaged over 35 individual profiles equal, within the limit of the experimental errors, the values calculated from the U.S. Standard Atmosphere, 1962, thus confirming the absence of significant numbers of aerosols above this level.

The mean experimental profile of $h^2C(h)$ vs. h shown in Fig. 3, is very similar in character to those obtained by workers in the Northern hemisphere (Clemesha *et al.*, 1966, Grams and Fiocco, 1967). The departure of the observed points in the 13–24 km region from the curve calculated for pure molecular scattering is interpreted as indicating the existance of a broad aerosol layer in this region.

Figure 4 shows the ratio of experimentally observed to calculated scattering for the 10–30 km height range for four individual nights. In this region, the calculated values were derived from air densities obtained from the Bureau of Meteorology radiosonde observations at the nearby Adelaide Airport on the corresponding days, as it has been found that over this height range the radiosonde data often depart significantly from the Standard Atmosphere. The general character of the ratio profile is stable for periods of a day or so, but significant changes are observed over periods of about a week. Over the 5 month period of observation (February–June 1969), the peak ratio, occurring at approximately 19 km, increased steadily from 1·25 to 1·75. These ratios are smaller than corresponding values published by workers in the Northern Hemisphere. Observations are continuing in order to determine if the increasing trend is part of a seasonal variation.

The maximum height from which returns can be satisfactorily measured with the present equipment is limited both by the statistics of the received count, and by the background count rate. The background count is caused by photomultiplier noise, and to a lesser extent by night sky emission, and becomes equal to the signal count rate at about 65 km. At this altitude, the count rate due to backscattered laser photons is approximately 0·15 per km channel width per 100 laser firings. It is thus necessary to accumulate the count from a large number of laser firings to obtain statistically meaningful results from the 60 km region.

4. Estimation of Aerosol Number Density

It is possible to estimate the number density of the aerosol particles if certain assumptions are made regarding their properties. The particle sampling experiments carried out by Junge *et al.* (1961), Friend (1966) and Mossop (1965), indicate that aerosols in the stratosphere are predominantly ammonium sulphate (or persulphate) particles many of which are coated with a volatile substance which is most likely to be water. Many workers choose the refractive index of ammonium sulphate (1·50) in calculations pertaining to the stratospheric aerosol. However, it

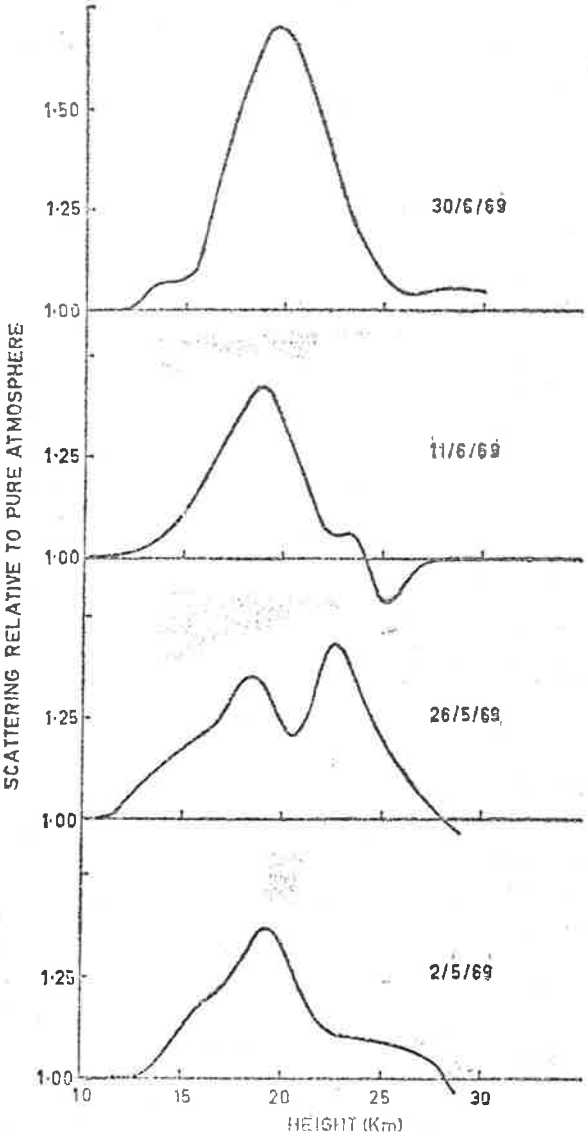

Fig. 4. Graphs of the ratios of observed to predicted scattering in the height range 10–30 km, showing the increase in the peak ratios during May and June, 1969.

is also reasonable to assume the refractive index to be that of water (1·33). Fortunately, the effect of this difference on the final number density answers is relatively small, and in the present calculations a value of 1·40 is chosen to conform with the work of Dave and Mateer (1963).

If it is assumed that the particles are spherical, the Mie theory of scattering can be applied to yield backscattering functions $\Sigma_a(\pi, r)$ (m^2 sterad.$^{-1}$) as functions of the particle radius r. Calculations based on a spherical shape for the atmospheric aerosol can be justified by the results of Powell *et al.* (1967). Their experiments showed that optical scattering properties of an ensemble of non-spherical, randomly aligned particles differ from those of geometrically equivalent spherical particles only when the particles are highly elongated. The aerosol collection experiments of Mossop (1965) indicate that few of the atmospheric particles would fall into this category.

The averaged aerosol backscattering function $\overline{\Sigma_A(\pi)}$ is found by integration of $\Sigma_A(\pi, r)$ over the range of particle sizes. If $\mathrm{d}N(r)$ is the number of particles having radii between r and $r + \mathrm{d}r$, then

$$\overline{\Sigma_A(\pi)} = \int_{r_1}^{r_2} \Sigma_A(\pi, r)\, \mathrm{d}N(r) \Big/ \int_{r_1}^{r_2} \mathrm{d}N(r)$$

where r_1 and r_2 are the limits of particle sizes.

Junge's power law model has been used by many authors to describe the size distribution of stratospheric aerosols. However, this model has been shown by Friend (1966) to be suspect in the small size range. The lognormal size distribution used by Dave and Mateer (1968) has therefore been utilized in the present calculations. This distribution is specified by

$$\frac{\mathrm{d}N(r)}{\mathrm{d}(\log r)}\ \alpha \exp\left[-\left(\log\frac{r}{r_0}\right)^2 \Big/ 2\, s^2\right]$$

where r_0 is the mean radius, and s is the standard deviation.

From the averaged results of Friend (1966) and Mossop (1965) we obtain $r_0 = 0{\cdot}35\ \mu$, and $s = 0{\cdot}30$ (using natural logarithms). The boundary values r_1 and r_2 in the integration are chosen to be 0·04 and 3·0 μ respectively, and, for a wavelength of 0·694 μ,

$$\overline{\Sigma_A(\pi)} = 2{\cdot}93 \times 10^{-14}\ \mathrm{m}^2\ \mathrm{sterad.}^{-1}$$

An increase in the integration range would have little effect on the value of $\overline{\Sigma_A(\pi)}$, due to the rapid decrease of particle number density away from r_0. For example, an extension of the integration range to limits of 0·01 and 8·0 μ only increases $\overline{\Sigma_A(\pi)}$ by approximately 0·03 per cent.

The ratio of observed to calculated scattering R, may be expressed by

$$R = \frac{B_r(\pi) + B_A(\pi)}{B_R(\pi)} = 1 + \frac{B_A(\pi)}{B_R(\pi)}$$

and its mean value at the height corresponding to the peak aerosol contribution in the stratosphere (18·5 km) is 1·5. Since $B_R(\pi)$ is known, and

$$B_A(\pi) = N_A\, \overline{\Sigma_A(\pi)}$$

N_A, the aerosol number density, may be calculated. The value obtained is

$$N_A = 7{\cdot}9 \times 10^5\ \mathrm{m}^{-3}.$$

Direct sampling experiments carried out by Chagnon and Junge (1961) yielded a maximum particle density near 20 km altitude of $10^5\ \mathrm{m}^{-3}$ for particles having radii between 0·1 and 1·0 μ. Rosen (1964) has found a maximum concentration of $3 \times 10^6\ \mathrm{m}^{-3}$ for particles having radii greater than 0·27 μ. The estimate obtained from the laser radar results presented here thus lies between these limits, and supports the assumption of a lognormal size distribution for particles in the stratosphere. For comparison, the above calculation has been repeated using the Junge size distribution $dN(r) \propto r^{-3}\,dr$ and yielded a value for N_d of $9{\cdot}8 \times 10^6\ m^{-3}$, an order larger than the number density derived using a lognormal distribution.

5. CONCLUSIONS

The laser radar equipment described in this paper is cabable of producing scattering profiles to an altitude of 60 km. Comparison of these profiles with curves calculated for purely molecular scattering shows the well-known stratospheric aerosol layer having a maximum concentration at 18·5 km. Assuming a lognormal size distribution for the stratospheric aerosol, the maximum number density is $7{\cdot}9 \times 10^5\ m^{-3}$, which lies between the estimates obtained from direct sampling experiments by Junge *et al.*, (1961) and Rosen (1964).

The authors believe that these are the first laser soundings of the atmosphere in the Southern hemisphere. The general form of the stratospheric aerosol layer appears very similar to that deduced from laser observations in the Northern hemisphere. However, the maximum concentration appears to be less in the Southern hemisphere.

Acknowledgements—This work was supported by grants from the Department of Supply and the University of Adelaide. The authors wish to thank Professor J. H. Carver and Mr. B. Rofe for their continued encouragement. The observations were carried out at the field station of the Mawson Institute for Antarctic Research, at Mt. Torrens. Much of the mechanical design of the equipment was carried out by Mr. C. F. Vaskess.

REFERENCES

Bain W. C. and Sandford M. C. W.	1966	*J. Atmosph. Terr. Phys.* **28**, 543.
Chagnon C. W. and Junge C. E.	1961	*J. Met.* **18**, 746.
Clemesha B. R., Kent G. S. and Wright R. W. H.	1966	*Nature, Lond.* **209**, 184.
Dave J. V. and Mateer C. L.	1968	*J. geophys. Res.* **73**, 6897.
Friend J. P.	1966	*Tellus* **18**, 465.
Goyer G. G.	1968	*Bull. Am. met. Soc.* **49**, 936.
Grams G. and Fiocco G.	1967	*J. geophys. Res.* **72**, 3523..
Junge C. E., Chagnon C. W. and Manson J. E.	1961	*J. Met.* **18**, 81.
Kent G. S., Clemesha B. R. and Wright R. W.	1966	*J. Atmosph. Terr. Phys.* **29**, 169.
Mossop S. C.	1965	*Geochim. Cosmochim. Acta* **29**, 201.
Palmer E. P. and Zdunkowski W. G.	1964	*J. geophys. Res.* **69**, 2369.
Powell R. S., Circle R. R., Vogel D. C., Woodson P. D. and Donn B.	1967	*Planet. Space Sci.* **15**, 1641.
Rosen J. M.	1964	*J. geophys. Res.* **69**, 4673.